

THESIS FOR THE DEGREE OF LICENTIATE OF PHILOSOPHY

Weld Pool Simulations

Marcus Edstorp

Department of Mathematical Sciences
Chalmers University of Technology and University of Gothenburg
Göteborg, Sweden 2008

Weld Pool Simulations
Marcus Edstorp

©Marcus Edstorp, 2008

NO 2008:19
ISSN 1652-9715
Department of Mathematical Sciences
Chalmers University of Technology and University of Gothenburg
SE-412 96 Göteborg
Sweden
Telephone +46 (0)31 772 1000

Cover:

Snapshot taken from a three-dimensional time-dependent simulation of a gas metal arc fillet welding process. The shape of the weld pool surface is visualized by arrows pointing in the directions of the surface normal.

Printed in Göteborg, Sweden 2008

Weld Pool Simulations

Marcus Edstorp

Department of Mathematical Sciences
Chalmers University of Technology and University of Gothenburg

Abstract

This investigation is devoted to the study of welding and its effect on the workpiece, focusing on the thermo and fluid dynamical phenomena occurring during an autogenous or non-autogenous arc fusion welding process. Its aim is to simulate the behaviour of the weld pool and analyze the consequence of the solid-liquid phase change, thus obtaining a methodology for predicting the appearance of weld defects related to solidification and cooling. In order to accomplish this, we solve equations governing a number of continuum mechanical and electromagnetic quantities, as well as consider the motion of the freely moving boundary of the weld pool. Since the state of these quantities is strongly influenced by phenomena such as arc and droplet impingement, non-isothermal phase change, surface tension, Marangoni forces and Lorentz forces, much effort is necessarily devoted to the modelling of the corresponding fluxes and sources, as well as to the implementation of computationally efficient techniques for simulating the geometrical deformation of the workpiece, which in our setting is entirely determined by the motion of the weld pool surface.

Common to all arc fusion welding processes is the employment of a welding arc. Many techniques rely on the arc to clean and shield the workpiece during the process, however in this study we consider it to be its main purpose to cause the local increase of thermal energy that is required for the establishment of the weld pool, and also to exert the mechanical forces that provoke the subsequent fluid flow which enhances heat transfer and facilitates weld penetration. The physics of the welding arc itself is quite intricate, and although the modelling of the arc is not the prime objective of this research project, we conclude that arc forces act on the pool surface, and that the investigation of the arc behaviour is important insofar that it provides input to the pool model and thus enables a more accurate prediction of the quality of the weldment that is created once the pool has solidified.

Keywords: Arc Welding, Weld Pool, Multiphysics Simulations, Moving Boundaries, Free Surfaces, Mesh Motion, Two-Phase Flow, Incompressible Flow, Electromagnetics, Finite Element Methods

Contents

1	Foreword and Acknowledgements	1
2	The Arc Fusion Welding Process	2
2.1	The workpiece	2
2.2	The welding arc	3
2.3	The influence of the arc on the workpiece	3
2.4	Cold laps	5
3	A Brief History of Weld Pool Simulations	6
4	Project Description	10
5	Mathematical Modelling of Weld Pools	11
5.1	Nomenclature	11
5.2	Continuum mechanics	19
5.2.1	A generic semi-weak balance equation	19
5.2.2	Continuity of mass and incompressibility	26
5.2.3	Balance of linear momentum	28
5.2.4	Conservation of energy	31
5.2.5	Pseudo-fluid workpiece motion	34
5.3	Electromagnetics	35
5.4	Pre-studies	38
5.4.1	2D time dependent vs. 3D steady state	38
5.4.2	The influence of filler metal heat transfer on the melting efficiency	39
6	Computational Modeling of Weld Pools	45
6.1	Pseudocompressibility	45
6.2	Mesh moving techniques	46
6.3	Dimensional analysis	47
6.4	Laminar vs. turbulent modelling	47
6.5	The DASPK algorithm and implementation details	48
6.6	A GMA fillet weld case study	49
6.7	A moving mesh mixed finite element method of lines	61
6.8	Something on continuum surface formulations and level set methods	70
7	Calibration and Verification	78
7.1	Incompressibility relaxation	78
7.2	Calibration of the temperature coefficient of surface tension and verification of fusion zone shape for a linear autogeneous GTA bead-on-plate weld	78

8 Applications and Conclusions	87
8.1 Welding out-of-position	87
8.2 Metal deposition and metallurgical simulations	89
8.3 Laser welding	89
8.4 The influence of arc forces on the probability of overlap	90
8.5 Summary, conclusions and future work	91
References	95

1 Foreword and Acknowledgements

The work performed during the creation of a simulations tool consists in modelling the process one wishes to simulate, solving a set of equations, validating and in a fair way presenting the result. The purpose of this treatise is to create a tool for simulating the appearance of cold laps in arc fusion welding (see section 4), a tool that will increase our understanding the underlying physics and the passage in the weld process that cause these faults. In order to accomplish this purpose, the author has undertaken a journey through the study of relativistic continuum mechanics, hands-on welding sessions, analytic solutions of Maxwells equations, and extensive bug checking of computer code for finite element analysis.

Since the prime objective of this research project is to understand why and when weld defects appear, and employ this knowledge when designing high performance welding sequences, it has been necessary to perform experiments and measurements on joints produced using such fusion processes. The results and analyses of these experiments are reported in [28, 29, 30, 31, 32]. In addition to this monograph, the theoretical work on the simulation of weld pools has also been reported in [22, 23, 24].

Marcus Edstorp is a Master of Science in Mathematics with orientation towards Industrial Mathematics from the *University of Gothenburg*. His Master Thesis work [21] in the field of Materials Science is on the simulation of fatigue micro-cracks, and was performed at the *Chalmers University of Technology* department of Computational Mathematics and in cooperation with *The Swedish National Testing and Research Institute*. His interest in weld pool simulations was aroused by the several research projects concerning the simulation and control of manufacturing processes incited and carried out at the *University West*.

The author would like to express his gratitude towards colleagues at *University West* as well as towards project participators at the *supporting companies* (see section 4).

*'assumption is the mother of all fuck-ups'*¹

Production Technology Centre, Trollhättan, September 5, 2008

¹Quoted from the movie *Under Siege 2*

2 The Arc Fusion Welding Process

Messler (c.f. [60]) attempts a definition of welding, describing it as *a process in which materials of the same fundamental type or class are brought together and caused to join (and become one) through the formation of primary (and, occasionally, secondary) chemical bonds under the combined action of heat and pressure*. The reader may also refer to this work for different types of classifications of welding techniques. We shall now brief upon the fundamental principles common to the set of processes that we consider in this study. These include the gas tungsten arc welding (GTAW) technique (a.k.a. TIG) when performed autogenously, plasma arc welding (PAW) in conduction mode, and gas metal arc welding (GMAW) techniques in spray transfer mode, including MIG and MAG and their tandem versions. In addition to the mentioned electrode arc fusion welding processes, our results apply to some extent also to the high energy density beam welding techniques including electron-beam welding (EBW) and laser-beam welding (LBW), in cases when they are not operated in key-hole mode.

2.1 The workpiece

The material body subject to welding is known as the *workpiece*. The workpiece will at every time instant t in the simulation interval $[0, t_{end}]$, via its current configuration, be identified with a subset $\Omega(t)$ of three-dimensional Euclidean (x, y, z) -space. When simulating square butt joints (as well as bead-on-plate welds), it is implicitly assumed that the weld plane, i.e. the surface on which the arc impinges, is a subset of the plane $y = 0$ prior to the welding sequence, and that its outwards normal points in the direction of increasing y .

The material of the unprocessed workpiece is known as the *base material* or *base metal*. This terminology is employed in order to distinguish the base material from the material that is added to the workpiece during non-autogenous welding processes, i.e. the *filler material* (*filler metal*). The mechanical properties of the filler material often differs from those of the base material, since the characteristics of the former are chosen in such a fashion that the quality of the joint is optimized. However, the tracking of the different species in a heterogenous weld implies a complication that we do not attempt to resolve within the scope of this project, and so we treat all welds as homogenous; That is, the base and filler metals are the one and same, and in many of the cases we consider it consists in an alloyed steel or a titanium alloy. At this stage, it should be pointed out that we consider every material as a continuum, completely characterized by its density, conductivity, viscosity, latent heat content, melt interval and surface tension, defined as pointwise functions on $\Omega(t)$. We abandon the continuum view only when trying to capture the occurrence of outer lack of fusion (see section 2.4), and preclude the possibility of lack of fusion in the interior of the weld. Thus heterogenous welds can actually be simulated, if the components can be approximated by the same values for those material properties.

2.2 The welding arc

In this text we refer to as *the arc* any means by which energy is transported from the solid welding equipment to the workpiece. The energy can for example be transported as kinetic energy carried by thermally emitted electrons, as heat via a plasma or a filler metal droplet, or it can be carried by the photons of a laser beam. The manner in which the arc transports the energy is determined by the type of welding process that is employed. However, it is unambiguously so, that the arc affects the workpiece not only by the generating heat at the weld surface and/or in the pool, but also by transferring to it a considerable amount of momentum, sometimes in the form of droplets and grosse sets of particles impinging en masse.

The analysis of the welding arc behaviour is a separate research field. For a survey on the subject, see [81]. At the present we are interested primarily in the weld pool, so the results elsewhere obtained for arcs are important to us only in that they give expressions for sources and input boundary conditions to the weld pool model. However, there is mutual influence between arc and weld pool, so an ultimate goal is to couple their respective models.

2.3 The influence of the arc on the workpiece

The influence of the arc on the workpiece is sometimes characterized by numbers such as the *transfer efficiency*, the *transferred power* and the *net heat input* (c.f. [60]). These are rough measures, there is sometimes ambiguity in their definitions, and they do not uncloak the details of the influence of the welding arc on the workpiece. Since we will differentiate between the manners in which energy is introduced in, and transferred away from, the workpiece, we will not indulge in the definitions of these concepts (although we sometimes refer to them without further ado!). An exception is when we hypothesize the shape of the inwards heat flux distribution on the weld surface (usually Gaussian in the distance from a given point), and choose its size such that if no heat is lost from the workpiece during the process, the total flux through the surface is equal to a number referred to as the *transferred power*. In these cases we define the transferred power as the total power $\mathcal{W}(t)$ delivered by the source, i.e. the *source power*, multiplied by the transfer efficiency η , which is a process specific number between 0 and 1. We also make use of a source distribution coefficient $a(t)$ (the *spot radius*), which is related to the dispersion of the heat flux around the source center $P(t)$. The purpose of the transfer efficiency is to take into account energy losses such as the ones due to electric resistance in the welding equipment and heat losses from the arc. It can also model heat losses from the workpiece, which is usually the type of transfer efficiency that is physically measured, using for example a calorimeter (see [50]). Since we model heat losses separately, our transfer efficiency will be higher than such. For a more detailed discussion of arc (and melting) efficiencies, and measurements thereof, see [20]. For an example of an application of inverse techniques for estimating these quantities for a GTAW process, see [33].

For welding processes employing electric energy sources, we take $\mathcal{W}(t)$ to be the product of the voltage and amperage as displayed at the welding terminal. This view of the source power is stringent with our strive to have simulations approach real life applications. However, it impacts on the value of the transfer efficiency, since measuring the voltage between a TIG electrode and the base plate would not give the same value as when measuring at the terminal. Taking a global view of welding simulation, we would like to model also the electric circuit, but this step has not been incorporated in this treatise.

Inherent to the fusion welding process is the melting of the base material. Except for cleaning and shielding the workpiece, we consider it to be the major purpose of the source and arc to establish the *weld pool* (melt pool, liquid pool). Since the workpiece is considered homogenous, the weld pool is at every time instant t constituted by the part $\Omega_w(t)$ of the workpiece the temperature of which is above the liquidus point of the base material. It is this melting, and the subsequent cooling that makes feasible the epitaxial growth of the metallic crystal structure which upon solidification implies material continuity between the joint surfaces, and thus the weld itself. For GTAW, the heating is accomplished mainly by a transformation into thermal energy of the kinetic energy of the welding arc electrons (or ions). For PAW, it is a consequence also of the thermal conduction through the workpiece surfaces caused by the hot plasma. Since the major part of the thermal energy is generated at, or conducted through, the surface, the actual melting of the base material is accomplished by thermal diffusion and the subsequent convective transport of thermal energy that occurs as the latent heat barrier is overcome. EBW and LBW techniques are frequently operated in keyhole mode, i.e. the mode during which the depth of the pool cavitation is much greater than its width and burn-through may even appear, and during such processes other phenomena play important roles in the advancement of the pool. During LBW, the recoil pressure due to the evaporation of the base material prevents the keyhole from collapsing, and during EBW a relatively large part of the transferred energy can be generated inside the workpiece. This makes keyhole welding essentially different from the *conduction mode* techniques we foremost consider in this treatise.

When welding alloys, the base material does not melt, nor does it solidify, at a specific temperature, but over a temperature range. This is why we employ the terminology *liquidus point* and *solidus point*, and write T_m and T_s respectively. This range is usually called the melting interval, and material at temperature in the melting interval is called *mushy*. Likewise, at every time instant t , the part $\Omega_{mz}(t)$ of the workpiece the temperature of which is above the solidus point but below the liquidus point of the base material, is termed the *mushy zone*.

The experimental study of welds is often performed after the welding process is terminated, as is also the case in our project. One can then divide the weldment into four distinct zones; these are the *Fusion Zone* (FZ), the *Partially Melted Zone* (PMZ), the *Heat Affected Zone* (HAZ) and the unaffected base material. The FZ is the part of the workpiece the temperature of which during welding was ever above the liquidus point, i.e. was ever a part of the weld pool. The PMZ is the part that was ever mushy but never completely liquid.

During welding, heat is conducted away from the PMZ, where it affects the material properties of the base material. The HAZ is the part of the workpiece the microstructure (or mesostructure²) of which was significantly influenced by the heat input but at all times was at temperatures below the solidus point.

The arc exerts pressure and drag forces on the surface of the weld pool. This causes the shape of the workpiece to change during welding. Specifically, there is created an *arc cavity*. This cavity is of considerable depth during keyhole welding, but also appears when using GMAW and TIG equipment. Due to the limited compressibility of the liquid metal it follows that peripheral parts of the weld pool surface rise above their original levels, unless substantial evaporation of the base metal occurs such as in keyhole laser welding; It even happens that the molten metal overflows the boundaries of the weld pool and flows onto the solid base material. This may give rise to one of the unwanted phenomena that we will try to investigate in more detail. However we note that the arc forces can also have positive effects on the pool in that the cavitation provokes weld penetration and that they can aid in keeping the pool in place when welding out of position.

2.4 Cold laps

A cold lap occurs when, upon solidification, the workpiece experiences self contact without enough fusion across the interface, the result thus being the formation of a crack. Due to stress intensification at the crack tip, the resistance of the weldment towards fatigue and other sources of structural failure is lowered. Typically, the defect originates as the weld pool overflows or spatters on to the solid base plate and solidifies without carrying enough energy to establish the heat transfer required to partially melt the base plate and enable the recrystallization process the result of which is material continuity. These defects can sometimes be treated by mechanically postprocessing the weld, but this is costly and time consuming, so it is preferable to have them not appear at all. Investigations and categorisations of cold laps appearing at the weld toe during tandem GMA welding can be found in [28, 30]. In [32] their appearance is shown to derive mainly from the mentioned spatter and overlap. See also [2] for an investigation of the appearance of cold laps in cruciform joints.

²By microstructure we mean the crystalline structure at the length scale of one Burgers vector, and by mesostructure we designate the pattern of the grains, each of which is made up from a (nearly) perfect lattice.

3 A Brief History of Weld Pool Simulations

We now brief upon the recent history of welding simulations. Inlining with the aim of our project, we focus on attempts to simulate the vicinity of the fusion zone, and hence do not discuss further the results of *computational weld mechanics* (CWM) simulations in which the mechanical state of the entire weldment is sought. In the CWM simulations, the weld pool is often represented simply as a heat source and fluid flow is ignored, even though convective effects are sometimes taken into account by employing effective values for the thermal properties of the weld and base metal. In [74, 73] there was presented solutions for a coupling of fluid dynamics and solid mechanics in the same simulation, but else such investigations are not very common.

The article [44] surveys in a comprehensive manner the efforts within the field of weld pool, welding arc and welding electrode simulations performed until the year 1990. Also, the article [89] assessed the state of weld phenomena modelling in the year 1995. In the present monograph we highlight only a small yet significant part of these contributions to the early development of weld pool simulations.

[51] claims to be the first investigation in which the location of the solid-liquid boundary is a priori unknown. Instead it is calculated as a steady solution of the Boussinesq approximation for the laminar Navier-Stokes equations in combination with an enthalpy method and the effective-viscosity formulation, much in the vein of the approach employed in the present thesis. [51] also presents an analytical expression for the Lorentz force, which is due to the electric current flowing through the workpiece during an electric arc welding process. This expression has since been subject to extensive use in weld pool simulations, see section 5.3. The work was carried on in [52].

In the earlier history of weld pool simulations, the investigation [87] focused on the effects of a surface tension coefficient that varied with the concentrations of a surface active element and temperature. It was found that for the GTAW process, the concentration of sulphur had an appreciable effect on the weld pool development, however this effect of the minor elements on the weld pool flow and shape had been experimentally investigated and documented much earlier (see for example [36, 37] and likewise [38] for high-density beam techniques). In [86], the model was expanded to incorporate a more detailed modelling of the evaporative flux. It is now known that the surface tension variation significantly impacts on the weld pool fluid flow and thus the penetration depth.

Since convection was seen to exercise a considerable effect on the shape and depth of the weld pool (see for example [86] and [45]) and the chemical composition of the weld metal (see for example [15]), and the Lorentz force was appreciated as a major force driving the fluid flow, one has sought ways of evaluating this force in an efficient and accurate way. In the early days of weld pool simulations, this was done using analytical solutions of the Maxwell equations (again c.f. section 5.3). In addition to [51] and [52], the work presented in [76] has often been referred to in the literature. This study also took into account transient effects in the pool as well as the heat transferred to the pool via filler

droplets. More recently, refined expressions have been suggested ([53]). There is of course yet the problem concerning the lack of certainty in the boundary conditions. The uncertainty in boundary conditions for the weld pool can be reduced if the pool simulation is coupled to a welding arc simulation. Such multiphysics simulations have begun to emerge during the last decade (see below), and the work seems promising.

Despite their popularity, the validity of the analytical expressions for the Lorentz force are very limited when dealing with moving weld pool surfaces and complex configurations. In order to approximate these forces in a detailed way, not only are accurate boundary conditions of importance, but one is also required to solve yet another set of equations. This certainly is a complex and time-consuming matter, and this is the reason why analytic expressions are often used instead, and also why it has long been many a researchers effort to develop an efficient algorithm that is capable of finding the Lorentz force through the solution of the equations governing the electromagnetic field. In connection to this it is worth noting that the articles [48] and [35] contains simulations in which the Lorentz force is calculated from a potential function for which an equation is solved on a domain that changes shape with time due to the deformation of the pool surface.

The first simulations of GTA weld pools considering the dynamic behaviour of the surface of a convection-conduction weld pool, as well as the impingement forces of filler metal droplets driven by the arc plasma drag force and electromagnetic force (see for example [79]), were developed in the late 90's. Until then, one had often considered the pool and arc separately. As mentioned, this implied that the reliability and usefulness of simulations aimed at predicting the behaviour of the surface and interior geometry of the weld pool, were often limited by the lack of certainty in the input boundary conditions and parameter values (c.f. [12]). Specifically, the arc efficiency and radii produced by the welding process, as well as heat transfer coefficients at clamped, cooled and weld surfaces are inherently difficult to experimentally determine. Moreover, values of the thermophysical quantities of the base material are not always known at high temperatures. This is a drawback, since it has been known for a long time that the way in which, for example, the surface tension gradient is taken to depend upon temperature and the activity of surface active species certainly has an impact on the weld pool fluid flow and thus on the predicted shape of the pool (c.f. [86, 15]). One may thus be required to employ an optimization process in order to obtain approximate values for some parameters. The matter is further complicated by the fact that the values of the thermophysical quantities obtained by such an optimization are "effective values", which consequently are dependent on the specific welding method, and on the choice of quantities the effective values were optimized with respect to. With these reservations, different algorithms were employed in ([63, 54, 56]) in order recreate GMA and GTA weld geometries.

Many investigations assume a flat weld pool surface, even though the presence of a pool cavity due to the arc force, may significantly influence penetration depth and pool geometry. When simulating autogeneous GTA pools or conduc-

tion mode laser weld pools, c.f. [93] and [65] respectively, this approach is under many circumstances adequate. When simulating non-autogenous fusion weld pools with the aim of predicting reinforcement shape, such an assumption of a flat weld pool surface is not even feasible. In the late 90's, pools with surfaces depressed by the influence of arc pressure were simulated in [49], and the depressing action of filler metal droplets impinging on the surface was also considered in [7], however a somewhat simpler model employing the Landau transformation (c.f. section 6.2) had much earlier been used to simulate deformed surfaces in [75]. Within our project, a model for moving weld pool surfaces was developed [24, 22, 23], taking into account the influence of filler metal spray transfer, but not the coupled behaviour of the arc. This model allows for an arbitrary motion of the pool, except that it in its present state does not automatically detect self contact. Many other researchers that consider the motion of the weld pool surface does so in order to accurately predict the bead shape and weld penetration. In such cases, a simpler representation of the motion is possible (see section 6.2), and the surface shape is often calculated by minimising a surface energy functional, c.f. [84, 90]. In [26, 27] (c.f. also [79] and [42]) there was implemented two-dimensional models for calculating globular mass transfer and electrical potential in the arc and workpiece. The authors were thus able to consider electromagnetic effects in a weld pool with a moving surface. Their results agreed reasonably well with measurements of bead geometries, and thus showed a promising future for fusion welding simulations in which the two-way coupling between the arc and pool is considered.

Worth mentioning is also the article [58] which claims to be the first study in which the finger penetration pool shape generated by the impingement of molten metal droplets on a GMA weld pool surface was modeled using a volumetric heat source applied in the workpiece interior.

In [40] there was simulated a steady incompressible weld pool during a stationary GTAW process. Having noticed earlier that laminar models tend to overestimate the depth of the weldpool ([39]), the authors used a $k - \epsilon$ turbulent model for the fluid flow. They allowed for a deformed weld pool surface, but ignored the effects of arc pressure and drag, as well as latent heat effects. However, the heat flux at the surface was calculated taking into account convection, radiation and vaporisation and their model treated the effects of impurity concentrations on surface tension. The results are interesting in that they suggested that the fluid flow under the given circumstances was turbulent, since the results of the turbulent model corresponded better with experimental results than those of the laminar model.

A time-dependent axisymmetric model was implemented in [82]. They assumed a flat weld pool surface and a vanishing mushy zone, but incorporated convective, radiative and evaporative effects, and considered a coefficient of surface tension that depended upon the activity of surface active species and the surface temperature. This study is noticed since the authors implemented their model using a finite element method, which contrasts with the otherwise commonly used finite volume and finite difference methods. Furthermore, a special method for evolving the solid-liquid interface had to be used in order to capture

the sharp pool boundary using a continuum approach. The numerical results were shown to correspond well with the experimental results for GTAW that were performed in the same study. This model was later extended in [19, 18], where it was used to obtain time-dependent 3D simulations with moving sources.

To this day, the arc and pool are often simulated separately or with a simple coupling, however increasingly often researchers find it useful to consider several phenomena in a fully coupled way. This is part of taking a global view of welding, that is, simulations in which the respective models for the welding equipment, the welding arc, the weld pool, the solid mechanics of the welded structure, and the metallurgy of the joint, are coupled together. In addition to discovering valuable facts about the nature of the welding process and finding out how to incorporate these in the design stage, it is part of our vision, a vision that is presumably shared by many other researchers in the field of welding, to implement a system for online control of the process using feed-back based on information from monitoring systems and possibly real-time simulations. This vision is somewhat utopian, however the global view of the process is the view that one should adhere to in order to work towards this end. An attempt at this is presented in the article [72].

4 Project Description

Considering the huge tonnage of weldments being produced every year within the automotive industry, the aerospace industry and in the field of structural engineering, one realizes that it is immensely advantageous to achieve high quality welds in a robust manner. To optimize weld resistance against failure (due to fatigue for example), we need to minimize the occurrence of defects such as porosity, liquation cracks, cold cracks, extreme grain coarsening, embrittlement and the aforementioned cold laps, which is a special kind of defect that arises when, upon solidification, two parts of the workpiece come in contact but is not succeeded by proper bonding across their common interface (see section 2.4). Focusing on cold laps, the aim of our current project is the following: Produce a methodology/tool for simulating the weld pool created during an arbitrary configured arc fusion welding process, and employ it in order to predict, and thus understand, the appearance of cold laps. This involves the development and implementation of a continuum mechanical model for the weld pool behaviour, and investigations of the bonding and heat transfer across surface discontinuities.

Since the task of simulating the appearance of cold laps is a great one, a partial goal has been to simulate the behaviour of the workpiece with respect to the distribution of heat, the interior weld geometry and the motion of the weld pool surface. If this goal is reached, we have at hand a tool that outputs data that is valuable as input to welding simulations with respect to metallurgy and solid mechanics. In addition to this monograph, the theoretical work performed on the simulation of weld pools within this project, has also been reported in [24, 22, 23].

The work on weld pool simulations which is reported in this monograph was originally carried out as one of two parts of the project “Formation and detection of weld defects related to solidification and cooling”, the other part being focused on welding experiments and detection. The work within both project parts was supported and guided by the competence of the following *supporting companies*;

Volvo Aero Corporation (VAC)
Volvo Construction Equipment (VCE)
ESAB AB
SSAB Tunnplåt AB

For the project “Formation and detection of weld defects related to solidification and cooling”, funding was received by 50 percent from the *Knowledge Foundation*³, and by 50 percent from the *supporting companies*. The work has since then been carried on mainly as a part of the project “INNSide”, which is supported in part by VAC.

³Stiftelsen för Kunskaps- och Kompetensutveckling

5 Mathematical Modelling of Weld Pools

This chapter is devoted to the mathematical modelling of weld pools, which by necessity also includes modelling the heat transfer in the solid part of the workpiece, as well as modelling the heat, mass and momentum fluxes induced by the welding arc. Many of the important phenomena may be incorporated when employing a continuum mechanical approach, and we therefore commence by deriving the corresponding equations. Although a continuum mechanical model can describe macroscopic phenomena such as deformation and fluid flow, it does not give any information about the micro and meso structural properties of the joint. In order to investigate and simulate the bonding, adhesion and the possible lack of fusion that strongly affects the weld quality, some other modelling strategy is required, primarily one based on kinetic theory. Kinetic theory is commonly employed when modelling the solidification front and grain growth in steel welds, and [66] applied a kinetic model for the dissolution of gas into the liquid pool. Also promising are the phase-field models considering the free energy of the system, such as in [77]. This type of analysis we however postpone indefinitely.

The electromagnetics of the arc and weld pool deserves a separate treatment. The theory we require for our immediate purposes is developed in section 5.3.

5.1 Nomenclature

We frequently employ the notation \mathcal{X} to designate an arbitrary physical quantity such as mass, momentum or energy. In this section, the unit of \mathcal{X} is written $[\mathcal{X}]$. In what follows, we summarize a substantial part of the nomenclature employed in this treatise, together with short descriptions and references to the sections in which the respective quantities are introduced and properly defined. We have excluded the notation introduced in section 6.8, since it is a stand-alone section of minor impact.

Section 2

<i>Notation</i>	<i>Unit</i>	<i>Description</i>
$t \in \mathbb{R}^+$	s	Time parameter
$t_{end} \in \mathbb{R}^+$	s	Simulation end time
$\Omega(t) \subset \mathbb{R}^3$		Spatial domain for the model equations at time $t \in [0, t_{end}]$, also referred to as <i>the workpiece</i>
$\mathcal{W}(t) \in \mathbb{R}^+$	W	Source power at time $t \in [0, t_{end}]$
$a(t) \in \mathbb{R}^+$	m	Spot radius at time $t \in [0, t_{end}]$
$P(t) = [P_1(t), P_2(t), P_3(t)]^T$	m	Source center at time $t \in [0, t_{end}]$
$\eta \in [0, 1]$	1	Transfer efficiency of welding process
$\Omega_w(t) \subset \Omega(t)$		Weld pool at time t
$T_m \in \mathbb{R}^+$	K	Liquidus point of base material
$T_s \in \mathbb{R}^+$	K	Solidus point of base material
$\Omega_{mz}(t) \subset \Omega(t)$		Mushy zone at time t

Section 5.2.1

<i>Notation</i>	<i>Unit</i>	<i>Description</i>
$\mathcal{X}^t : \Omega(t) \rightarrow \mathfrak{R}$	$[\mathcal{X}]/m^3$	Spatial representation of the density distribution of the arbitrary quantity \mathcal{X} at time t
$V(\mathcal{X}^t)$		Weighting space for \mathcal{X}^t
$\phi^t : \Omega(t) \rightarrow \mathfrak{R}$	1	Weighting function, a member of $V(\mathcal{X}^t)$
$\mathbf{q}_{tot}^t : \Omega(t) \rightarrow \mathfrak{R}^3$	$[\mathcal{X}]/m^2s$	Spatial representation of total flux density for \mathcal{X}^t at time t
$F^t : \Omega(t) \rightarrow \mathfrak{R}$	$[\mathcal{X}]/m^3s$	Spatial representation of total source density for \mathcal{X}^t at time t
$W \in \mathfrak{R}^3$		Control volume in $\Omega(t)$
$\mathbf{n}^t : \partial\Omega(t) \rightarrow \mathfrak{R}^3$	1	Outwards unit normal to $\Omega(t)$
$\frac{D}{Dt}$		Differential operator for derivative following the fluid
$\mathbf{q}^t : \Omega(t) \rightarrow \mathfrak{R}^3$	$[\mathcal{X}]/m^2s$	Spatial representation of non-advective flux density for \mathcal{X}^t at time t
$\Omega^0 \subset \mathfrak{R}^3$		Referential domain for the model equations
$\{\omega^t\}_{t \in [0, t_{end}]}$	m	Workpiece motion
$\omega(\cdot, t) : \Omega^0 \ni \mathbf{X} \xrightarrow{\sim} \omega^t _{\Omega^0}(\mathbf{X}) \in \Omega(t)$	m	Simplified notation for workpiece motion
$\hat{\mathcal{X}} : \Omega^0 \times [0, t_{end}] \rightarrow \mathfrak{R}$	$[\mathcal{X}]/m^3$	Material representation of \mathcal{X}^t
$\hat{\phi} : \Omega^0 \times [0, t_{end}] \rightarrow \mathfrak{R}$	1	Material representation of weighting function
$\mathcal{J}_\omega = \mathcal{J}_\omega(\cdot; t) : \Omega^0 \rightarrow \mathfrak{R}^{i \times i}, i = 2 \text{ or } 3$	1	Jacobian matrix of the current configuration at time t
$ \mathcal{J}_\omega : \Omega^0 \rightarrow \mathfrak{R}$	1	Jacobian determinant of the current configuration at time t
$\mathbf{X} = [X, Y, Z]^T$	m	Independent Cartesian coordinates on the referential domain
$\mathbf{x} = [x, y, z]^T$	m	Independent Cartesian coordinates on the spatial domain
$\nabla_{\mathbf{x}}$		Nabla operator acting on spatial representations
$\nabla_{\mathbf{X}}$		Nabla operator acting on material representations

$\hat{\mathbf{q}} : \Omega^0 \times [0, t_{end}] \ni (\mathbf{X}, t) \rightarrow [\hat{q}_1(\mathbf{X}, t), \hat{q}_2(\mathbf{X}, t), \hat{q}_3(\mathbf{X}, t)] \in \mathfrak{R}^3$			
	$[\mathcal{X}]/m^2s$		Material representation of non-advective flux density for \mathcal{X}^t
$\hat{F} : \Omega^0 \times [0, t_{end}] \rightarrow \mathfrak{R}$			
	$[\mathcal{X}]/m^3s$		Material representation of total source density for \mathcal{X}^t
$D \subset \mathfrak{R}^2$			Domain of definition for \mathbf{r}
(s_1, s_2)	m		Independent Cartesian coordinates in D
$\mathbf{r} : D \rightarrow \partial\Omega^0$	m		Parametrization of $\partial\Omega^0$
$\dot{\omega}^t : \Omega(t) \rightarrow \mathfrak{R}^3$	m/s		Spatial representation of motion velocity
$\mathbf{v} \in \mathfrak{R}^3$	m/s		Velocity of source center
$v \in \mathfrak{R}^+$	m/s		Speed of source center
$Z^* \in \mathfrak{R}$	m		Referential z -coordinate for space-time material motion
$\nabla_{(\mathbf{x}, t)}$			Nabla operator acting on space-time material representations
$\omega^* : \Omega^0 \times [0, t_{end}] \rightarrow \mathfrak{R}^4$			Space-time material motion
$\mathcal{J}_{\omega^*} \in \mathfrak{R}^{4 \times 4}$			Jacobian of current space-time configuration
$\mathbf{A} \in \mathfrak{R}^{2 \times 2}$	1		Matrix for artificial convection in space-time material formulations
$\hat{\mathbf{t}} : \Omega_{Z^*} \times [0, t_{end}] \rightarrow \mathfrak{R}^2$			
	1		Positively oriented unit tangent to $\partial\Omega_{Z^*}$
$\Omega_{Z^*} \subset \mathfrak{R}^2$			Z -slice of Ω^0 , for $Z^* = 0$ it is referred to as <i>the computational domain</i>
$\nabla_{(X, Y)}$			Nabla operator acting on two-dimensional material representations
$t^* \in \mathfrak{R}$	s		Referential time in stationary model

Section 5.2.2

<i>Notation</i>	<i>Unit</i>	<i>Description</i>
$V(t) \in \mathfrak{R}^3$		Moving control volume in $\Omega(t)$
$\rho^t : \Omega(t) \rightarrow \mathfrak{R}$	kg/m^3	Spatial representation of mass density at time t
$M^t : V(p^t) \rightarrow \mathfrak{R}$	kg/s	Deposition rate at time t
$\mathbf{q}_m^t : \Gamma_w(t) \ni \mathbf{x} \rightarrow [q_{m,1}^t(\mathbf{x}), q_{m,2}^t(\mathbf{x}), q_{m,3}^t(\mathbf{x})] \in \mathfrak{R}^3$	kg/m^2s	Spatial representation of boundary mass flux density at time t
$\rho_{ref} \in \mathfrak{R}^+$	kg/m^3	Constant referential mass density
$\Gamma_0^w \subset \partial\Omega_0$		Welding surface in the computational domain
$\Gamma_w(t) \subset \partial\Omega(t)$		Welding surface in the spatial domain
$\Gamma_w^0 \subset \partial\Omega^0$		Welding surface in the referential domain
$\hat{\mathbf{q}}_m : \Gamma_w^0 \times [0, t_{end}] \ni (\mathbf{X}, t) \rightarrow [\hat{q}_{m,1}(\mathbf{X}, t), \hat{q}_{m,2}(\mathbf{X}, t), \hat{q}_{m,3}(\mathbf{X}, t)] \in \mathfrak{R}^3$	kg/m^2s	Material representation of boundary mass flux density
$D_w \subset \mathfrak{R}^3$		Projection of welding surface
$b(t) \in \mathfrak{R}^+$	m	Spray radius at time t
$M(t) \in \mathfrak{R}^+$	kg/s	Total deposition rate at time t
\hat{M}	kg/s	Material formulation of M^t
$\hat{p} : \partial\Omega_0 \times [0, t_{end}] \ni (X, Y, t) \rightarrow \bar{p} \circ \omega(X, Y, t) \in \mathfrak{R}$	1	Material representation of test function for pressure in two dimensions

Section 5.2.3

<i>Notation</i>	<i>Unit</i>	<i>Description</i>
$\mathbf{F}^t : \Omega(t) \rightarrow \mathfrak{R}^3$	N/m^3	Spatial representation of force density at time t
$\mathbf{F}_{em}^t : \Omega(t) \rightarrow \mathfrak{R}^3$	N/m^3	Spatial representation of electromotive force density at time t
$\mathbf{g} = [g_1, g_2, g_3]^T \in \mathfrak{R}^3$	m/s^2	Gravitational acceleration
$\beta \in \mathfrak{R}^+$	$1/K$	Thermal expansion coefficient
$T_{sm} \in \mathfrak{R}$	K	Mean melting temperature
$\mathbf{u}^t : \Omega(t) \ni \mathbf{x} \rightarrow [u_1, u_2, u_3]^T \in \mathfrak{R}^3$	m/s	Spatial representation of mass averaged fluid velocity at time t
$\sigma^t : \Omega(t) \rightarrow \mathfrak{R}^{3 \times 3}$	N/m^2	Spatial representation of Cauchy stress at time t
$\Gamma^t : V(\mathbf{u}) \rightarrow \mathfrak{R}$	N	Surface force at time t
$\gamma^t : \partial\Omega(t) \rightarrow \mathfrak{R}$	N/m	Spatial representation of surface tension at time t
∇_S		Surface gradient operator
$P_{arc}(t) \in \mathfrak{R}$	N	Arc force at time t
$p_{arc}(t) \in \mathfrak{R}$	m	Arc impingement radius at time t
$\gamma_m \in \mathfrak{R}$	N/m	Surface tension at liquidus point
$-A \in \mathfrak{R}$	N/mK	Temperature coefficient of surface tension
$R \in \mathfrak{R}$		Gas constant
$\Gamma_{sol} \in \mathfrak{R}$		Surface excess at saturation
$K^\circ \in \mathfrak{R}$		Adsorption coefficient
$a_i \in \mathfrak{R}$		Activity of species
$k_1 \in \mathfrak{R}$		Entropy factor
$\Delta H^\circ \in \mathfrak{R}$		Standard heat of adsorption
$p^t : \Omega(t) \rightarrow \mathfrak{R}$	N/m^2	Spatial representation of pressure at time t
$\hat{\mu} : \mathfrak{R} \rightarrow \mathfrak{R}$	Ns/m^2	Effective dynamic viscosity
$\mu_m \in \mathfrak{R}^+$	Ns/m^2	Dynamic viscosity of liquid base material
$\hat{\mathbf{u}} : \Omega^0 \times [0, t_{end}] \ni (\mathbf{x}, t) \rightarrow [\hat{u}_1(t), \hat{u}_2(t), \hat{u}_3(t)]^T \in \mathfrak{R}^3$	m/s	Material representation of mass averaged fluid velocity
$\hat{p} : \Omega^0 \times [0, t_{end}] \rightarrow \mathfrak{R}$	N/m^2	Material representation of pressure
$\hat{\beta} : \mathfrak{R} \rightarrow \mathfrak{R}$	$1/K$	Effective thermal expansion coefficient
$\hat{\mathbf{F}}_{em} : \Omega^0 \times [0, t_{end}] \rightarrow \mathfrak{R}^3$	N/m^3	Material representation of electromotive force density
$\hat{\Gamma}$	N	Material formulation of Γ^t

Section 5.2.4

<i>Notation</i>	<i>Unit</i>	<i>Description</i>
$h^t : \Omega(t) \rightarrow \mathfrak{R}$	J/m^3	Spatial representation of sensible enthalpy density at time t
$\Delta H^t : \Omega(t) \rightarrow \mathfrak{R}$	J/m^3	Spatial representation of latent enthalpy density at time t
$T_0 \in \mathfrak{R}$	K	Initial temperature
$c : \mathfrak{R} \rightarrow \mathfrak{R}$	J/kgK	Heat capacity
$L \in \mathfrak{R}^+$	J/kg	Latent heat coefficient
$f : \mathfrak{R} \rightarrow \mathfrak{R}$	1	Local liquid fraction
$k_\infty^t : \partial\Omega(t) \rightarrow \mathfrak{R}$	W/m^2K	Combined heat transfer coefficient at time t
$Q^t : V(T^t) \rightarrow \mathfrak{R}$	W	Transferred power
$k : \mathfrak{R} \rightarrow \mathfrak{R}$	W/mK	Thermal conductivity
$T^t : \Omega(t) \rightarrow \mathfrak{R}$	K	Spatial representation of temperature at time t
$\hat{c} : \mathfrak{R} \rightarrow \mathfrak{R}$	J/kgK	Effective heat capacity
$\hat{T} : \Omega^0 \times [0, t_{end}] \rightarrow \mathfrak{R}$	K	Material representation of temperature
$\hat{\sigma} : \Omega_0 \times [0, t_{end}] \rightarrow \mathfrak{R}^{2 \times 2}$	N/m^2	Two dimensional material representation of Cauchy stress at time t
$\hat{k}_\infty : \partial\Omega_0 \times [0, t_{end}] \rightarrow \mathfrak{R}$	W/m^2K	Material representation of combined heat transfer coefficient
σ	W/m^2K^4	Stefan-Boltzmann constant
$\hat{\epsilon} : \partial\Omega_0 \times [0, t_{end}] \rightarrow \mathfrak{R}$	1	Material representation of workpiece emissivity
\hat{Q}	W	Material representation of Q^t
$\hat{T}_\infty : \partial\Omega_0 \times [0, t_{end}] \rightarrow \mathfrak{R}$	K	Material representation of ambient temperature

Section 5.2.5

<i>Notation</i>	<i>Unit</i>	<i>Description</i>
$\lambda^t : \partial\Omega^t \rightarrow \mathfrak{R}$		Spatial representation of Lagrange multiplier for kinematic constraint
$\mathcal{L} : V(\dot{\omega}^t) \times V(\lambda^t) \rightarrow \mathfrak{R}$		Lagrangean for constrained mesh velocity
μ_{mesh}	Ns/m^2	Mesh viscosity
$\hat{\Gamma}_\omega : V(\frac{\partial\omega}{\partial t}) \rightarrow \mathfrak{R}$	N	Material formulation of force on pseudo-fluid surface

Section 5.3

<i>Notation</i>	<i>Unit</i>	<i>Description</i>
$\mu_B \in \mathfrak{R}^+$	H/m	Effective magnetic permeability
r	m	Radial distance from arc center in reference domain
r_1	m	Distance from projected arc center in reference domain
$h_0 \in \mathfrak{R}^+$	m	Thickness of undeformed base plate
$\sigma(t) \in \mathfrak{R}^+$	m	Incident current spot radius at time t
$j : \mathfrak{R} \rightarrow \mathfrak{R}$	A/m^2	Incident current strength on weld surface

Section 5.4

<i>Notation</i>	<i>Unit</i>	<i>Description</i>
H_{melt}	1	Melting efficiency

Section 6

<i>Notation</i>	<i>Unit</i>	<i>Description</i>
ϵ	t	Relaxation parameter
h	m	Mesh size function
h_8	m	Height function in method of spines
h_ϵ	m	Local element size at the fillet

<i>Notation</i>	<i>Unit</i>	<i>Description</i>
-----------------	-------------	--------------------

$\hat{\nabla}_S$		Material representation of surface gradient operator
η_v	1	Efficiency of applied volumetric heat source
η_s	1	Efficiency of applied surface heat source

5.2 Continuum mechanics

Previous studies ([28, 30, 32]) indicate that cold laps appear due to unfavorable combinations of the dynamic behaviour of the workpiece surface and the pool solidification circumstances. The prediction of these characteristics requires insight into a number of different physical phenomena and their effect on the thermodynamical and mechanical state of the material body. In particular, the flow of liquid metal determines the dynamical behaviour of the pool surface. It is also known that the interior shape and size of many a weld pool is markedly influenced by the convective heat transfer induced by such gross motion of particles (c.f. for example [39]). We therefore begin this section by deriving a generic balance equation which is then instantiated for the mass density ρ^t , the fluid momentum density $\rho^t \mathbf{u}^t$ and the energy density H^t . Much effort is put into modelling fluxes and sources for these quantities. Since the geometrical deformation of the workpiece is of immense importance to us, we also propose an equation for the workpiece motion $\{\omega^t\}_t$. However, the design of such an equation is actually a matter of computational modelling, and will thus not be discussed in detail until chapter 6.

We state from the outset, that we do consider the material of the continuum to be homogeneous with respect to chemical composition (see for example [10] for a study in which the composition of the base material is simulated using a mixture model). This implies that we do not model the distribution of different species in the weld pool, and that macrosegregation and the evaporation rates of different alloying elements are not considered separately, although this could very well affect the mechanical properties of the joint. Liquation cracking, for example, can be predicted using a model including solute transport (see [62]), and consequently we cannot simulate the appearance of such defects in that manner.

Unless they are of particular interest, boundary and initial conditions are not presented in this section. The full system of equations, together with conditions, is written down in section 6.7.

5.2.1 A generic semi-weak balance equation

We now derive a generic semi-weak balance equation for an arbitrary physical quantity \mathcal{X} , the density distribution of which at time t is represented spatially by the function $\mathcal{X}^t : \Omega(t) \rightarrow \mathfrak{R}$. We denote by $V(\mathcal{X}^t)$ the weighting space for \mathcal{X}^t , but postpone the discussion concerning the specific properties of this space

until chapter 6. For now we assume only that $\phi^t \in V(\mathcal{X}^t)$ is smooth enough to allow the necessary operations.

A pointwise equation for a of the family $\{\mathcal{X}^t\}_{t \in [0, t_{end}]}$ posed on the sequence of spatial domains $\{\Omega(t)\}_{t \in [0, t_{end}]}$ is obtained by first considering that, for every $t \in [0, t_{end}]$, the conservation of \mathcal{X} in any open control volume W fixed in the interior of $\Omega(t)$ can be expressed with the use of the flux \mathbf{q}_{tot}^t and the source density F^t :

$$\frac{d}{dt} \int_W \mathcal{X}^t = - \int_{\partial W} \mathbf{q}_{tot}^t \cdot \mathbf{n}^t + \int_W F^t \quad (1)$$

For any useful definition of flux and source, \mathcal{X}^t is determined by relation (1). In reality, \mathcal{X}^t is a quantity that is measured during the calibration and validation of a continuum mechanical model, so modelling is simply nothing more than finding a flux \mathbf{q}_{tot}^t and source F^t that fits into relation (1) given a function \mathcal{X}^t . This process is simplified by the fact that a measurement would not output a pointwise function, but perhaps rather samples of \mathcal{X}^t , which allows us to use forms of the flux and source that are simpler than the ideal ones, yet being able to accurately recreate and predict the outcome of experiments. It should be pointed out at this stage that validation requires us to transform our measurement results into mathematical quantities (a real representing temperature or length for example) and correlate these with the samples of \mathcal{X}^t and hence there is always a probabilistic element involved. One can therefore claim that the mathematics and numerics upon which a simulation is built is “true” or “correct” only if the simulation tool, with a certain probability, can produce results that match any experimental result within a specified process window. Having noted this, we invoke classical arguments and decades of experience, and find it worthwhile to let every thermomechanical quantity \mathcal{X} be subject to the advective flux $\mathcal{X}^t \mathbf{u}^t$ ($\mathbf{u}^t = [u_1, u_2, u_3]^T$ is the flow velocity, see section 5.2.3), and we follow here the standard approach of separating the advective flux from the total flux and dividing it into a convective term and a compressibility term. As we consider arbitrary fixed control volumes, and continuity of \mathcal{X}^t and \mathbf{q}_{tot}^t is assumed, the partial differential equation follows:

$$\frac{D}{Dt} \mathcal{X}^t = -\mathcal{X}^t \nabla \cdot \mathbf{u}^t - \nabla \cdot \mathbf{q}^t + F^t \quad (2)$$

where $\mathbf{q}_{tot}^t = \mathbf{q}^t + \mathcal{X}^t \mathbf{u}^t$, and $\frac{D}{Dt} = \frac{\partial}{\partial t} + \mathbf{u}^t \cdot \nabla$ is the derivative following the fluid.

We now seek to formulate equation (2) weakly in space, and thus multiply it by $\phi^t \in V(\mathcal{X}^t)$, and integrate over the spatial domain:

$$\int_{\Omega(t)} \frac{\partial \mathcal{X}^t}{\partial t} \phi^t + \int_{\Omega(t)} \nabla [\mathcal{X}^t] \mathbf{u}^t \phi^t = - \int_{\Omega(t)} \mathcal{X}^t \nabla \cdot [\mathbf{u}^t] \phi^t - \int_{\Omega(t)} \nabla \cdot [\mathbf{q}^t] \phi^t + \int_{\Omega(t)} F^t \phi^t \quad (3)$$

One-phase equations such as (3) are not adopted for numerical implementation, since the symmetric difference between the domains of definition of \mathcal{X}^t

for two distinct values of t cannot be assumed null, and thus the left hand side integral is undefined whenever the spatially represented time derivative $\frac{\partial \mathcal{X}^t}{\partial t}$ is discretized. In order to derive a generic semi-weak formulation on a referential domain Ω^0 we turn instead to a material formulation, and hence introduce the workpiece motion $\{\omega^t\}_{t \in [0, t_{end}]}$. Specifically, we consider general workpiece motions that generally do not coincide with the motion of the physical fluid that we wish to model. In order to simplify our notation, we for now choose the reference configuration as to coincide with the initial configuration, and hence the material representation of the current configuration restricted to the referential domain, i.e. $\omega^t|_{\Omega^0} =: \omega(\cdot, t) : \Omega^0 \xrightarrow{\sim} \Omega(t)$ is a bijection that possesses C^1 -continuity with respect to the independent variable describing the initial location of an arbitrary particle. This transformation is in our case not known a priori, but is determined both by computational needs and as part of the solution. Denoting material representations by adding a hat, i.e. $\hat{\mathcal{X}}(\cdot, t) = \mathcal{X}^t \circ \omega(\cdot, t)$, we have by the chain rule that

$$\frac{\partial}{\partial t} [\mathcal{X}^t] \circ \omega(\cdot, t) = \frac{\partial}{\partial t} [\hat{\mathcal{X}}](\cdot, t) - \nabla [\mathcal{X}^t] \circ \omega(\cdot, t) \frac{\partial \omega}{\partial t}(\cdot, t)$$

Using this relation, we can transform the integral on left hand side of (3) to the referential domain:

$$LHS(3) = \int_{\Omega^0} \frac{\partial}{\partial t} [\hat{\mathcal{X}}] \hat{\phi} |J_{\omega}| + \int_{\Omega^0} \nabla [\mathcal{X}^t] \circ \omega(\cdot, t) (\hat{\mathbf{u}} - \frac{\partial \omega}{\partial t}) \hat{\phi} |J_{\omega}|$$

where $J_{\omega} = J_{\omega}(\cdot; t)$ is the Jacobian of the map $\mathbf{X} = [X, Y, Z]^T \rightarrow \omega(\mathbf{X}; t)$. As the derivatives with respect to the spatial coordinates $\mathbf{x} = [x, y, z]^T$ are transformed according to the rules $\nabla_{\mathbf{x}}^T = J_{\omega}^{-T} \nabla_{\mathbf{X}}^T$ and $\nabla_{\mathbf{x}} = J_{\omega}^{-T} : \nabla_{\mathbf{X}}$, we arrive at a semi-weak material formulation:

$$\begin{aligned} & \int_{\Omega^0} \left[\frac{\partial}{\partial t} \hat{\mathcal{X}} + \nabla_{\mathbf{x}} \hat{\mathcal{X}} J_{\omega}^{-1} (\hat{\mathbf{u}} - \frac{\partial \omega}{\partial t}) \right] \hat{\phi} |J_{\omega}| = \\ & - \int_{\Omega^0} \hat{\mathcal{X}} \nabla_{\mathbf{x}} \hat{\mathbf{u}} : J_{\omega}^{-T} \hat{\phi} |J_{\omega}| - \int_{\Omega^0} \nabla_{\mathbf{x}} \hat{\mathbf{q}} : J_{\omega}^{-T} \hat{\phi} |J_{\omega}| + \int_{\Omega^0} \hat{F} \hat{\phi} |J_{\omega}|, \forall \phi^t \in V(\mathcal{X}^t) \end{aligned} \quad (4)$$

In order to avoid differentiation of the flux and incorporate natural boundary conditions, we apply Greens formula to the corresponding integral. If $\mathbf{r} : (s_1, s_2) \in D \rightarrow \partial\Omega^0$ is a parametrization of $\partial\Omega^0$, then $\omega(\cdot, t) \circ \mathbf{r}$ is a parametrization of $\partial\Omega(t)$, and we have that

$$\begin{aligned} & \int_{\Omega^0} \nabla_{\mathbf{x}} \hat{\mathbf{q}} : J_{\omega}^{-T} \hat{\phi} |J_{\omega}| = \\ & - \int_{\Omega^0} \hat{\mathbf{q}} \cdot \nabla_{\mathbf{x}} \hat{\phi} J_{\omega}^{-1} |J_{\omega}| + \int_D \hat{\mathbf{q}} \circ \mathbf{r} \cdot J_{\omega} \circ \mathbf{r} \frac{\partial \mathbf{r}}{\partial s_1} \times J_{\omega} \circ \mathbf{r} \frac{\partial \mathbf{r}}{\partial s_2} \hat{\phi} \circ \mathbf{r} \end{aligned} \quad (5)$$

It should be noted that the weighted counterpart of relation (1) can be obtained using the geometric conservation law $\frac{\partial}{\partial t} |J_{\omega}(\cdot; t)| = |J_{\omega}(\cdot; t)| \nabla \cdot [\dot{\omega}^t] \circ$

$\omega(\cdot, t)$, where $\dot{\omega}^t \circ \omega^t = \frac{\partial \omega}{\partial t}$, and requiring the material representation of each weighting function to be constant in time;

$$\begin{aligned} \frac{d}{dt} \int_{\Omega(t)} \mathcal{X}^t \phi^t + \int_{\Omega(t)} (\mathbf{u}^t - \dot{\omega}^t) \cdot \nabla \mathcal{X}^t \phi^t = \\ - \int_{\Omega(t)} \mathcal{X}^t \nabla \cdot [\mathbf{u}^t - \dot{\omega}^t] \phi^t + \int_{\Omega(t)} \mathbf{q}^t \cdot \nabla \phi^t \\ - \int_{\partial\Omega(t)} \mathbf{q}^t \cdot \mathbf{n}^t \phi^t + \int_{\Omega(t)} F^t \phi^t, \forall \phi^t \in V(\mathcal{X}^t) \end{aligned} \quad (6)$$

We have treated the flux $\mathcal{X}^t [\mathbf{u}^t - \dot{\omega}^t]$ in a special way. It is important to analyze the influence that this flux has on the amount of \mathcal{X} contained in the control volume, i.e. we wish to see how the moving boundary affects the integral $\int_{\Omega(t)} \mathcal{X}^t$. This can be done by inserting the function $\phi^t \equiv 1$ into equation (6). When disregarding sources and other fluxes, we get

$$\frac{d}{dt} \int_{\Omega(t)} \mathcal{X}^t = - \int_{\Omega(t)} (\mathbf{u}^t - \dot{\omega}^t) \cdot \nabla \mathcal{X}^t - \int_{\Omega(t)} \mathcal{X}^t \nabla \cdot [\mathbf{u}^t - \dot{\omega}^t], \quad (7)$$

and we see that the divergence of $\dot{\omega}^t$ acts as a source. If a partial integration of the advective flux is allowed, the following version of equation (6) holds;

$$\begin{aligned} \frac{d}{dt} \int_{\Omega(t)} \mathcal{X}^t \phi^t = + \int_{\Omega(t)} (\mathbf{q}^t + \mathcal{X}^t [\mathbf{u}^t - \dot{\omega}^t]) \cdot \nabla \phi^t \\ - \int_{\partial\Omega(t)} (\mathbf{q}^t + \mathcal{X}^t [\mathbf{u}^t - \dot{\omega}^t]) \cdot \mathbf{n}^t \phi^t + \int_{\Omega(t)} F^t \phi^t, \forall \phi^t \in V(\mathcal{X}^t) \end{aligned}$$

and the influence of the moving boundary could be studied via the equation;

$$\frac{d}{dt} \int_{\Omega(t)} \mathcal{X}^t = - \int_{\partial\Omega(t)} \mathcal{X}^t [\mathbf{u}^t - \dot{\omega}^t] \cdot \mathbf{n}^t \quad (8)$$

We constrain the motion of the workpiece using the kinematic constraint $\mathbf{u}^t \cdot \mathbf{n}^t = \dot{\omega}^t \cdot \mathbf{n}^t$. Studying equation (8), it would thus seem that if the arbitrary motion of the boundary is to influence \mathcal{X} , either the advective field is not well behaved enough to allow for the partial integration, or the kinematic condition is violated. We have seen from case studies, that the kinematic constraint is actually *not* violated, yet the thermal energy of the workpiece is increased as a consequence of the added filler. It turns out that the incompressibility constraint is numerically violated in the interior of the domain. We investigate this phenomena in more detail in section 5.4.2.

We note also that in equations (7) and (8), the influence of $\dot{\omega}^t$ is a source for \mathcal{X} that is dependant upon \mathcal{X}^t itself. This is an inherent feature in arbitrary

motions techniques; We cannot control the influence of a freely moving boundary on \mathcal{X}^t without controlling \mathcal{X}^t . For example, the thermal energy contained in a control domain increases as a result of a positive divergence of $\dot{\omega}^t$, i.e. an outwards moving boundary, but we cannot say in what way unless we know the temperature distribution. However, in our applications, the magnitude of the power transferred to the workpiece is of major interest, and it is reasonable to assume that the power transferred by the filler metal increases and decreases with the pool temperature, since these quantities depend in similar fashions on the energy of the welding arc. This is another reason for the further discussion on in section 5.4.2. We will see that we have the possibility of restricting the influence of the moving boundary to the boundary itself, so it is enough to apply essential boundary conditions on \mathcal{X} in order to explicitly control this influence.

If the weld source center $P : [0, t_{end}] \rightarrow \mathfrak{R}^3$ moves at the constant velocity \mathbf{v} in the joint plane $x = 0$, and at constant height over the weld surface, we may further reduce the complexity of equation (4) by assuming that for every physical quantity \mathcal{X} , including fluxes and sources, it is valid that $\mathcal{X}^t(x, y, z) = \mathcal{X}^{t - \frac{z - Z^*}{v}}(x, y, Z^*)$ for any fixed $Z^* \in \mathfrak{R}$ and any $(\mathbf{x}, t) \in \Omega(t) \times [0, t_{end}]$, where $v = |\mathbf{v}|$. These circumstances may apply for example to linear GMA butt-welding when the arc height and contact tube to work distance is constant, and the weld pass is long. In practice, oscillations in the applied welding current and the pool cavitation depth, as well as small imperfections in the base material, often implies that the pool never actually reaches a steady configuration no matter how long the weld. Yet, we find it appropriate to invoke this simplifying assumption in this first stage of modelling. The simplification is based on the rewriting of equation (2) so that $0 = -\nabla_{(\mathbf{x}, t)} \cdot [\mathbf{q}_{tot}^t(\mathbf{x}), \mathcal{X}^t(\mathbf{x})] + F^t(\mathbf{x})$ and on the broadening of the concept of material motion to include also time. The derivation of formulation (4) is still valid, but the time differentiations are now part of the gradient operator. Considering motions on the form $\omega^*(X, Y, Z, \hat{t}) = [\omega_1(X, Y, \hat{t}), \omega_2(X, Y, \hat{t}), Z, \hat{t} + \frac{Z - Z^*}{v}]^T$, we see that all material representations are independent of Z . Hence it suffices to solve only for the plane $Z = Z^*$ where transformed and physical time coincide. Specifically, we have that

$$\mathcal{J}_{\omega^*} = \begin{bmatrix} \mathcal{J}_{\omega} & 0 & \frac{\partial \omega_1}{\partial \hat{t}} \\ & 0 & \frac{\partial \omega_2}{\partial \hat{t}} \\ 0 & 0 & 1 & 0 \\ 0 & 0 & 1/v & 1 \end{bmatrix}$$

and hence $|\mathcal{J}_{\omega}| = |\mathcal{J}_{\omega^*}|$. Furthermore,

$$\mathcal{J}_{\omega^*}^{-1} = \begin{bmatrix} \mathcal{J}_{\omega}^{-1} & \mathbf{A} \\ 0 & 0 & 1 & 0 \\ 0 & 0 & -1/v & 1 \end{bmatrix}$$

where $\mathbf{A} = [1/v \mathcal{J}_{\omega}^{-1} \frac{\partial \omega}{\partial \hat{t}} \quad -\mathcal{J}_{\omega}^{-1} \frac{\partial \omega}{\partial \hat{t}}]$, and ω now has only the two components ω_1 and ω_2 . If we temporarily leave out the advective flux, we thus see that the balance equation can be written explicitly as

$$\begin{aligned} \int_{\Omega^0 \times [0, t_{end}]} \begin{bmatrix} \frac{\partial \hat{q}_1}{\partial \hat{X}} & \frac{\partial \hat{q}_1}{\partial \hat{Y}} & 0 & \frac{\partial \hat{q}_1}{\partial \hat{t}} \\ \frac{\partial \hat{q}_2}{\partial \hat{X}} & \frac{\partial \hat{q}_2}{\partial \hat{Y}} & 0 & \frac{\partial \hat{q}_2}{\partial \hat{t}} \\ \frac{\partial \hat{q}_3}{\partial \hat{X}} & \frac{\partial \hat{q}_3}{\partial \hat{Y}} & 0 & \frac{\partial \hat{q}_3}{\partial \hat{t}} \\ \frac{\partial \hat{\chi}}{\partial \hat{X}} & \frac{\partial \hat{\chi}}{\partial \hat{Y}} & 0 & \frac{\partial \hat{\chi}}{\partial \hat{t}} \end{bmatrix} : \begin{bmatrix} \mathcal{J}_\omega^{-T} & 0 & 0 \\ 0 & 0 & 0 \\ \mathbf{A}^T & 1 & -1/v \\ 0 & 0 & 1 \end{bmatrix} \hat{\phi} | \mathcal{J}_\omega | \\ = \int_{\Omega^0 \times [0, t_{end}]} \hat{F} \hat{\phi} | \mathcal{J}_\omega | \end{aligned}$$

which is equivalent to

$$\begin{aligned} & \int_{\Omega^0 \times [0, t_{end}]} \left[\frac{\partial \hat{\chi}}{\partial \hat{t}} - \frac{1}{v} \frac{\partial \hat{q}_3}{\partial \hat{t}} \right] \hat{\phi} | \mathcal{J}_\omega | \\ & - \int_{\Omega^0 \times [0, t_{end}]} \frac{\partial \omega}{\partial \hat{t}} \cdot \nabla_{(X, Y)} \left[\hat{\chi} - \frac{1}{v} \hat{q}_3 \right] \mathcal{J}_\omega^{-1} \hat{\phi} | \mathcal{J}_\omega | = \\ & - \int_{\Omega^0 \times [0, t_{end}]} \nabla_{(X, Y)} \begin{bmatrix} \hat{q}_1 \\ \hat{q}_2 \end{bmatrix} : \mathcal{J}_\omega^{-T} \hat{\phi} | \mathcal{J}_\omega | + \int_{\Omega^0 \times [0, t_{end}]} \hat{F} \hat{\phi} | \mathcal{J}_\omega | \end{aligned}$$

It is close at hand now to consider a space-time finite element method. However, the reason we employ the space-time material motion is to derive an equation that can be solved using the method of lines, since this is the kind of formulation our software is adopted for (see sections 6.7 and 6.5 and the comment on equation (11)). Thus, we now omit the integrations with respect to Z and \hat{t} , apply Greens formula, and again incorporate the advective flux. This leaves us with a two-dimensional material formulation:

$$\begin{aligned} & \int_{\Omega_{Z^*}} \frac{\partial}{\partial \hat{t}} \left[\hat{\chi} - \frac{\hat{q}_3 + \hat{\chi} \hat{u}_3}{v} \right] \hat{\phi} | \mathcal{J}_\omega | + \int_{\Omega_{Z^*}} \nabla_{(X, Y)} \hat{\chi} \mathcal{J}_\omega^{-1} \left(\begin{bmatrix} \hat{u}_1 \\ \hat{u}_2 \end{bmatrix} - \frac{\partial \omega}{\partial \hat{t}} \right) \hat{\phi} | \mathcal{J}_\omega | \\ & + \int_{\Omega_{Z^*}} \frac{\partial \omega}{\partial \hat{t}} \cdot \nabla_{(X, Y)} \frac{\hat{q}_3 + \hat{\chi} \hat{u}_3}{v} \mathcal{J}_\omega^{-1} \hat{\phi} | \mathcal{J}_\omega | = \\ & - \int_{\Omega_{Z^*}} \hat{\chi} \nabla_{(X, Y)} \begin{bmatrix} \hat{u}_1 \\ \hat{u}_2 \end{bmatrix} : \mathcal{J}_\omega^{-T} \hat{\phi} | \mathcal{J}_\omega | + \int_{\Omega_{Z^*}} [\hat{q}_1, \hat{q}_2] \cdot \nabla_{(X, Y)} \hat{\phi} \mathcal{J}_\omega^{-1} | \mathcal{J}_\omega | \\ & - \int_{\partial \Omega_{Z^*}} [-\hat{q}_2, \hat{q}_1] \mathcal{J}_\omega \hat{\mathbf{t}} \hat{\phi} + \int_{\Omega_{Z^*}} \hat{F} \hat{\phi} | \mathcal{J}_\omega |, \forall \phi^t \in V(\mathcal{X}^t) \end{aligned} \quad (9)$$

where $\hat{\mathbf{t}}$ is the positively oriented unit tangent to $\partial \Omega_{Z^*}$, and $\Omega_{Z^*} = \{[X, Y] : \mathbf{X} \in \Omega^0, Z = Z^*\}$. Equation (9) hints that we may disregard the total flux in the z -direction if the arc speed is high enough. An attempt of quantifying this critical arc speed is presented in section 5.4.1. Finally, let us note that when disregarding the total flux in the z -direction, we obtain exactly the two-dimensional version of equation (4). What more is, equation (9) is further

simplified when incorporating not only the assumption that the flux \hat{q}_3 vanishes at all points, but also the incompressibility constraint (see equation (13));

$$\begin{aligned} \int_{\Omega_{Z^*}} \left(1 - \frac{\hat{u}_3}{v}\right) \frac{\partial}{\partial t} \hat{\chi} \hat{\phi} |_{\mathcal{J}_\omega} + \int_{\Omega_{Z^*}} \nabla_{(X,Y)} \hat{\chi} \mathcal{J}_\omega^{-1} \left(\begin{bmatrix} \hat{u}_1 \\ \hat{u}_2 \end{bmatrix} - \frac{\partial \omega}{\partial t} \left(1 - \frac{\hat{u}_3}{v}\right) \right) \hat{\phi} |_{\mathcal{J}_\omega} = \\ + \int_{\Omega_{Z^*}} [\hat{q}_1, \hat{q}_2] \cdot \nabla_{(X,Y)} \hat{\phi} \mathcal{J}_\omega^{-1} |_{\mathcal{J}_\omega} \\ - \int_{\partial \Omega_{Z^*}} [-\hat{q}_2, \hat{q}_1] \mathcal{J}_\omega \hat{\mathbf{t}} \hat{\phi} + \int_{\Omega_{Z^*}} \hat{F} \hat{\phi} |_{\mathcal{J}_\omega}, \forall \phi^t \in V(\mathcal{X}^t) \end{aligned} \quad (10)$$

When instantiating equation (10) we set $Z^* = 0$ and ignore the fluid flow component parallel to the weld line, i.e. $u_3 \equiv 0$. Equation (10) is a very useful material formulation of equation (6) since we have, unlike in equation (5), explicitly incorporated a parametrization of the domain boundaries, which is advantageous when solving the equation using our choice of software. In the study presented in [11], the authors employ an argument for reducing their problem from three spatial dimensions to two spatial dimensions and time, which is akin to the presented here, other than that we have not seen this approach be used explicitly anywhere else.

Hereafter we abuse our notation somewhat; The same notation is used for three-dimensional material representations and those material representation only two components of which are considered. This implies a slight blurring of the distinction between the referential domain Ω^0 and the computational domain Ω_0 , although it should be clear from the context which definition is intended. This is actually a conceptual advantage of our modelling approach, since the governing equations are exactly the same in the three dimensional time-dependent case, as when considering only two space dimensions and time.

Another way to model the steady-state weld pool is to let the moving coordinate system travel at the same velocity as the source center, for example by choosing $\omega(X, Y, Z, t) = [\omega_1(X, Y, Z, t^*), \omega_2(X, Y, Z, t^*), \omega_3(X, Y, Z, t^*)]^T + (t - t^*)\mathbf{v}$. The corresponding assumption on \mathcal{X}^t is that $\mathcal{X}^t(\mathbf{x}) = \mathcal{X}^{t^*}(\mathbf{x} - (t - t^*)\mathbf{v})$ for any fixed $t^* \in \mathfrak{R}$, and the material representations are thus independent of time. The resulting equation is

$$\begin{aligned} \int_{\Omega^0} \nabla_{\mathbf{x}} \hat{\chi} \mathcal{J}_\omega^{-1} (\hat{\mathbf{u}} - \mathbf{v}) \hat{\phi} |_{\mathcal{J}_\omega} = \\ - \int_{\Omega^0} \hat{\chi} \nabla_{\mathbf{x}} \hat{\mathbf{u}} : \mathcal{J}_\omega^{-T} \hat{\phi} |_{\mathcal{J}_\omega} - \int_{\Omega^0} \nabla_{\mathbf{x}} \hat{\mathbf{q}} : \mathcal{J}_\omega^{-T} \hat{\phi} |_{\mathcal{J}_\omega} + \int_{\Omega^0} \hat{F} \hat{\phi} |_{\mathcal{J}_\omega}, \forall \phi^t \in V(\mathcal{X}^t) \end{aligned} \quad (11)$$

Equation (11), is theoretically equivalent to a formulation in which time and two spatial dimensions are considered. We have however found that when employing the method of lines with our software, convergence is usually faster and memory requirements not as substantial.

5.2.2 Continuity of mass and incompressibility

In many standard textbooks and other treatises on continuum mechanics, a pointwise equation expressing the continuity of mass is derived using the transport theorem and an equality resembling $0 = \frac{d}{dt} \int_{V(t)} \rho(\mathbf{x}, t) d\mathbf{x}$. The transport theorem is certainly mathematically correct, however the equality expressing the conservation of mass is a matter of modelling, and as such cannot be said to either true or false until the validation stage. In order to attach meaning to the above equality one must first define the continuum mechanical quantities of velocity, which determines the motion of the volume V , and the density of the material body. Specifically, one implicitly in this modelling stage chooses between a mass-averaged or a molar-averaged velocity, and assumes that the material body fulfills the continuum assumption. However straightforward this may seem, the standard definitions of velocity and density do not preclude the possibility of mass diffusion, or rather mass density diffusion, which has implicitly been abandoned when assuming that $0 = \frac{d}{dt} \int_{V(t)} \rho(\mathbf{x}, t) d\mathbf{x}$. As a matter of fact, we shall see that for our purposes, this equality is not satisfactory. We now turn to a more general approach instead based upon relation (1).

A semi-weak continuity equation on the spatial domain is obtained by taking $\mathcal{X}^t = \rho^t$ in equation (6). No interior sources of mass are present, and thus it remains only to specify the non-advective mass density flux. Considering the types of materials that is most commonly subject to fusion welding, it may be assumed that the base material and filler metal used in the process are similar and homogenous in such a fashion that the density may be evaluated according to the Boussinesq approximation. This assumption is very common in weld pool simulations, c.f. [51, 52, 76, 65, 82, 59, 1, 8, 19, 3, 41], which is feasible since the value of the thermal expansion coefficient ($\sim 10^{-5} K^{-1}$) times the temperature range in the pool ($\sim 10^3 K$) is usually quite small. This implies that mass density diffusion is negligible in the interior of the domain. The flux through the workpiece boundaries however, may be non-vanishing (c.f. section 6.8) and defined in such a fashion that it models the addition of filler metal by spray transfer (see sections 5.2.5 and 6.7 for alternative ways of incorporating the effects of the addition of filler). By specifying the deposition rate $M^t : V(p^t) \rightarrow \mathfrak{R}$ and choosing the smooth boundary mass flux \mathbf{q}_m^t such that $M^t[\bar{p}] = - \int_{\partial\Omega(t)} \mathbf{q}_m^t \cdot \mathbf{n}^t \bar{p}$, we arrive at a modified incompressibility equation for the Lagrange multiplier p^t , that should hold for every $t \in [0, t_{end}]$:

$$0 = -\rho_{ref} \int_{\Omega(t)} \nabla_{\mathbf{x}} \cdot \mathbf{u}^t \bar{p} + M^t[\bar{p}], \forall \bar{p} \in V(p^t)$$

where we write ρ_{ref} for the constant referential (operating) density. If the weld configuration is not very complex, the computational domain Ω_0 can be taken as a rectangle, and consequently Ω^0 is an extension of this rectangle in the Z direction. This simplifies the equations in many ways, and does not restrict the scope of our simulations since we consider in this treatise only fillet joints and butt joints. The part Γ_0^w of the boundary $\partial\Omega_0$ that is mapped onto a subset of

the welding surface $\Gamma_w(t)$ is thus a subset of the $Y = 0$ line, since the referential welding surface $\Gamma_w^0 \subset \partial\Omega^0$ is a subset of the $Y = 0$ plane. We can now take $D = \{(s_1, s_2) \in \mathfrak{R}^2 \mid (s_1, 0, s_2) \in \Gamma_w^0\}$ and $\mathbf{r}(s_1, s_2) = [s_1, 0, s_2]^T$ in equation (5) so that

$$M^t [\bar{p}] = - \int_D \hat{\mathbf{q}}_m(s_1, 0, -s_2, t) \cdot \mathcal{J}_\omega(s_1, 0, -s_2; t) \begin{bmatrix} 1 \\ 0 \\ 0 \end{bmatrix} \times \mathcal{J}_\omega(s_1, 0, -s_2; t) \begin{bmatrix} 0 \\ 0 \\ -1 \end{bmatrix} \bar{p} \circ \omega(s_1, 0, -s_2, t) ds_1 ds_2$$

Now, by assuming that the boundary flux is directed such that $q_{m,1}^t \equiv q_{m,3}^t \equiv 0$, the above integral can be simplified;

$$M^t [\bar{p}] = \int_D -\hat{q}_{m,2}(s_1, 0, -s_2, t) \left(\frac{\partial\omega_1}{\partial X} \frac{\partial\omega_3}{\partial Z} - \frac{\partial\omega_1}{\partial Z} \frac{\partial\omega_3}{\partial X} \right) \bar{p} \circ \omega(s_1, 0, -s_2, t)$$

This simplification is important since we mean to explicitly find and control $M^t [1]$, the total deposition rate. By assuming that the spray intensity $-q_{m,2}^t$ is independent of the y -coordinate, and applying a change of coordinates, we arrive at

$$M^t [1] = \int_{D_w} -q_{m,2}^t(\omega_1, 0, \omega_3, t) d\omega_1 d\omega_3,$$

where D_w is the projection of $\Gamma_w(t)$ on to the plane $y = 0$. The spray intensity is assumed to be Gaussian in the distance from the line through the source center $P(t)$ which is parallel to the y -axis;

$$-q_{m,2}^t(\mathbf{x}, t) = \frac{M(t)}{\pi b^2(t)} \exp\left(\frac{-\|(x, z - P_3(t))\|^2}{b^2(t)}\right),$$

where $b(t)$ is the spray radius at time t . For $b(t) \ll 1$, the factor $M(t)$ is found to be a good approximation of the total deposition rate;

$$M^t [1] = M(t) \int_{D_w} \frac{1}{\pi b^2(t)} \exp\left(\frac{-\|(x, z - P_3(t))\|^2}{b^2(t)}\right) \approx M(t)$$

We find from equation (10) that the material representation of the deposition rate is written as

$$\hat{M} [\hat{p}] = \frac{M(t)}{\pi b^2(t)} \int_{\Gamma_w^0} f \circ \hat{T}(X, 0, t) \exp\left(\frac{-\|(\omega_1(X, 0, t), P_3(t))\|^2}{b^2(t)}\right) \frac{\partial\omega_1}{\partial X}(X, 0, t) \hat{p} dX,$$

where \hat{p} is the material formulation of the test function, and the local liquid fraction f (see section 5.2.4) has been incorporated in order to avoid adding

material to the solid workpiece. If the weld pool is wider than $b(t)\sqrt{-\ln(0.01)}$, the theoretical deposition rate does not deviate more than one percent from $M(t)$.

It should be noted that the filler metal carries also momentum and thermal energy to the pool, as explained by equations (7) and (8). The validity of a globular transfer simulation based on our current approach may be questioned, since we are then for many purposes required to simulate individual droplets. The computational advantage of our current approach, however, should not be underestimated. This was partially verified in [14], where the present approach was appreciated at high welding currents ($\geq 150\text{A}$).

To conclude, the equation we wish to solve is the following;

$$0 = -\rho_{ref} \int_{\Omega_0} \nabla_{(X,Y)} \hat{\mathbf{u}} : \mathcal{J}_\omega^{-T} \hat{\mathbf{p}} |\mathcal{J}_\omega| + \hat{M}^t [\hat{\mathbf{p}}], \forall \bar{p} \in V(p^t) \quad (12)$$

Although the above equation is a result of physical modelling, the incompressibility equation should be considered a pointwise constraint that can be used to simplify the equations for the other quantities of interest. We note thus that the pointwise version of equation (9) can be written as

$$-\frac{1}{v} \frac{\partial}{\partial t} \hat{u}_3 = -\nabla_{(X,Y)} \begin{bmatrix} \hat{u}_1 \\ \hat{u}_2 \end{bmatrix} : \mathcal{J}_\omega^{-T} - \frac{1}{v} \frac{\partial \omega}{\partial t} \cdot \nabla_{(X,Y)} \hat{u}_3 \mathcal{J}_\omega^{-1} \quad (13)$$

Let us note that employing a mass density flux that vanishes in the interior and is discontinuous when approaching the boundary, does not allow for the application of Greens formula, and is thus not necessarily “useful” in the sense that \mathcal{X}^t can be determined from our governing equation. Yet it is the validation of the model that will prove this to be useful or not. As a matter of fact, when discretizing and solving equation (12), the incompressibility condition will be violated close to the boundary in the interior of the domain, c.f. section 5.4.2. This is why we take special measures when solving this equation, see section 6.1.

5.2.3 Balance of linear momentum

A semi-weak equation for the conservation of momentum is obtained upon inserting the densities of the axis-parallel (linear) momenta into (10) and using the incompressibility constraint (not the continuity equation) to remove the divergence term. The volumetric source of momentum, i.e. the force density \mathbf{F}^t , is given rise to mainly by electromagnetic effects and gravity. We have $\mathbf{F}^t = \mathbf{F}_{em}^t + \rho^t \mathbf{g}$, where \mathbf{F}_{em}^t is the electromotive (Lorentz) force density (see section 5.3) and \mathbf{g} is the gravitational acceleration.

According to the Boussinesq approximation, the relative difference between the buoyancy-inducing and operating densities depends linearly on the corresponding temperature difference with a coefficient of proportionality equal to the thermal expansion coefficient β , i.e $\mathbf{F}^t = \mathbf{F}_{em}^t + \rho_{ref} [1 - \beta(T^t - T_{sm})] \mathbf{g}$, where the reference temperature T_{sm} is taken as the mean of the solidus and liquidus points of the material. One may argue about whether buoyant effects

are important. In the absence of other driving forces, buoyancy has a considerable effect on the distribution of heat within the pool via natural convection, only if the Rayleigh number is above a critical value. According to Rayleigh's analysis of convective instability in a pool with a free upper surface (c.f. [13]), this critical value is 1100. For the processes we encounter in this study, the Rayleigh number is far below this value. This is mainly because the length scale (plate thickness) and expansion coefficient are small for a typical process. What more is, the Lorentz forces act to oppose the flow pattern provoked by density gradients, see section 5.3. We incorporate the buoyancy effect for the sake of theoretical completeness. Note however that, since we consider moving boundaries, the gravitational source term cannot be entirely ignored.

In the case $\mathcal{X}^t = \rho_{ref} \mathbf{u}^t$, which is the present, the unknown quantity has as many components as the fluid flow velocity \mathbf{u}^t , and consequently the flux, which is equal to the Cauchy stress σ^t , is a three times three matrix. The boundary integral appearing in equation (6) is thus the total weighted force acting on the boundary, and we represent this by the generalized function $\Gamma^t : V(\mathbf{u}) \rightarrow \mathfrak{R}$. In this work we assume that the influence of the arc impingement is reduced to a pressure on the weld pool surface, i.e. we ignore drag forces. This may be subject to criticism, since it was found in [34] that for a simulated GTA weld pool operated at 200A, it is the arc shear forces in combination with the Marangoni forces that determine the weld pool flow. Yet we ignore arc shear at this stage, and so the total force on the pool surface in the tangential direction is simply the Marangoni force, and for the normal direction, the force is derived using the arc pressure, the surface tension γ^t and the curvature of the surface. Expanding the treatment presented by [71], we have for its spatial representation that

$$\begin{aligned} \Gamma^t[\bar{\mathbf{u}}] = & - \int_{\partial\Omega(t)} [\gamma^t \nabla_S \cdot \mathbf{n}^t] \mathbf{n}^t \cdot \bar{\mathbf{u}} + \int_{\partial\Omega(t)} [\nabla_S \gamma^t] \cdot \bar{\mathbf{u}} \\ & - \int_{\Gamma_w(t)} \frac{P_{arc}(t)}{\pi p_{arc}^2(t)} \exp\left(\frac{-\|(x, z - P_3(t))\|^2}{p_{arc}^2(t)}\right) \mathbf{n}^t \cdot \bar{\mathbf{u}} \end{aligned}$$

where $\nabla_S = (\mathbf{I} - \mathbf{n}^t \mathbf{n}^{tT}) \nabla^T$ is the surface gradient operator, and the same ansatz was used for the arc pressure as for the deposition rate. Hence, the number $p_{arc}(t)$ is the impingement radius of the source, and $P_{arc}(t)$ is the total arc force acting on the weld surface. This force is during the different welding processes exerted for example by the filler metal spray, the plasma, the shielding gas, and impinging electrons. Applying the surface divergence theorem (c.f. [78]) gives

$$\begin{aligned} \Gamma^t[\bar{\mathbf{u}}] = & - \int_{\partial\Omega(t)} \gamma^t \nabla_S \cdot \bar{\mathbf{u}} + \int_{\partial\Omega(t)} [\nabla_S \gamma^t] \cdot \bar{\mathbf{u}} \\ & - \int_{\Gamma_w(t)} \frac{P_{arc}(t)}{\pi p_{arc}^2(t)} \exp\left(\frac{-\|(x, z - P_3(t))\|^2}{p_{arc}^2(t)}\right) \mathbf{n}^t \cdot \bar{\mathbf{u}} \end{aligned}$$

In the above equation, we do not incorporate the contact line integrals that emerges when applying the surface divergence theorem, since the contact line is a Dirichlet boundary on which the velocity vanishes. In some cases the formulation of the problem is simplified by assuming symmetry with respect to the joint plane, and in such cases the line integral vanish also, due to the fact that the velocity is perpendicular to the binormal.

It has been shown (*c.f.* [87, 59, 92]) that the surface tension gradient $\nabla_S \gamma^t$ exercises a dominating influence on the fluid flow in many GTA and laser weld pools. A reasonable assumption is that the surface tension is dependent only on temperature and the presence of surfactants. It has been observed that the addition of an impurity concentration to the liquid pool may reverse the direction of the surface flow (see for example [87]), hence it may be important not to ignore solutocapillary effects. In for example [68, 87, 86, 16, 48, 59] the following expression is employed when evaluating the surface tension:

$$\begin{aligned} \gamma^t(\mathbf{x}) &= \gamma_m - A(T^t(\mathbf{x}) - T_m) - RT^t(\mathbf{x})\Gamma_{sol} \ln(1 + K^\circ(\mathbf{x})a_i) \quad (14) \\ K^\circ(\mathbf{x}) &= k_1 \exp(-\Delta H^\circ / RT^t(\mathbf{x})) \end{aligned}$$

where γ_m is the surface tension at the liquidus point in the absence of surface active elements, R is the gas constant, Γ_{sol} is the surface excess at saturation, K° is the adsorption coefficient, a_i is the activity of species, k_1 is an entropy factor and ΔH° is the standard heat of adsorption. In the absence of surface active elements, $-A$ is simply the temperature coefficient of surface tension. However important solutocapillary effects may be in some situations, one may suspect that expression (14) involves parameters that we cannot determine and is slightly more complicated than is actually required when simulating non-autogenous weld pools. In this study, we therefore assume that the temperature coefficient of surface tension is constant, and set the activity of all species equal to zero.

It should be noted that whenever we speak of a value for the surface tension of a metal, we signify an approximate expression for the liquid metal surface free energy when opposing the adjacent medium which consist in a shielding gas, a plasma, air, or a mix of the three.

The material is modeled as an incompressible Newtonian fluid, and σ^t is hence decomposed into pressure and viscous stress;

$$\sigma^t = p^t \mathbf{I} - \hat{\mu} \circ T^t [\nabla \mathbf{u}^t + (\nabla \mathbf{u}^t)^T],$$

where the effective dynamic viscosity $\hat{\mu}$ is a function of temperature only. Since the mechanical state in the interior of the solid phase is not sought, we may use the same form of the stress tensor in the entire domain by letting the effective dynamic viscosity increase with decreasing temperature. The essential characteristics of the motion of solid phase fluid particles and interdendritic flow can be captured by employing the relation $\hat{\mu}(T) = 10^{10} \left[\frac{\mu_m}{10^{10}} \right]^{f(T)}$, where μ_m is the presumably constant viscosity of the completely molten phase and $f : \mathfrak{R} \rightarrow \mathfrak{R}$ is

the local liquid fraction yet to be specified. It should be noted that a porosity source term, for example the popular Darcy damping term with a permeability function evaluated using the Carman-Kozeny equation (c.f. [59, 43]), cannot instead be used since this would make solidifying overflow wave fronts come to a sudden halt in mid-air.

Assuming that the flow in the weld pool is laminar (c.f. [14, 3, 41], see also section 6.4), we arrive at the following equation by inserting the above expression and the material representation $\hat{\mathbf{u}}$ of the flow velocity into equation (10):

$$\begin{aligned} \rho_{ref} \int_{\Omega_0} \left[\frac{\partial \hat{\mathbf{u}}}{\partial t} + \nabla_{(X,Y)} \hat{\mathbf{u}} \mathcal{J}_\omega^{-1} \left(\hat{\mathbf{u}} - \frac{\partial \omega}{\partial t} \right) \right] \cdot \hat{\mathbf{u}} |\mathcal{J}_\omega| = & \quad (15) \\ - \int_{\Omega_0} \hat{\mu} \circ \hat{T} \left[\nabla_{(X,Y)} \hat{\mathbf{u}} \mathcal{J}_\omega^{-1} + \mathcal{J}_\omega^{-T} (\nabla_{(X,Y)} \hat{\mathbf{u}})^T \right] : \left[\nabla_{(X,Y)} \hat{\mathbf{u}} \mathcal{J}_\omega^{-1} \right] |\mathcal{J}_\omega| & \\ + \int_{\Omega_0} \mathbf{I} \hat{p} : \left[\nabla_{(X,Y)} \hat{\mathbf{u}} \mathcal{J}_\omega^{-1} \right] |\mathcal{J}_\omega| + \rho_{ref} \int_{\Omega_0} \left[1 - \hat{\beta} (\hat{T} - T_{sm}) \right] |\mathcal{J}_\omega| \mathbf{g} \cdot \hat{\mathbf{u}} & \\ + \int_{\Omega_0} \hat{\mathbf{F}}_{em} \cdot \hat{\mathbf{u}} |\mathcal{J}_\omega| + \hat{\mathbf{\Gamma}}[\hat{\mathbf{u}}], \forall \bar{\mathbf{u}} \in \mathbf{V}(\mathbf{u}^t) & \end{aligned}$$

where $\hat{\beta} = f\beta$ is the effective thermal expansion coefficient, and $\hat{\mathbf{\Gamma}}$ is the material formulation of the surface force Γ^t .

5.2.4 Conservation of energy

The total energy is written as $\mathcal{X}^t = h^t + \Delta H^t + \rho^t \frac{\mathbf{u}^t \cdot \mathbf{u}^t}{2}$, where $h^t(\cdot) := \int_{T_0}^{T^t(\cdot)} \rho^t c$ is the sensible enthalpy, $\Delta H^t := \rho^t L f \circ T^t$ is the latent enthalpy, T_0 denotes the constant initial temperature of the workpiece, c is the temperature dependant heat capacity, and L is the latent heat coefficient. The latent heat release rate is given by the local liquid fraction f (since the density is constant, it does not matter if f is a mass fraction or a volume fraction), which in this study is a function of temperature only. At a more detailed modelling level, f could be defined as depending also on the cooling rate, solidification speed and solute concentration. Some investigations such as [88] even solve a differential equation for the liquid fraction, in which the diffusion of the liquid state in the mushy zone is considered. In the present case we employ a local liquid fraction which is piecewise linear, and takes the values 0 and 1 for $T^t < T_s$ and $T^t > T_m$ respectively. Not very often do investigators assume smoother shapes for f , since it turns out that simulations are insensitive to the particular ansatz (at least as long as f is a continuous function of its arguments). In the case when \mathcal{X}^t represents the total energy, the flux is composed from the flux of kinetic energy, which is written $\sigma^t \mathbf{u}^t$, and a number of different types of thermal energy fluxes. Except for the advective flux, we consider only the conductive flux in the interior, and it is modeled by Fourier's law. The boundary flux is convective and radiative. The convective boundary term includes evaporative heat losses using

a combined heat transfer coefficient k_∞^t . Arc heating, such as ohmic heating and convection from a jet, is modelled by a boundary flux expressed using the transferred power $Q^t : V(T^t) \rightarrow \mathfrak{R}$, which is of the same form as the deposition rate and the arc pressure. Since we ignore joule dissipation, no interior sources of thermal energy are present. Furthermore, the interior source of kinetic energy is the work $\mathbf{F}^t \cdot \mathbf{u}^t$, \mathbf{F}^t still denoting mechanical force per volume. Before inserting these expressions into equation (10), it is worthwhile to simplify the pointwise equation. Thus, using the incompressibility constraint and not yet considering the boundary terms, equation (2) now reads

$$\left(\rho_{ref} c + \rho_{ref} L \frac{\partial f}{\partial T} \circ T^t \right) \frac{DT^t}{Dt} + \rho_{ref} \mathbf{u}^t \cdot \frac{D\mathbf{u}^t}{Dt} = -\nabla \cdot [\sigma^t \mathbf{u}^t] - \nabla \cdot [-k \nabla T^t] + \mathbf{F}^t \cdot \mathbf{u}^t$$

where the thermal conductivity k is a function of the temperature T^t only. Rearranging we arrive at

$$\left(\rho_{ref} c + \rho_{ref} L \frac{\partial f}{\partial T} \circ T^t \right) \frac{DT^t}{Dt} + \mathbf{u}^t \cdot \left(\rho_{ref} \frac{D\mathbf{u}^t}{Dt} + \nabla \cdot \sigma^t - \mathbf{F}^t \right) = -\sigma^t : \nabla \mathbf{u}^t - \nabla \cdot [-k \nabla T^t]$$

The second paranthesized expression on the left hand side in the above equation is the pointwise residual for the conservation of linear momentum. Although we do not pointwise fulfil the constraint of conservation of balance of linear momentum, we assume that this residual is small enough to be neglected. Now, we can pose the equation in terms of the temperature T^t , with the viscous dissipation as a source term;

$$\left(\rho_{ref} c + \rho_{ref} L \frac{\partial f}{\partial T} \circ T^t \right) \frac{DT^t}{Dt} = -\nabla \cdot [-k \nabla T^t] - \sigma^t : \nabla \mathbf{u}^t$$

The above equation is an instance of equation (2) with $\mathcal{X}^t = T^t$, $\mathbf{q}^t = -k \nabla T^t$ and $F^t = -\sigma^t : \nabla \mathbf{u}^t$ with the exception that the total derivative term has a weighting coefficient, which is in contrast with the other popular approach in which the effect of the latent heat is incorporated using a source term, as for example in [18]. It can be seen that the derivation of equation (10) is valid even with this coefficient, and so behold

$$\begin{aligned}
\rho_{ref} \int_{\Omega_0} \hat{c} \left[\frac{\partial \hat{T}}{\partial t} + \nabla_{(X,Y)} \hat{T} \mathcal{J}_\omega^{-1} (\hat{\mathbf{u}} - \frac{\partial \omega}{\partial t}) \right] | \mathcal{J}_\omega | \hat{T} = & \quad (16) \\
- \int_{\Omega_0} k \circ \hat{T} \nabla_{(X,Y)} \hat{T} \mathcal{J}_\omega^{-1} \mathcal{J}_\omega^{-T} \nabla_{(X,Y)}^T \hat{T} | \mathcal{J}_\omega | & \\
- \int_{\Omega_0} \hat{\sigma} : [\nabla_{(X,Y)} \hat{\mathbf{u}} \mathcal{J}_\omega^{-1}] | \mathcal{J}_\omega | \hat{T} & \\
- \int_{\partial \Omega_0} \hat{k}_\infty (\hat{T} - \hat{T}_\infty) | \mathcal{J}_\omega \hat{\mathbf{t}} | \hat{T} - \int_{\partial \Omega_0} \sigma \hat{\epsilon} (\hat{T}^4 - \hat{T}_\infty^4) | \mathcal{J}_\omega \hat{\mathbf{t}} | \hat{T} + \hat{Q}[\hat{T}], \forall \bar{T} \in V(T^t) &
\end{aligned}$$

In the above equation, $\hat{c} = c \circ \hat{T} + L \frac{\partial f}{\partial T} \circ \hat{T}$ is the effective heat capacity, \hat{T} is the material representation of temperature, $\hat{\sigma}$ is the material representation of the stress, \hat{k}_∞ is the material representation of the combined heat transfer coefficient, σ is the Stefan-Boltzmann constant, $\hat{\epsilon}$ is the material representation of the emissivity of the workpiece surfaces, \hat{Q} is the material representation of the transferred power, and the ambient temperature is denoted by \hat{T}_∞ . In applications we usually ignore the viscous dissipation (c.f. [51]).

In the above form of the equation for the conservation of energy, we have not made explicit the dependence of \hat{c} on other phase transitions such as metallurgical transitions. This is because the latent heat of solid-solid transformations can be neglected in applications such as those we consider, cf [46].

The total amount of transferred energy can be controlled using the Gaussian form of the surface source, an approach that is almost universally adopted in one form or another. Thus we let Q^t be of the same form as the deposition rate and the arc pressure:

$$Q^t[\bar{T}] = \eta \mathcal{W}(t) \int_{\Gamma_w(t)} \frac{1}{\pi a^2(t)} \exp\left(\frac{-\|(x, z - P_3(t))\|^2}{a^2(t)}\right) \bar{T}$$

The total power transferred by the mechanisms modeled by the above equation is equal to $\eta \mathcal{W}(t)$. The arc efficiency, source power and spot radius $a(t)$, are assumed to be functions of the process parameters such as the voltage, amperage, polarity, arc height, type of shielding gas, and the contact tube to workpiece distance. However, the above form of the surface source of energy, and the alike for the surface pressure and mass density source, may very well be target for serious criticism, since it does not take into account the actual Euclidean distance from the surface to the the electrode tip. It may be argued that at a point on the surface which is close to the tip the energy density should be higher than at a point in a deep cavity directly below the tip. There has been proposed expressions for the source more sophisticated than the above, that takes this into account. For example, [80] successfully applied an expression which took into account the reduction of resistance by the influence of ionistaion. However, the more naive form that we have chosen to apply in our studies have proven to be useful in many applications, and also simpler to work with, and therefore we remain with the above.

5.2.5 Pseudo-fluid workpiece motion

In general, no fluid flow, and thus no advective flux, is allowed through the boundaries of the control domain. That is, we treat the bounding surfaces as being 'impermeable', c.f. section 6.8. The workpiece motion ω is hence required to satisfy the kinematic constraint $\dot{\omega}^t \cdot \mathbf{n}^t = \mathbf{u}^t \cdot \mathbf{n}^t$. This way the current configuration allows us to extract the shape of fluid surfaces. Specifically, we can extract the outer geometry of the weld as it solidifies. No other condition based on physical considerations can be imposed on ω , and equations for the motion are instead defined such that they satisfy computational requirements. It is well-known that solving the Laplace equation for the mesh velocity $\dot{\omega}$ gives rise to a non-singular motion, i.e. a motion that satisfies the geometric conservation law (c.f. [6]). Since the kinematic constraint is a Dirichlet constraint on an a priori unknown combination of the solution variables representing the mesh velocities in two linear independent directions, it is in our current setting implemented using a Lagrange multiplier $\lambda^t : \partial\Omega^t \rightarrow \mathfrak{R}$ (we will discuss this approach extensively in section 6.6). Although the use of a Lagrange multiplier is a computational issue, we find it appropriate to include it already in this section, and so prepare ground for the further discussions in sections 6.8 and 6.2! Thus, we wish to find the unique pair $(\dot{\omega}^t, \lambda^t) \in V(\dot{\omega}^t) \times V(\lambda^t)$ that makes the following Lagrangean stationary;

$$\mathcal{L} [\bar{\omega}^t, \bar{\lambda}^t] = -\frac{1}{2} \int_{\Omega^t} \mu_{mesh} \nabla_{\mathbf{x}} \bar{\omega}^t : \nabla_{\mathbf{x}} \bar{\omega}^t + \int_{\partial\Omega^t} \bar{\lambda}^t (\mathbf{u}^t - \bar{\omega}^t) \cdot \mathbf{n}^t \quad (17)$$

It should be noted that using this technique we effectively attach the workpiece motion to the motion of an inertia-less fluid, the stress in which can be expressed simply as the the gradient of the velocity of the motion times a factor μ_{mesh} . This is why we refer to the mesh as a *pseudo-fluid*, and to the function μ_{mesh} as the *mesh viscosity*. We note also that since the constraint is on the mesh velocity and not on the configuration ω , it is not straightforward to implement a model in which we instead calculate the deformation of what may be called a *pseudo-solid*. By following the standard argument of introducing arbitrary multiples of variations in equation (17), and differentiating with respect to these, we find that we must require that the relations

$$0 = - \int_{\Omega_0} \mu_{mesh} \left[\nabla_{\mathbf{x}} \frac{\partial \omega}{\partial t} \mathcal{J}_\omega^{-1} \right] : [\nabla_{\mathbf{x}} \bar{\omega} \mathcal{J}_\omega^{-1}] |\mathcal{J}_\omega| + \hat{\Gamma}_\omega [\bar{\omega}] \quad (18)$$

$$0 = \int_{\partial\Omega_0} (\hat{\mathbf{u}} - \frac{\partial \omega}{\partial t}) \cdot \hat{\mathbf{n}} \bar{\lambda} \quad (19)$$

hold for every $(\bar{\omega}, \bar{\lambda}) \in V(\frac{\partial \omega}{\partial t}) \times V(\hat{\lambda})$, where $\hat{\Gamma}_\omega : V(\frac{\partial \omega}{\partial t}) \ni \bar{\omega} \rightarrow - \int_{\partial\Omega_0} \hat{\lambda} \bar{\omega} \cdot \hat{\mathbf{n}} \in \mathfrak{R}$ is the material formulation of the such force acting on the surface of the pseudo-fluid that makes the solution $\dot{\omega}$ fulfill the kinematic constraint. The attentive reader would by now have noticed that the absence of a surface Jacobian in the equation for the multiplier implies that we actually constrain the material

representation of the mesh velocity, and not the spatial representation. The analysis is still valid, and we have experienced that this approach is efficient.

As an alternative to having the surface move as a result of adding mass in the continuity equation, one may modify the velocity of the boundary in the expression for $\tilde{\Gamma}_\omega$, thus relaxing the kinematic constraint. This way, the motion of the free surface is not a result of simulating the response of an incompressible material to a mass source, but the motion of the moving surface is instead detached from the physical fluid, thus allowing for a fluid flow that is, due to the action of arc pressure and droplet momentum transfer, mainly directed towards the bottom of the pool, even as the weld surface is elevating. The two approaches will undoubtedly produce different outputs. So far we have experienced that the approach we have described above and which we for now continue to follow in this treatise, in a number of cases computationally outperforms the approach employing a modified $\tilde{\Gamma}_\omega$. As an example, we noticed that the alternative approach does not converge for the case depicted by the rightmost circle in figure 4.

The mesh viscosity which can be used to improve the mesh deformation. Generally, the mesh viscosity is taken to increase with decreasing element size, so that small elements are less distorted. The workpiece motion will be discussed further in section 6.2.

5.3 Electromagnetics

During many electric arc welding process, the magnitude of the Lorentz force \mathbf{F}_{em}^t acting in the liquid metal is great compared to buoyancy and surface tension forces. The magnitude of the Lorentz force typically increases with the magnitude of the current that is passed thorough the workpiece, and above a certain amperage, the electrodynamic of the process governs entirely the weld pool flow. \mathbf{F}_{em}^t can be determined from the electric field and magnetic field present in the workpiece. For many electric arc weld pool flows the magnitudes of the length scale and flow velocities are quite small in comparison to the magnetic diffusivity. In such cases, the influence of the weld pool flow field on the magnetic field can safely be ignored, and the electric and magnetic fields can be assumed to be governed by the Maxwell equations with the magnetohydrodynamic (MHD) approximation for flows at low magnetic Reynold numbers. These equations are derived in explained in for example [13]. In essence, the simplifications of the full Maxwell equations are possible because it is assumed that magnetic field induced by the motion of the conducting liquid is small in comparison to the imposed magnetic field, which is due to the flow of current through the arc and workpiece, and it is in alignment with our modelling strategy to assume that this imposed field is steady.

In [13] the major characteristics of electromagnetically driven flows in cavities, such as weld pools, are summarized. For a hemispherical pool and axisymmetric fields, it is easy to derive a solution for the simplified MHD equations that show that the Lorentz force, in cases when the applied current is directed into the workpiece, is directed radially inwards and decreases in magnitude to-

wards the base of the pool. Consequently, the flow field is directed towards the bottom of the pool near the symmetry axis. We note that this field carries mass and thermal energy from the hot impinging spot of the electrode, towards the deepest part of the pool, and thus promotes penetration. The phenomena that causes this type of flow field is known as the *pinch effect*. The pinch effect acts in weld pools of arbitrary shapes, and the penetrating effect of electric current is an established phenomena in all direct current electrode negative welding processes. The digging effect of the electrons impinging on the pool surface adds to this effect.

Under the restricting circumstances explained above, [51] presented analytical expressions for the Lorentz force considering a stationary arc, symmetrically impinging on the flat weld surface of a semi-infinite workpiece. These expressions have subject to extensive use in the history of weld pool simulations, see for example [82, 59]. The work carried on in [52], in which a workpiece of finite thickness was considered. The expressions for \mathbf{F}_{em}^t involves the integration of exponentials and Bessel functions. However, under the assumption that the incident current on the weld surface is concentrated to a single point, the expression for the semi-infinite workpiece can be simplified into one that is more straightforward to evaluate, see [51]. In order to account for moving weld pool boundaries and arcs, this expression must be modified. If the deformation is not great, this can be done simply by replacing the spatial coordinates by material coordinates and transforming the force components into our cartesian coordinate system. The force contribution is

$$\mathbf{F}_{em}^t(\omega(\mathbf{X}, t), t) = \frac{I^2 \mu_B}{4\pi^2 r_1^3} \left(1 + \frac{Y}{r_1}\right) \left[\frac{XY}{r^2}, -1, \frac{Y(Z - P_3(t))}{r^2} \right]^T$$

where

$$\begin{aligned} r &= \sqrt{X^2 + (Z - P_3(t))^2} \\ r_1 &= \sqrt{X^2 + Y^2 + (Z - P_3(t))^2}, \end{aligned}$$

and μ_B is an effective magnetic permeability of the weld, which is assumed constant. The above expression was applied by the author in [24], but the results were not entirely satisfactory. It is believed that this is predominantly due the idealized radius of the incident current spot, and that the geometrical approximation inherent in the expression is not valid in applications such as those, in which the weld surface underwent great deformation. What more is, the motion of the pseudo-fluid has an impact on the force, which is not physical.

[76] proposed an expression (c.f. [53]) that takes into account the finite thickness of the base plate (h_0) and also allows for a strictly positive radius $\sigma(t)$ for the incident current j , which in a cylindrical (r, z, θ) -coordinate system is assumed to be of the form

$$j(r) = \frac{I}{\pi \sigma(t)^2} \exp\left(-\frac{r^2}{\sigma(t)^2}\right)$$

The expression was derived under assumption that the through thickness current density and the θ -component of the magnetic flux density varies linearly with the distance from the weld surface. Furthermore, the r -component of the current density was taken as an average value through the thickness of the workpiece. Still, a flat weld surface was considered. In [22], the author applied the expression in a deformed workpiece by replacing the spatial coordinates by material coordinates. We get

$$\mathbf{F}_{em}^t(\omega(\mathbf{X}, t), t) = F_1^{em} F_3^{em} F_4^{em} \left[F_2^{em} F_4^{em} X, \frac{I}{2\pi h_0} F_3^{em}, F_2^{em} F_4^{em} Z \right]^T \quad (20)$$

where

$$\begin{aligned} F_1^{em} &= -\frac{\mu_B I}{2\pi r^2} \\ F_2^{em} &= j(r) \\ F_3^{em} &= \left(1 - \exp\left(-\frac{r^2}{\sigma(t)^2}\right) \right) \\ F_4^{em} &= \left(1 + \frac{Y}{h_0} \right) \end{aligned}$$

It has since then been noticed that this expression for the force can be extrapolated outside the rectangular domain without changing its characteristics. Hence it is possible to use spatial coordinates instead of material coordinates. This avoids attaching physical meaning to the mesh motion, but it also implies another degree of approximation. Since we find mesh independence to be a very important feature, and we often consider bead-on-plate simulations in which deformations are small, the above expression with spatial coordinates inserted is the one we have continued to employ throughout the studies presented in this treatise.

However practical these expressions are, a more realistic approach is perhaps to consider the effects of boundary layers in the weld pool. Referring again to [13], we find that this makes the treatment of the flow more complicated. Furthermore, the flow can usually not be assumed steady, since it becomes unsteady at Reynolds numbers in the order of 10, and that it is also sensitive to the behaviour of the the magnetic field imposed by the arc. Considering this, we are content with the analytical expression until a coupling with an arc model is provided. The next step in the refinement of the electromagnetical force simulation is to first calculate the potential from the steady-state electric potential equation and then calculate the electric field and also obtain the magnetic field from the Biot-Savart law, as in [43]. In connection to this we note that the article [48] presents simulations in which such a potential equation is solved on a domain that changes shape with time due to the deformation of the pool surface.

5.4 Pre-studies

A number of issues were raised during the derivation of the mathematical model for the weld pool. The purpose of this section is to resolve these issues by investigating into the behaviour of the model in certain model cases, and so hint on what to expect when applying the model in realistic simulations. The computational model we employ during these investigations is as explained in section 6.

5.4.1 2D time dependent vs. 3D steady state

It is natural to ask what impact the assumption that the flux vanishes in the welding direction has on the result of a simulation of a typical weld pool, that is, we would like to compare the formulations (10) and (11) with respect to pool size and shape. This we do for a number of simplified cases, in which we calculate only temperature and ignore dissipation, and thus assume that the workpiece is undeformed and that the flow velocities vanish with respect to reference frame fixed with respect to the workpiece. This reduces the convective field in the 3D simulations to a single component in the opposite direction of the arc velocity, and that compressible effects disappear.

The cases we consider are equal except that we treat the arc speed as a parameter, and they simulate a set of linear-bead-on-plate welding sequences on 6mm thick 304 stainless steel plates. Figures 1 and 2 graph the depths and lengths of the weld pools calculated using the 2D time dependent formulation measured as percentages of the depths and lengths calculated using the 3D steady state formulation. Equation (9) hints that the effects of the flux in the direction of the weld, in this case heat conduction, decreases with increasing arc speed. Since we apply the same heat input in the different simulations but in the 2D formulation remove a way for the energy to spread in the workpiece, we expect the 2D pools to be shorter and more shallow than their counterparts. We see that the simulations verify these trends. It is also worth noticing that the maximum temperature in the pool is predicted quite well even for low arc velocities, see figure 3.

Our conclusion is that, for this model case, we may trust the predictions obtained using the 2D if the arc speed is greater than approximately $0.020m/s$. In simulation cases where the arc velocity is significantly slower, this study does not assure that the pool geometry will not deviate significantly from the one that would have been obtained using a model that considers three spatial dimensions. In preparing the model for such applications, we have tried adding in the governing equations a conductive flux in the welding direction. In doing so, the second time derivative of the temperature appears. This acceleration completely changes the nature of the equations system, and in fact, the theory we have developed is intended to avoid this behaviour. Accordingly, the implementation we have worked with during this project does not function well for such a formulation, and none of the calculations based upon it have converged.

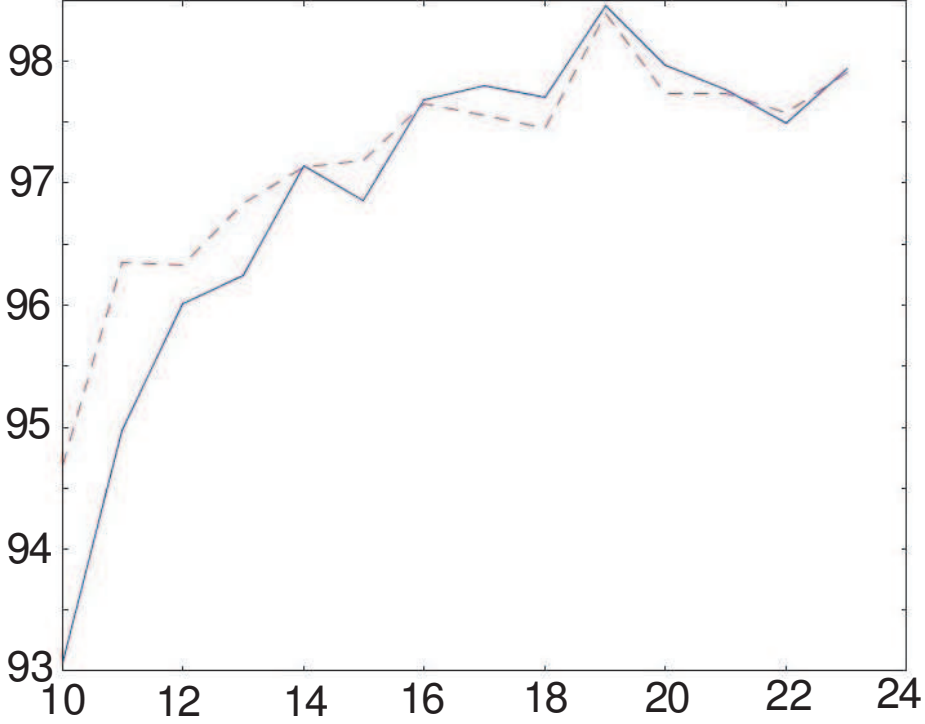


Figure 1: Pool depth (percent) versus arc speed (mm/s). The solid line represents the solidification boundary of the pool, while the dashed line represents the melting boundary.

5.4.2 The influence of filler metal heat transfer on the melting efficiency

As explained by equation (6), our model employs an energy equation the spatial representation of which contains the source term $-\int_{\Omega(t)} \left(h^t + \Delta H^t + \rho \frac{\mathbf{u}^t \cdot \mathbf{u}^t}{2} \right) \nabla \cdot [\mathbf{u}^t - \dot{\omega}^t] \phi^t$. If we thermally insulate the surfaces and ignore the viscous dissipation, the temperature field we calculate should satisfy the following equation for the thermal energy $h^t + \Delta H^t$;

$$\begin{aligned} & \frac{d}{dt} \int_{\Omega(t)} (h^t + \Delta H^t) \phi^t + \int_{\Omega(t)} (\mathbf{u}^t - \dot{\omega}^t) \cdot \nabla (h^t + \Delta H^t) \phi^t = \\ & - \int_{\Omega(t)} (h^t + \Delta H^t) \nabla \cdot [\mathbf{u}^t - \dot{\omega}^t] \phi^t - \int_{\Omega(t)} k \nabla T^t \cdot \nabla \phi^t + Q^t[\phi^t] \end{aligned}$$

As remarked in the discussion of equations (7) and (8), assuming that the incompressibility condition is not violated, adding mass to the workpiece would not increase its thermal energy content. This implies that the temperature of the workpiece must undergo a net decrease in temperature as mass is added.

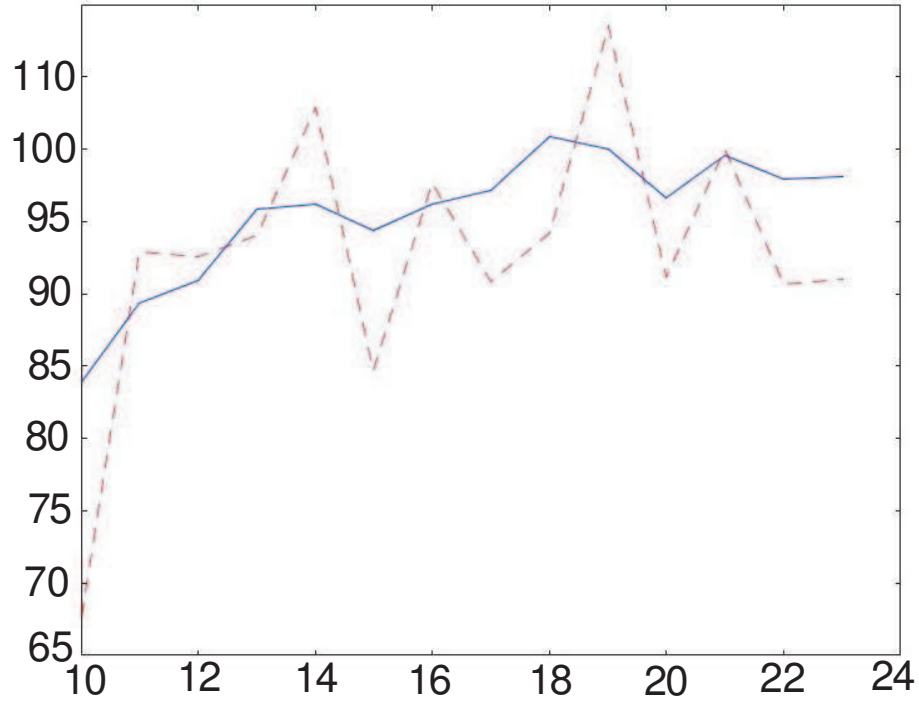


Figure 2: Pool length (percent) versus arc speed (mm/s). The solid line represents the solidification boundary of the pool, while the dashed line represents the melting boundary.

This however does not happen, which is obvious from simulating a test case in which the workpiece is initially fluid and in which we apply no heat source, but add material. Hence the incompressibility condition was violated. Yet we ignored the thermal energy sink which in compressible cases equilibrates the source of thermal energy that is due to the expansion of the material, i.e. the compressibility term $\int_{\Omega(t)} (h^t + \Delta H^t) \nabla \cdot \mathbf{u}^t$. Since the amount and distribution of thermal energy is crucial in welding, it is important to know what influence the compressibility source has on the outcome of a simulation. As mentioned, the source is nonlinear in the thermal energy, but this has the effect that the heat transfer by mass increases with the temperature of the pool, which at least seems natural.

In order to quantify the influence of the heat input to the workpiece that is due to the addition of filler metal, and compare it to the significance of the boundary source term in the energy equation, we study the effect that the heat input resulting from the presence of the nonlinear source term has on the melting efficiency predicted by the simulation. We define the melting efficiency H_{melt} of a steady-state linear welding process as the ratio of the

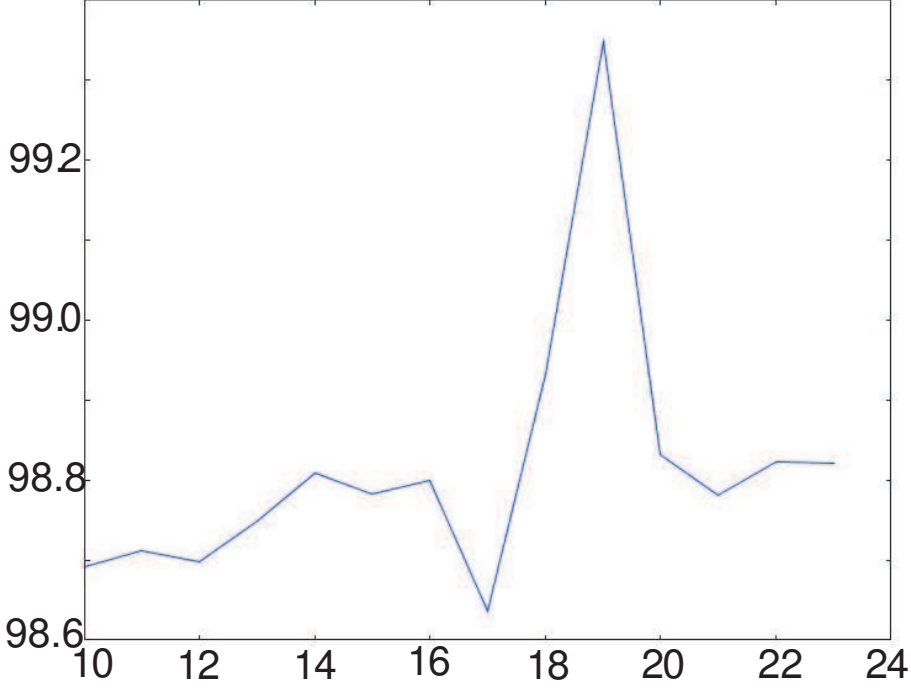


Figure 3: Maximum pool temperature (percent) versus arc speed (mm/s).

theoretical minimum amount of energy required to establish the weld pool and mushy zone to the total amount of thermal energy contained in the workpiece. Melting efficiency is sometimes defined in terms of cross-sectional areas and heat input per unit length (c.f. [60]), but since we assume a mushy zone of considerable size, this definition is awkward. Note however, that if we thermally insulate the surfaces of the workpiece during the simulation, the total energy contained in the workpiece is the same as the heat input to the workpiece, but since our model precludes the possibility of having heat escape in the welding direction, insulating the boundaries may increase the heat per unit length in every cross-section indefinitely. Thus we choose not to insulate the surfaces. This implies that we can expect H_{melt} to depend upon k_{∞}^t , however the heat transfer coefficient is fixed throughout this study.

We have that

$$H_{melt} = \frac{\int_{\Omega(t)} Lf \circ T^t + \int_{\Omega_{mz}(t)} \int_{T_0}^{T^t} c + \int_{\Omega_w(t)} \int_{T_0}^{T_m} c}{\int_{\Omega(t)} \left[Lf \circ T^t + \int_{T_0}^{T^t} c \right]} \quad (21)$$

This ratio was calculated for a number of typical linear (steady state) bead-on-plate welding processes (on steel 316 plates), the parameter settings of which

were the same, except that we between the runs modified the deposition rate. This way we may study the dependence of the melting efficiency on the reinforcement size, which we measure as the volume of reinforcement per length, i.e. its cross-sectional area. We obtained nine data points in the range $0\text{mm}^2 - 4\text{mm}^2$, see figure 4. An immediate result is that we may verify that our model behaves

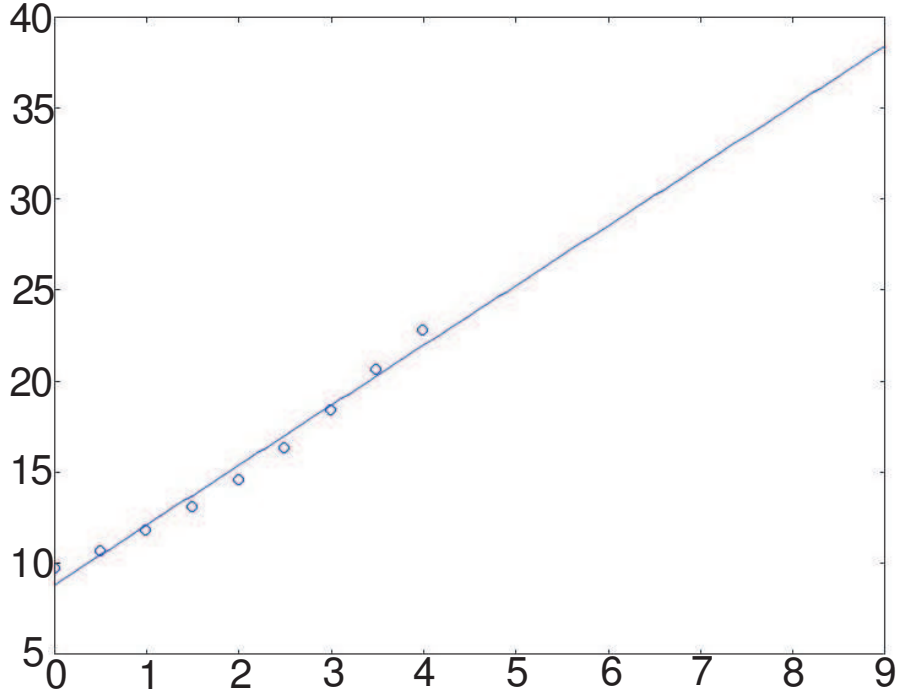


Figure 4: Obtained melting efficiencies (circles) and a quadratic least squares fit plotted against the reinforcement cross-sectional area (mm^2).

qualitatively correct in that the melting efficiency increases with the actual heat input to the workpiece (c.f. [20]) which is strongly affected by the deposition rate. By extrapolating a quadratic least squares fit, we find that the performed parameter study predicts that, for a higher deposition rate, our model would simulate a melting efficiency the size of which agrees with what is usually experienced during non-autogeneous arc welding (40-50 percent, see for example [20]).

Lets return to the discussion following equation (8). The main question is why assume a pointwise solenoidal velocity field, and use this property when simplifying the equations, even though the velocity field approximated by the computational model is expected to be at most merely discretely divergence-free? In applications in which the incompressibility term is close to zero, this assumption does not significantly influence the result, but in our setting the incompressibility condition is severely violated. We have seen that the moving

boundary itself does not influence the heat content of the workpiece, however the divergence of the velocity that it causes was ignored. In order to verify that the heating effect of the deposited material is actually an effect of the incorrect assumption of a solenoidal velocity field, we compare two typical welding simulation cases which differ only in that one of them includes the compressibility source. In these cases we insulate the workpiece surfaces, which implies that the heat content (energy) in the computational slice should tend to the theoretical energy input, if the model conserves energy globally. The heat content in the computational slice calculated using the model ignoring the compressibility source is plotted against time in figure 5. The heat content calculated using the model taking into account the compressibility source is plotted against time in figure 6. It is clear that it is the decompression of the material that gives rise to the artificial heat source that we hitherto have chosen to ignore. As the source passes at time $t = 5$, the workpiece slice that we observe experiences an increase of energy due to the addition of mass and application of the heat source, and when using the model with the compressibility source we see that the energy content remains above 99% of the theoretical heat input after the source has passed.

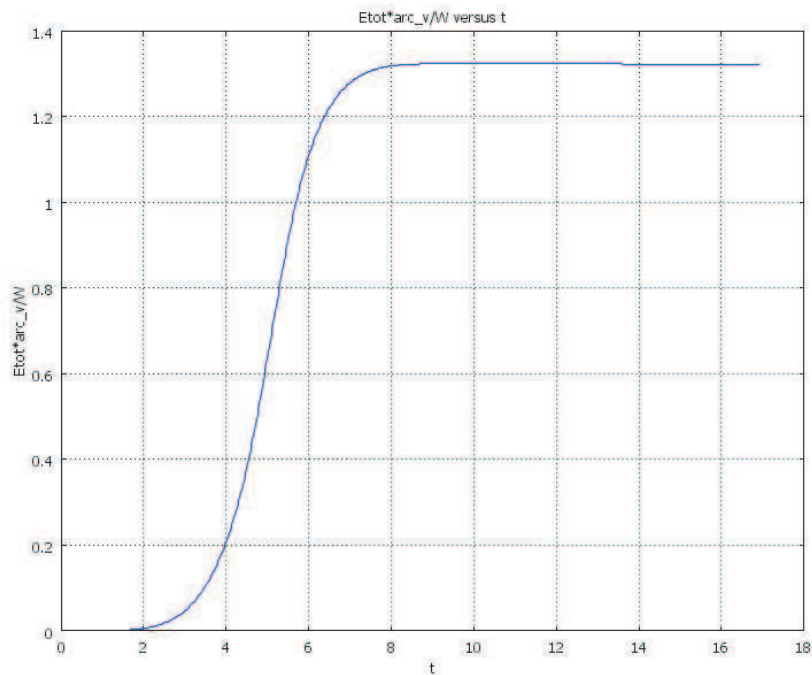


Figure 5: Heat content (measured as the ratio of the heat content in the computational slice to the theoretical total heat input) against time (s), ignoring compressible effects.

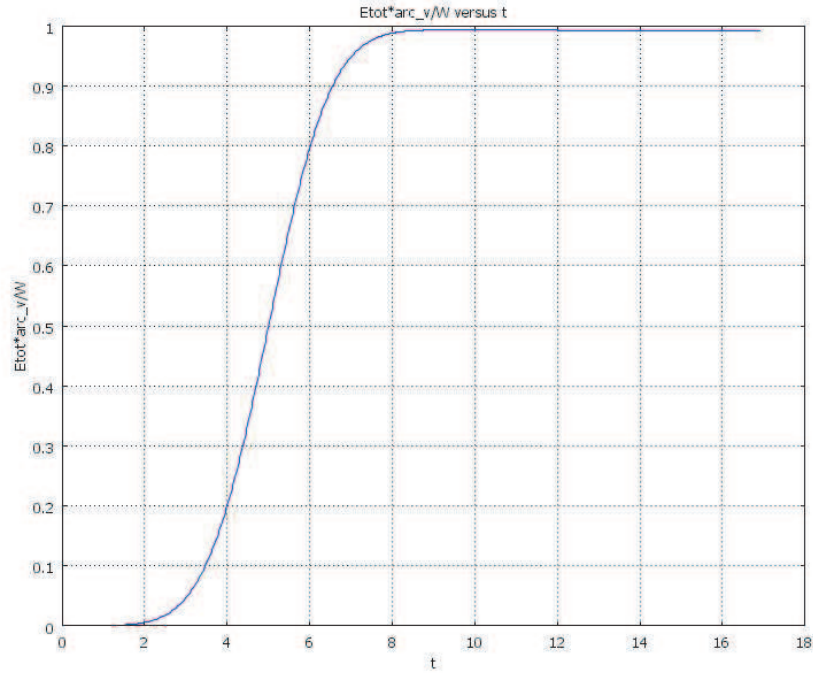


Figure 6: Heat content (measured as the ratio of the heat content in the computational slice to the theoretical total heat input) against time (s), taking into account compressible effects.

The results presented in this and the previous sections are important for appreciating the behaviour of the model, and what more is we can now bring closure to the question we have posed several times before; What is the momentum and energy of the material added to the simulated weld pool? The answer is that we cannot know this beforehand. It is difficult to get around this when insisting on employing a one-phase model such as the one we have proposed. However, it is, as we have seen, simple to neutralize the effect of the decompression on the energy input that follows upon a mass deposition in the pool. We simply include the compressibility source in the energy equation. Since it is often so that an experiment we seek to mimic, or a specification for a simulation, gives a quantity such as the path energy or the net total heat input, it is much more straightforward to use the model if compressible effects are taken into account. Hence we decide for now to continue using the modified model that includes the compressibility source in the energy equation. The momentum source given rise to by the metal spray is yet to be analyzed.

A real-life case in which this modified model displays its impeccable global energy conservation property was considered in a related project on metal deposition.

6 Computational Modeling of Weld Pools

In this section we develop a computational model for the governing equations, and discuss a number of alternative approaches to the problem. The discretization is performed using a finite element method.

6.1 Pseudocompressibility

It can be realized that the compressibility condition will be violated in the interior of the domain and cause a loss of or increase in mass. Since our computational model is partly meant to aid in predicting reinforcement size and geometry, the conservation of mass is essential. We therefore implement a pseudo-compressibility method by adding to the continuity equation a Petrov-Galerkin regularization term, i.e. a small artificial flux in the direction of the negative pressure gradient. Also, in order to obtain further relaxation of the incompressibility condition, a penalization term is added to the spatially represented continuity equation, resulting in the following computational version of equation (12):

$$\begin{aligned}
 0 &= -\rho_{ref} \int_{\Omega_0} \nabla_{(X,Y)} \hat{\mathbf{u}} : \mathcal{J}_\omega^{-T} \hat{p} | \mathcal{J}_\omega | & (22) \\
 &- \epsilon \int_{\Omega_0} \nabla_{(X,Y)} \hat{p} \mathcal{J}_\omega^{-1} \mathcal{J}_\omega^{-T} \nabla_{(X,Y)}^T \hat{p} | \mathcal{J}_\omega | - \epsilon^2 \int_{\Omega_0} \hat{p} \hat{p} | \mathcal{J}_\omega | + \hat{M}^t [\hat{p}], \forall \hat{p} \in V(p^t)
 \end{aligned}$$

where ϵ is the constant relaxation parameter. It is reasonable to let the value of this parameter be dependent upon the mass added per unit length and unit time as the source passes over the computational slice, i.e. it is dependent upon the mass density, the deposition rate, and the interaction time for a pool surface particle in the joint plane. Thus we assume $\epsilon = \epsilon(\rho_{ref}, M, v, b)$. We note that this assumption is in contrast with the standard approach of having the relaxation vanish with decreasing mesh size. By interpreting the pressure flux in a physical way, we see that in order to render the Petrov-Galerkin regularization term dimensionally consistent, the relaxation parameter must have the dimension of time. By dimensional analysis we find that an appropriate ansatz is $\epsilon = C_\epsilon \frac{M}{\rho_{ref} v^2 b}$, where C_ϵ is a dimensionless constant. The value of C_ϵ will be calibrated in section 7.1. As is apparent from equation (22), the value of the factor in front of the penalization term is assumed to be the square of ϵ .

A reason for employing the penalization method is usually that the pressure variable does not need to be calculated. However, our model does not exploit this opportunity since the deposition of mass requires that we solve the continuity equation for the pressure. There is a theoretical possibility of inserting the weighted integral of the pressure from the continuity equation into the equations for the fluid flow velocity, thus incorporating the boundary source. We have tried this option, but it does not work very well, the fluid remains incompressible and no material can consequently be added. The reason for this is thought to be that

the penalization is too rigorous for the boundary source to have an effect on the divergence of the flow field.

6.2 Mesh moving techniques

We must decide upon what equations to solve for the motion. Choosing $\hat{\mathbf{u}} = \frac{\partial \omega}{\partial t}$, as in the classical Lagrange approach, eliminates the convection term in equation (4). This approach is often a good choice for solid mechanical simulations, but it is rarely successfully applied within the field of CFD. The other extreme is the Euler approach, in which the motion vanishes. Since in the Eulerian approach the mesh is not at all distorted, this approach cannot be used to track moving surfaces unless we employ a CSF formulation. Attempting to exploit the good characteristics of either two of the above extremes, we choose to employ a pseudo-fluid mesh moving technique with mesh size dependent viscosity, i.e. we solve equation (18) with $\mu_{mesh} = \mu_{mesh}(h)$, where h is a measure of the local element size. Specifically, we set

$$\mu_{mesh}(h) = 1 - h$$

We also tried using an exponentially increasing mesh viscosity, but for a number of test cases we obtained shorter simulation times using the above formula. This is probably due to the extreme viscosity gradients that appear when employing the former approach.

It is well worth mentioning another mesh moving technique that we also tried. If the location of the moving surface can be represented as the graph of a single-valued function h_s giving the displacement of the surface in a specified direction measured from a reference plane or point, then the *method of spines* (c.f. [70]), also known as the *height function method*, is applicable. This method reduces the complexity of the system of equations, since the motion of the entire workpiece can be expressed via the single unknown h_s , which is defined only on the free surface. For example, if the workpiece consists of a plate of thickness h_0 , and the surface is spatially described by $\Gamma_w(t) = \{(x, h_s(x, z, t), z) : (x, 0, z) \in \Gamma_0^w\}$, then

$$\omega(\mathbf{x}, t) = \begin{bmatrix} 1 & 0 & 0 \\ 0 & 1 + \frac{h(x, z, t)}{h_0} & 0 \\ 0 & 0 & 1 \end{bmatrix} \mathbf{x} + \begin{bmatrix} 0 \\ h(x, z, t) \\ 0 \end{bmatrix}.$$

and in two dimensions we have a formula for \mathcal{J}_w involving only a derivative of h_s . If one wishes to simultaneously perform tracking of two different boundaries such as the liquid-solid and liquid-gaseous or root side workpiece boundaries of a nicely behaving weld pool, the akin *Landau transformation* (c.f. [75, 83]) is appropriate. The method of spines reduces system complexity, but even for small deformations we have experienced that the convergence is very slow, probably due to the severe deformation of the elements. What more is, it cannot be used to represent an extremely deformed surface such as the weld pool surface during overflow.

6.3 Dimensional analysis

During electric arc welding it is in general so that the relative importance of the forces driving the fluid flow is such that the electromagnetic force exercises the dominating effect, followed in decreasing order by Marangoni and gravitational forces. It would be a great advantage to know beforehand if any of these forces can be neglected and thus ignored during a simulation. Likewise is it advantageous to know whether heat transfer occurs predominantly by conduction or convection. Our modelling strategy compels us to calculate the fluid flow and convection, and conduction must also always be considered else the base material would not melt, but simulation results can aid in understanding the phenomena occurring in the real weld pool. For example, during LBW the Marangoni force is the main driving force, and the direction of this force can be modified by adding a surface-active element which causes the gradient of surface tension to change direction. This method can thus be used in order to achieve higher penetration (c.f. [17]), however only when the Peclet number is large, which signifies that the heat transfer that determines the interior pool shape occurs predominantly by convection. Simulations can be used in order to approximate the fluid flow velocity in the pool and thus verify or falsify that this is in fact the case. Although the Peclet and other dimensionless numbers would preferably be known beforehand, it is difficult to calculate such without enough information about the thermodynamical state of the workpiece during the welding sequence. Since we do not have this information a priori, we let our simulation tool output the important quantities, and these can be used for approximating the values of the dimensionless numbers during similar simulations, for example those subsequent in a parameter study.

The calculation of the weld pool flow Reynolds numbers and turbulence modelling is discussed in section 6.4.

6.4 Laminar vs. turbulent modelling

Both experimental, numerical and theoretical attempts have been made to approximate the Reynolds number for different weld pool flows. The prediction of course depend on the welding process and parameters, but even for similar situations the results diverge. Since it has proven difficult to establish a critical Reynolds number for a weld pool flow, it generally remains an open question whether a flow should be treated as laminar or turbulent. There have though been performed studies that compare simulations using laminar models to simulations using turbulent models, and the results indicate what modelling strategy should be pursued.

In [40] it was noticed that laminar models tend to overestimate the depth of the actual weld pool. There was conveyed a comparison between the measured and predicted weld pool shapes using a laminar and a $k - \epsilon$ turbulent model. It was found that, for the specific case, turbulent models are more accurate. However, when approaching the solid-liquid interface, the level of turbulence was seen to decrease to a size that predicts laminar flow. It can thus be suspected

that ignoring turbulent effects in the center of the pool may result in a laminar model that overestimate the pool depth. This can be explained by the fact that the thermal energy density in the fluid is high close to the center of the pool surface, i.e. directly under the center of the arc, and the flow pattern induced by Lorentz forces transport this thermal energy towards the root side and provokes weld penetration. This effect is not as emphasized when turbulence is present, since in a such flow the diffusion of thermal energy away from the center is more enhanced, and the temperature of the fluid that is transported to the bottom center of the weld pool is thus reduced (c.f. [85] where it was found that “the dissipation of heat and momentum in the weld pool is significantly aided by turbulence”). This effect is verified by the isotherms presented in [40].

In [8, 9] it is on the other hand argued that turbulent thermal diffusion may increase the depth of the pool. This effect is however limited by the enhanced diffusion of momentum which reduces the flow velocities, and thus the convective transport of heat, towards the root side.

There is no definite advantage of employing a turbulent modelling approach in our present work, and hence we choose for now to continue using the laminar model.

6.5 The DASP algorithm and implementation details

We employ the DASP algorithm ([4, 5]) for solving the differential-algebraic systems obtained from the finite element discretization of the equations. The numerical method was implemented using the software COMSOL Script. The input to the software consists in a source file, which primarily contains the specification of the weak form of the governing equations and of the corresponding elements. Also, the choice of linear system solver and corresponding settings are specified in the source file. Due to limited computing power, the computational models considered in this treatise are all of moderate size, and we have experienced that the direct linear solver outperforms the iterative solvers supplied by COMSOL script. We use the linear solver UMFPACK.

The DASP algorithm requires the user to supply the value of the weights that define the weighed norm which is used to determine convergence. The relative tolerance and the absolute tolerance are discussed in section 6.6. Their values are generally set some magnitudes lower than those values recommended in [4] as the starting guesses in the process of finding an application specific optimization of the code performance.

Some intricate issues have taken up much of the authors time. For example, tangential derivatives are analytically and numerically equivalent to the projection of the gradient on the tangential direction. However there seems to be a difference in the implementation of the two since the latter gives rise to highly irregular surfaces when employed in the formulation of the partially integrated surface tension term, while the former does not. We have also tried normalizing the equations with respect to ρ , but we have found that the built-in scaling performed by the code is generally more efficient.

6.6 A GMA fillet weld case study

We now apply the developed tool to the simulation of a GMA fillet weld pool. The purpose is to extract important information about the behaviour of the tool, before proceeding to its calibration. [91] (as well as [47] and [57] in a similar fashion) gives a specification of a three dimensional steady state GMA fillet weld simulation, although lacking in the value for the latent heat coefficient of the A-36 mild steel, the workpiece and spatial domain dimensions, and the incident current radius. What more is, the [91] model predicts the surface shape by minimizing a surface energy functional under mass conservation conditions, and hence does not make use of a mass source. Hence we must choose b . This we do by restricting the mass source radius to the weld pool, so that no mass is deposited onto the solid workpiece. The value $b = 0.2a$ is assumed to suffice. We calculate the total deposition rate from wire dimensions and feed rate. By setting L to the value of the latent heat coefficient for pure iron, approximating the workpiece dimensions from the figures in [91], and setting the incident current radius $\sigma = b$, we may specify all input values required in order to obtain a corresponding simulation using our tool. We note that the arc current is high enough (362A) to enable the assumption of spray transfer (c.f. [85] and [50]).

Furthermore, our tool does not apply a Dirichlet condition for the temperature at the butt sides of the workpiece, but instead applies the convective heat transfer condition using the value 10^{10} for the effective heat transfer coefficient. Finally, the model for the electromotive force in [91] is as in [52], which, as previously explained, differs from the expression we apply in this study.

According to the results obtained in section 5.4.1, it is possible that our model will underestimate the size of the pool, since the arc speed is only $0.0042m/s$. In preliminary simulations, we have experienced that the melting is not initiated in the fillet but rather at a distance from the fillet, which causes molten material to overflow the solid fillet and cause the calculations to break down (due to the severe deformation of the elements in the mushy zone close the workpiece surface). This behaviour is not unphysical, however it does not appear in [91]. Considering the results obtained in section 5.4.1, we figure that it might be the lack of heat transfer in the welding direction that delays the melting of the fillet, and thus improperly causes the overflow. Hence this is a limitation of our model. It is remedied by specifying a strictly positive radius of the fillet so that the surface source alone is enough to melt the fillet first. The fillet radius is coupled to the mesh size h_ϵ at the fillet, so that the effect of the modified geometry vanishes with decreasing mesh size, see discussion below.

Our computational domain is an undeformed rectangle. So far we have for simplicity and brevity assumed that the initial and referential configurations are the same. This is no longer the case, but the exact same analysis is valid even though we must now define an appropriate transformation $\omega_0 : \Omega_0 \xrightarrow{\sim} \Omega^0$ that maps the computational rectangle onto the initial configuration of the workpiece. This can be done in several ways. The a priori idea is to minimize the deformation of the element domains. We have tried a different initial configurations, and have found that the following mapping is a good one;

$$\omega_0(X, Y) = [X, Y + X + \frac{h_0 + Y}{h_0} h_\epsilon (\exp(-X/h_\epsilon) - 1)]^T$$

where h_ϵ is a measure of the local element size at the fillet. We notice that the previously employed boundary condition $\frac{\partial \omega_2}{\partial X} = 0$ for the workpiece configuration at the symmetry line is more restrictive than necessary since the symmetry line is not a physical boundary of the workpiece. We require only that corners in the fluid surface are avoided, and thus it is necessary to ensure $\frac{\partial \omega_2}{\partial X} = 0$ along the fillet only, which in our case is represented by a point. This point condition is fulfilled by the above initial configuration.

It is a vital part of this study to compare the prediction of the shape of the interior and exterior weld that our simulation tool provide, to the computational results obtained using the different approach of [91]. Since the results obtained in the latter are verified against experimental results, this case study is also an indirect verification of former. However, the [91] model differs from our model not only in that it is steady state and predicts the surface shape by a minimization algorithm, it also applies a volumetric heat source of a certain depth and width, that models the heat transfer from the filler metal droplets which at high speed strike the pool. As in [85], the volumetric source is calculated from cavitation depth, droplet radii and frequency. However the experiments against which the simulations are verified were conducted in spray transfer mode, which implies that the frequency of the droplets is not so easily approximated. As a matter of fact, when simulating a GMA process operated at a high current such as the one at hand, we would very much like to avoid the need for considering individual droplets. We take therefore the opportunity to investigate the importance of where the heat is supplied, by employing in similar simulations also only an equivalent surface source efficiency.

Having run the case for the first time, we find that it doesn't work very well since the compressibility term overcompensates and material partly solidifies in the arc cavity as the source passes, see figure 7. This is unphysical, and further calculation becomes tedious. This phenomena was not visible in earlier test cases using this model, however under realistic conditions such as those at hand (that has now become feasible to consider since our project has gotten access to a more powerful workstation), the arc pressure and the mass deposition rate are higher, and cause more severe violations of the incompressibility condition. More specifically, the energy sinks applied in order to eliminate the effect of the violations of the incompressibility condition on the global energy conservation, are highly localized to the elements near the weld pool boundary. Thus we wish to get rid of the compressibility term, but without disturbing the global energy conservation. We turn therefore again to a method that was previously rejected; Adding material by specifying the motion of the weld pool boundary via the artificial force on the pseudofluid, anticipating that this method behaves better than the hitherto used method when applied to the present realistic simulation case. The surface force on the pseudo-fluid includes now a weak term for the deposited volume per second. Since the incorporation of the action of the filler is now done via the the action of the Lagrange multiplier, the kinematic

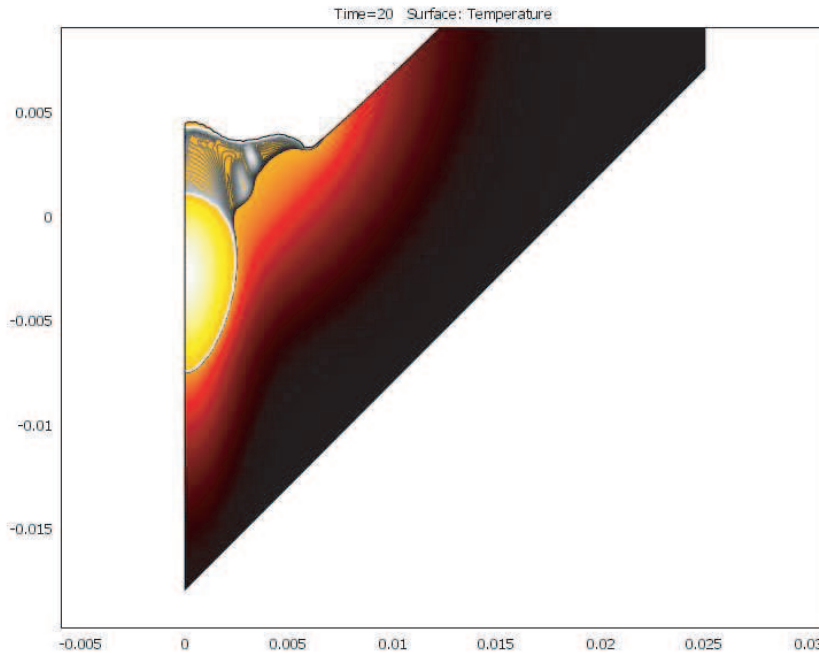


Figure 7: The pointwise compressibility sink makes the pool mushy as the source passes.

constraint is automatically relaxed so that the flow velocity at the pool surface, as affected by the arc pressure and Lorentz force, can be directed mainly towards the bottom of the pool even as the pool surface is under elevation. What more is, the problem with the violation of the incompressibility condition is perhaps no longer an issue. Hopefully we avoid the need for applying the compressibility term, however global energy conservation is now maintained using a surface sink which is coupled to the energy density at the surface, as explained by equation (8). Test runs show that this approach does not solve the problem, since the surface sink now overcompensates, and instead of having material solidify in the interior of the pool as the source passes, it now solidifies from the pool surface. Apparently, the rate of energy transfer by mass is much higher than the rate of energy transfer by the Joule heating as modelled by the boundary source in the energy equation.

In order to remedy the situation, we propose a new heat source model that is both volumetric and acting as a surface source. The volumetric part of the source is meant to keep the material from solidifying in the interior of the pool. The user specifies the arc efficiencies for each source term, and their sum cannot be greater than 1. The drawback is one we have encountered many times before when dealing with mesh motion techniques, and it is that we cannot control the

amount of energy transferred to the deforming workpiece without modifying the shape of the source. By expressing volumetric sources and sinks in material coordinates we would gain control of the size of integrals that determine the total energy of the source, but it also has the effect of attaching physical meaning to the mesh motion, which is something that we wish to avoid. However, if the fraction of the total arc efficiency that is used for modelling interior energy deposition is not great (it is 31 percent of the source power in this case study), the error in total energy input can be neglected. We let the volumetric source be of Gaussian shape, and thus three numbers are used to specify its decay in the three spatial directions. Since the volumetric source is meant to model heat transfer from metal droplets, it is natural that its dispersion in the plane orthogonal to the arc axis is the same as for the mass source. Thus it remains to specify its depth d . This can be calculated in a fashion similar to the one employed in [91], however it is not apparent what value is used in that study. We set $d = 0.008$, and leave this parameter for future calibration. As the fillet case was run with the new source, we found that the problem with the solid (mushy) chunks of metal in pool, had not been solved. However, before the calculations stalled, we saw that the interior pool had begun to take on the finger penetration shape, as in [91]. It seems thus that the volumetric source term should be kept in order to better recreate and predict the geometry of GMA weld pools.

Having failed at solving the main problem by modifying the source, we now instead aim at its heart. We wish to spread out the effect of the highly localized compressibility variations on a larger part of the workpiece. Thus we try the following; We calculate the total artificial effect input, and add an artificial energy sink in the interior of the computational domain, shaped not much unlike the volumetric source. There is now a coupling of the weight on the artificial sink to the integral of the energy density and velocity derivatives over the entire domain. We must hypothesize the distribution of the sink. At first attempt, we try the same length of the semi-axes as for the source. Test runs show that no artificial solidification occurs, and the computational method conserves the energy globally. We also see that the artificial sink destroys the finger penetration shape of the weld pool directly below the arc, however we have had good agreement with the results of [91] considering the pool profile in the rear of the pool (c.f. figure 8). One should note however, that the results presented in [91] are verified against fusion zone shapes only, and therefore we cannot determine what pool shape is correct. Since the incorporation of a volumetric sink into the model involves introducing yet another unknown parameter, i.e. the sink shape, we decide not to continue working along these lines.

Yet another disturbing phenomena is that kinks in the surface configuration appear in the solid phase close to the mushy zone, see figure 9. For one particular mesh, we have seen that these are due to an unphysical mesh motion that violates the kinematic constraint. Since the kinks always appear close to the fusion boundary, it seems that they are related to the physics of the problem. If the kinematic boundary condition is not fulfilled, the only connection the mesh motion has to the physics of the problem is via the shape of the domain on

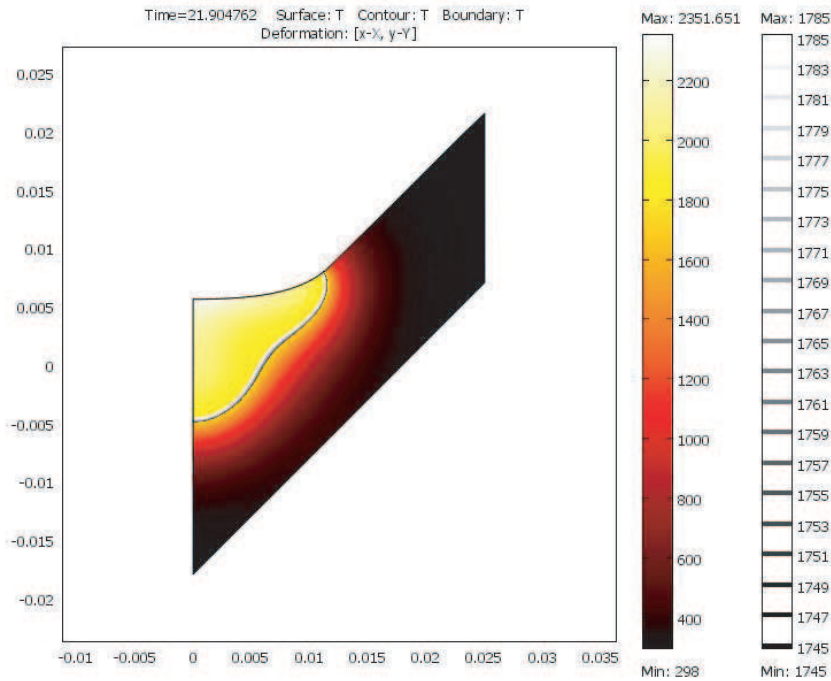


Figure 8: Pool profile 8mm behind the arc.

which the governing Laplace equation is solved. It seems thus that the problem is inherent in the Laplace equation, and the behaviour of its solution near a concavity in the domain such as the one that appears at the triple point. One of the reasons for choosing the Laplace equation for determining the mesh velocity was that its solutions are usually well-behaved on two dimensional convex domains, but as filler material due to the action of the arc pressure is pushed towards the fusion boundary, it elevates over the weld plane, and the pool surface strives to attach to the solid plate at an angle, thus creating an inwards corner in the domain. It can be suggested that this build-up of material towards the fusion boundary is more severe when considered as a phenomena occurring in the plane perpendicular to the weld line only, since we have then removed the possibility of having mass escape from the cavity by building up in the welding direction (the direction in which overlaps do not compromise the weld quality). This suggestion is supported by the fact that in our simulations we find that more mass per length is contained in the transversal slice directly below the arc than is contained in the corresponding slice simulated using the three dimensional model to which we compare our results. Furthermore we have, to a minor extent, verified that the kinking behaviour is actually a consequence of the irregularity in domain boundary, by solving the Laplace equation on the rectangular material domain instead. This approach though, seems to cause

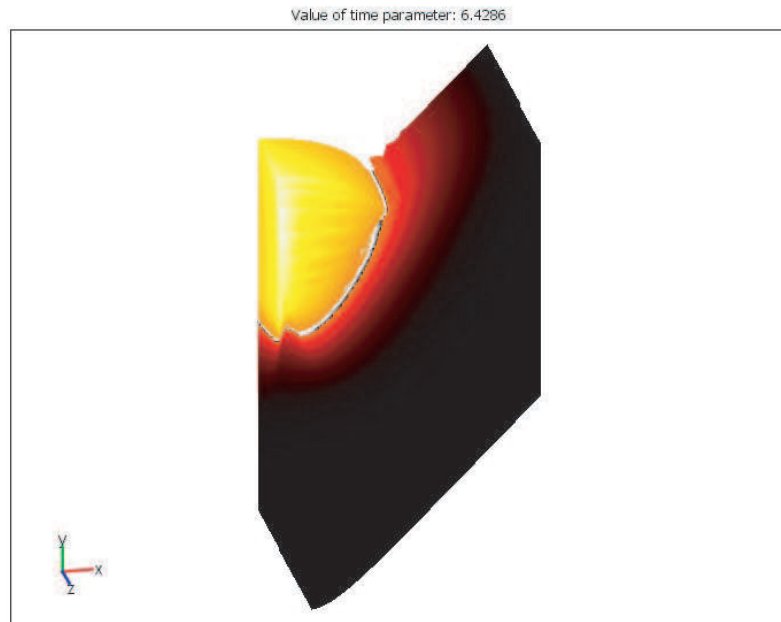


Figure 9: Kinks in the solid workpiece surface are visible near the mushy zone. The section of the workpiece visualized in this figure has its weld plane to the left, partially facing the viewer.

unfavourable deformations of the element domains not only at the triple point, since the calculation was slow and finally came to a stall. However, the kinking behaviour had reduced in severity, but had not entirely vanished, which is probably due to the remaining unregularity in the kinematic boundary condition. The unregularity in the kinematic boundary condition appears since the multiplier technique abruptly switches from restricting the horizontal mesh velocity to restricting the vertical mesh velocity at the triple point. This is also the reason why it is difficult to implement the kinematic condition as a Dirichlet condition; The degrees of freedom to remove from the approximation space changes dynamically between different solution variables and boundary segments. What more is, the constraint is a coupling between the different solution variables, which is a further complication. We will later explore a method that avoids these difficulties; By transforming the dependent coordinates of the mesh velocity, so that one single component determines the normal velocity at the boundary, the kinematic constraint can be implemented as a homogenous Dirichlet condition on a single scalar unknown function representing the difference in the normal flow of the pseudo-fluid and the physical fluid. First we make a few other remarks concerning the mesh motion equation.

When defining the equation for the workpiece motion, we did not take into account the effect of the mesh viscosity, which happens to be discontinuous. When specifying instead a constant mesh viscosity, the simulation based on the model in which mass is added in the incompressibility equation finishes quickly, and the kinks have decreased in size. However when trying to add mass in the modified way, the simulation does not converge in the same amount of time. This is an argument for sticking to the model we have hitherto developed. For one particular test problem in which kinking has previously appeared when using a mesh viscosity identically equal to 1, we have also run a number of simulations in which the mesh viscosity was set to orders of magnitudes larger and smaller, but none of these latter simulations were any more successful than the former.

Even though removing the mesh-dependence from the mesh viscosity decreased computational times, the issue with the surface kinks is not yet completely solved. In simulation cases closely related to the present, we have experienced that the problem still appears, but now the kinematic constraint is not as severely violated. Further investigation reveals an inaccuracy in the solution of the ordinary differential equation that extracts the current configuration from the mesh velocity. This contributes to the error in the workpiece motion, but is not easily circumvented. The best we can do is to further refine the mesh. Since the kinks appear on the scale of the element domains, their severity will decrease with decreasing mesh size.

We recall now a problem that appeared early in the process of implementing our model; The low level implementation of the coordinate derivatives are not suitable for use on the domain boundaries. As we switch to expressions for tangential derivatives, the simulation tool works much better. We continue now to replace the expressions for the surface tension forces with new ones utilizing only tangential derivatives. After having done so, convergence is faster and better, but still kinks appear.

It seems to be the mesh velocity in the surface adjacent element the domain of which is part solid and part fluid (and thus contains a lot of mush) that causes the kink. Its fluid part strives to flatten out, and this causes its solid part to follow this motion, thus creating a kink at its solid boundary, see figure 10. Since there is a small but not negligible physical deformation of the solid, i.e. a non-vanishing fluid flow gradient, we perform a minor investigation of the sensitivity of the simulation with respect to the parameter that determines the viscosity of the solid state workpiece. Having done so we find a much better value (10^5), for which the calculations are much faster, i.e. the DASP algorithm converges in fewer iterations. This value is lower than the previously used, and a higher value did not reduce the kinks. Modifying the arc pressure so that it acts only on the fluid surface and not on the solid workpiece surface on which it should exercise no influence but apparently does, reveals yet another speed-up. In spite of these favourable efforts, the kinks remain.

It remains to investigate the effects of the equation for the mesh motion. So far we have used an equation that we claimed mimicked the one for an inertia-less fluid, however the pure Laplace equation we solve is not quite the same as the one for a Stokes flow, in which the stress tensor contains the transpose of the

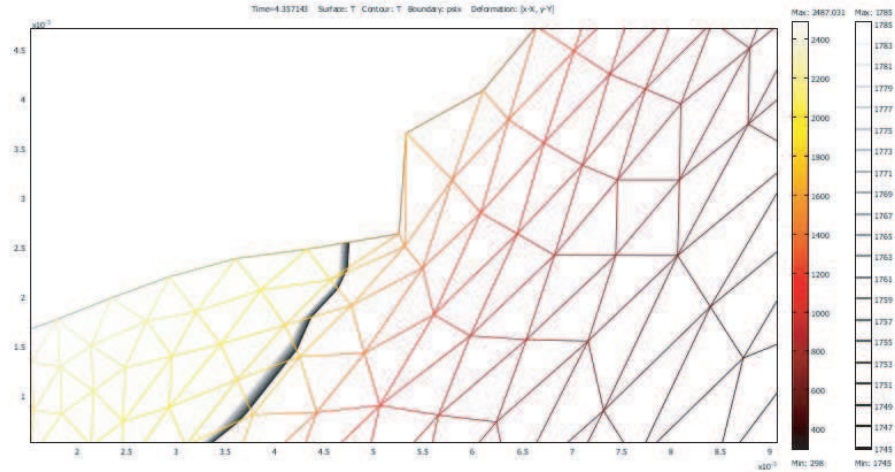


Figure 10: Kinking element extending across the mushy zone. The gray line is the mushy zone, molten material is to the left. In this picture, a linearized version of the piecewise quadratic deformation is plotted.

velocity gradients. There is also the possibility of adding inertia to the mesh. We have tried different combinations of these ideas, but it is not obvious from the test cases we have run which choice is the best. In some cases a pseudofluid with inertia improves mass conservation, and in some cases the modified stress tensor gives rise to very distorted meshes, and vice versa.

Since nothing else seems to do the trick, we now use brute force. A so called porosity term was added as a boundary source for the mesh velocity, and this term counteracts any mesh motion normal to a solid surface, thus inhibiting unphysical workpiece deformations. This is a restriction of our model, since solid surfaces were previously allowed to move (a solidified overflow wavefront for example), but not deform. Now we force all solid surfaces to remain at rest. Hopefully, cases in which solid parts of the workpiece are separated from the solid that is adjacent to a Dirichlet boundary for the fluid flow and workpiece motion, are not in abundance. The behaviour of the solution is dependent upon the value of the factor multiplying the porosity term, however we have not found value that inhibits the kinking behaviour.

All in all, the kinking behaviour is due to an unphysical mesh motion that appears due to the fact that our computational model does not take into ac-

count the appropriate physical phenomena. A boundary adjacent element in the mushy zone experience a force from the surface tension, but its solid part resists any velocity gradients. It seems that as an increasingly large part of the element is melted, the high viscosity in its solid part cannot resist the surface tension force, and the element deforms, thus forcing the adjacent element in the solid phase to follow this motion in order to achieve continuity of the material configuration, even though no fluid flow occurs in that element. A configuration with a concavity of small radius results, and the solution of the mesh moving equation oscillates along the surface. Actually the kinking behaviour these oscillations provoke appears also in the liquid part of the workpiece, but there the surface tension force quickly smooths them out, and all we see are small and rapidly diminishing surface waves travelling towards the joint plane. It is important to note that the severity of the kinking behaviour is dependent upon the mesh size, and smaller elements will decrease the size of the kinks, but not necessarily their impact on the computational performance. We have also experienced that a larger surface tension gradient has a smoothing effect on the surface configuration, i.e. Marangoni forces decrease the severity of the kinks. This effect was not obvious to us when studying only the undiscretized equations.

Having tried modifying the equations modelling the physics of the problem, it remains now to investigate the computational model and its effect on the simulation. The choice of elements is discussed in section 6.7. We now try adapting the mesh so that mesh elements are clustered in the region where strong gradients in the coefficients appear, i.e. in the mushy zone. The time derivative of the Jacobian determinant of the configuration is a measure of the increase in the local mesh density. If we base our mesh moving strategy upon a specification of the Jacobian and its derivative in time, we would thus be able to monitor the motion of the element domains more closely than we have so far, and so obtain an adaptive method. A mesh velocity distribution that renders a regular mesh automatically satisfies the geometrical conservation law, and this law can be used as the starting point for the development of an adaptive mesh moving method. If we add the reasonable condition that the mesh velocity field is irrotational, we can use a potential formulation for the flow of the pseudofluid, and thus reduce the number of dependent variables. What more is, the kinematic constraint enters the equation for the flow potential in the form of a natural boundary condition, and it is worth investigating if an implementation based on this new method can more accurately handle the phenomena that provoke the kinking behaviour of the mesh surface. The methods we have tried are inspired by those explained in [6]. However, our pseudofluid is not incompressible, and also undergoing a net expansion. Therefore the compatibility condition for the divergence of the mesh velocity field is somewhat more complicated, and it turns out that a potential formulation based on the GCL is difficult to implement in an efficient way.

The only success we have had so far in our attempts to add adaptivity to the computational model is when remaining with the hitherto approach in which we solve a Laplace equation for the mesh velocity, but modifying it only

by adding a body force on the pseudofluid which acts in the direction of the mushy zone. This direction is approximated by the temperature gradient and its negative in the solid and liquid parts of the workpiece respectively. Elements are thus pushed into the mushy zone where the strong gradients of the material properties occur. In the ideal case this would cluster the elements to the extent that the mushy zone extends over several elements, thus reducing the effect of the kinking element. It has proven difficult to adequately chose the size of the body force though, and the adaptivity works well only during a limited time interval.

In the process of developing an adaptive method, we have experienced that for small deformations allowing a method of spines formulation, the simulation time can be shortened if we solve the Laplace equation for the mesh velocity component in the arc axis direction only. This is not quite the method of spines explained in section 6.2, since we solve an equation, in the entire domain, for the mesh velocity in the y -direction. This method takes into account the mesh velocity gradient in the x -direction, and is thus more efficient than the method of spines, since it consequently does not in comparison skew the elements very much, although it cannot be used for severely deformed pools.

Based on the above experiences, we have managed to define a computational model that works better than the hitherto employed, at least for a limited class of problems. The method circumvents the problem with the violation of the kinematic boundary constraint by implementing it as pointwise homogenous Dirichlet constraint on the a solution variable representing the difference between the mesh velocity and the fluid flow velocity. For this to work, the constraint must be on only one of the solution variables along the entire Dirichlet boundary, and not coupled to any other solution variable. Thus we transform the dependent variables of the “velocity difference” equation into a coordinate system the coordinate directions of which at the boundary coincide with the boundary tangential and normal directions. The constraint is now solely on the solution variable representing the velocity component which on the boundary coincides with the normal velocity difference. In order to insert the mesh velocity into the governing equations for the other quantities of interest, we must transform the velocity difference back into the global xy -coordinate system. What more is, we may choose to solve for the “normal” mesh velocity difference component only, and define the other component in such a fashion that the mesh moves in the vertical direction only. We have seen that solving the Laplace equation for a single velocity component only is efficient. Furthermore, we solve this equation on the undeformed domain, thus circumventing all problems with irregularities in the domain and boundary conditions. For this method to be efficient, one must take special care in the scaling of the solution variables representing the transformed velocity difference. For a special kind of scaling, the method of adding filler material to the pool by modifying the normal velocity of the boundary can easily be implented as an inhomogenous constraint on the “normal velocity difference” solution variable, that does not depend on any other solution variable, not even on the workpiece configuration, i.e. the Jacobian of the current configuration disappear from the constraint equation.

Since we specify the motion of the boundary, one could control the amount of energy added by mass transfer, if one could in the simulation also control the temperature at the pool surface.

We have also the option of solving only for the “normal velocity difference” and setting the “tangential” component to zero, thus not restricting the configuration of the workpiece boundary at all. We note also that if we are to exploit symmetry when using the modified model in this fashion, it is necessary that ω fulfills the boundary condition $\frac{\partial \omega_2}{\partial X} = 0$ along the entire symmetry line. Thus we employ the initial configuration

$$\omega_0(X, Y) = [X, Y + X + h_\epsilon(\exp(-X/h_\epsilon) - 1)]^T$$

when using the modified mesh moving method.

Further investigations of the modified model reveals that the Dirichlet condition seems to be too restrictive for the calculations to converge at a satisfying rate, and we have found that relaxing the kinematic constraint using a penalty method alleviates any remaining problem concerning the boundary condition for the mesh velocity. We can now solve for the mesh velocity instead of the velocity difference, which makes the equations more easy to implement, and apparently renders a more robust computational model.

As a paranthesis, we mention also that we tried to solving the Laplace equation for the transformed mesh velocity on the undeformed domain, which makes it easy to increase the resistance of the pseudofluid against shear along a plane perpendicular to the weld surface. This would theoretically imply an increased resistance towards kinking, but we have had no success when working along these lines.

After extensive testing of the different models that we now have at hand, two have emerged as the most competitive ones. One of them is approximately the same as we have explained so far in this treatise, however we solve the Laplace equation for the mesh motion in the vertical direction only, thus restricting the set of possible configurations. As previously mentioned, we have experienced that the problems with the kinematic boundary condition can be resolved simply by relaxing it using a penalization method instead of a multiplier method or linear system reduction method. The other model that has emerged as competitive is the one developed during this case study, and in which the dependent variables in the mesh velocity equation are transformed such that the kinematic boundary condition, which is implemented using a penalization method, is on one solution variable only. Also in this model we solve the Laplace equation for the one mesh velocity component only, however now the mesh always has freedom to move in the direction normal to the surface. Consequently this approach does not restrict the set of possible configurations. This is of course an advantage, but unless large deformations are expected, the former model is usually more computationally efficient (that is, it finishes in shorter time), since the distortion of the mesh is usually not as severe as when employing the latter model. Finally, we have experienced that for both these models, a very good technique for adding mass to the pool is to control the mesh velocity normal to

the pool surface. This is good news since we now explicitly control where mass is added to the pool, and consequently there is a possibility of also controlling for example the temperature at the locations where mass is added, and thus also controlling the energy input by mass transfer. Since we explicitly force the motion of the boundaries of the spatial domain during the filler metal deposition, the global mass conservation properties of the models are excellent. Both of these models are written down in their entirety in the following section.

Now we turn to a more detailed analysis of the simulation results for the fillet case study. A visualization of the pool can be found in figure 11. The results

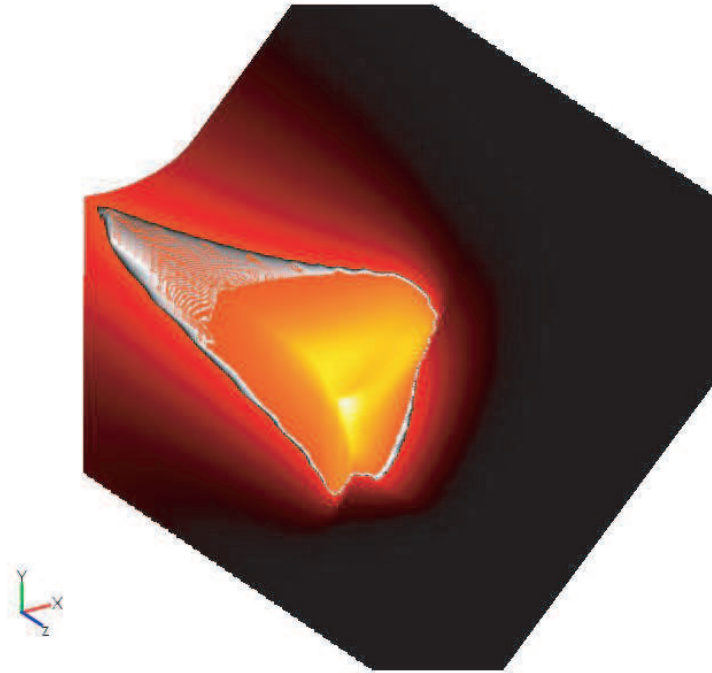


Figure 11: The fillet weld pool.

we discuss here were obtained from the model (23) below, but with penalization for the kinematic constraint instead of the multiplier technique. We have used the value $\eta_s = 0.54$ for the efficiency of the surface source, but have avoided modelling the droplet heat transfer as an applied volumetric heat source, by setting $\eta_v = 0$. The discretization resulted in a system with 99158 degrees of freedom. The solidified weld bead profiles agree reasonably well with the one computed in [91]. The bead profile is mainly determined by the maximum weld pool width and the volume of the deposited mass. Our simulations produce a slightly wider pool, and therefore also a wider bead the height of which is slightly lower. We also notice that our bead is not entirely flat as in [91], but has a top along its center line. This can be seen from figure 12, which also

displays the spatial configuration of the mesh. We have seen this shape before in other preliminary simulation tests that are not documented here, and we have hypothesized that it is mainly due to the effect of Marangoni forces. This study supports this hypothesis since it can be assumed that the main force driving the flow in the pool far away from the source is exactly the Marangoni force.

A fingering effect is obtained as the source passes and adds energy by mass transfer and the Lorenz force produces a downwards motion of the hot material close to the arc center. At this point there is a second recirculating motion further away from the pool center (see figure 13), which is driven by the Marangoni force due to the negative value of the surface tension derivative with respect to temperature. At a further distance from the source, the downwards circulating flow reduces in strength and the pool penetration is not increased, but the pool width increases still due to the action of the Marangoni force. The pool penetration directly below the arc is not as deep as for the pool calculated in [91]. However, the penetration of the actual solidified weld was measured and found to be 3.4mm, which agrees fairly well with the penetration depth of 3.1mm that our models calculate.

We have showed that the fingering effect can be obtained by adding mass and energy at the surface of the pool, instead of applying a combination of a surface source and a volumetric heat source in the interior of the pool. The fact that the pool shape does not entirely match the one computed in [91] does not mean that we have computed a shape that is not in accordance with reality. By studying the shape of the fusion zone of the actual weld and the fusion zone predicted by our simulations, we find that they agree reasonably well.

We also ran the test case using the method of adding filler material in which we modify the mesh motion. We compared the maximum depth and width of the pool obtained using this method, and they matched quite well the ones obtained using the method the results of which is analyzed above. This is not entirely surprising, since it can be suspected from equations (7) and (8) that the latter tends to the former as the mesh size tends to zero. It may be interesting thus to compare the cpu times for the different models. So far we have only seen that the wall-time for the simulation based upon the mass source model is shorter than for the simulation based upon the mesh velocity source model.

6.7 A moving mesh mixed finite element method of lines

We now summarize the choices we have made for the weighting spaces for the unknown functions the approximations of which we would like to compute. By choosing these spaces to be of finite dimensions, we effectively discretize the equations with respect to the spatial variables. Since the time variable remains continuous, this discretization results in a differential-algebraic system of equations, in which the constraints are represented by the purely algebraic ones. The reason why we apply the method of lines instead of applying finite elements to all three independent variables at once, as in the corresponding three dimensional steady-state formulation, is that it is generally easier to obtain convergence when applying our choice of software to time-dependent problems than

to static ones (c.f. section 6.5).

It can be seen that the boundary mass source which has been applied in many of our simulations, is not a bounded functional on the weighting space for the pressure, so the well-posedness of the weak formulation does not follow from standard methods. This fact does not hinder the method from working remarkably well. For the sake of completeness, we have also simulated test cases using a volumetric mass source term instead of the boundary source term. This produced a solution quite different from the one obtained using the boundary source for the same problem, most probably due to the fact that the kinematic boundary condition was severely violated in the case with the volumetric source. The added mass was consequently overestimated.

We employ the triangular Taylor-Hood element pair ([25]) for the fluid flow equations, with linear shape functions for the pressure. It is not directly obvious that this element combination is stable for the Navier-Stokes equations on a moving domain, but it has hitherto worked quite well. Since the mesh velocity is coupled to the fluid flow via the kinematic constraint, it is natural, and also very efficient, to let the unknowns representing the mesh velocity components also be approximated using second order Lagrange elements on the same mesh. Also the current configuration is discretized using this element type, since it is extracted from the mesh velocity using an ordinary differential equation in time. Finally, second order Lagrange elements are used for the temperature, and linear Lagrange elements have been used for the multiplier if computed.

Since it seems natural that the shape of the free surface should have at least first order geometrical continuity, one may suspect that for example Argyris elements would be more suitable for approximating the motion. Actually, even using triangular Hermite elements would result in a C^1 surface, since it is enough that we have continuity of the derivatives at the element nodes located at the surface. However, we have found that both the Argyris and Hermite elements perform worse than the Lagrange element. We have experienced that the coupling between the fluid flow velocities and the mesh velocities via the kinematic constraint fails when using unsuitable element combinations for the multiplier and velocities, because the calculations using other elements than Lagrange fails to converge at the same time as the partial melting of the base material is initiated and the weld surface begins to change shape.

Since the integrands in the FE formulation involve products of both velocity or temperature with Jacobians which are also second order, it is necessary to employ a high order quadrature formula in order to exactly evaluate the integrals. We have however experienced that underintegration is much faster and seemingly the errors inherent in the low order quadrature formulas we use are not in any way devastating.

On the following pages we present the system of equations, with boundary and initial conditions, for the simulation case studied in section 6.6. They are labeled (23) and (24). The equations for the material representation of the x -direction and y -direction fluid velocity components \hat{u} and \hat{v} , for the material representation of the pressure \hat{p} , and for the material representation of the temperature \hat{T} , are almost the same for the two systems, however in order

to achieve a reasonable balance between brevity and completeness, we present the system (23) with the kinematic constraint implemented using a Lagrange multiplier and a boundary mass source in the continuity equation, and the system (24) implemented using a penalization term and a modification of the weld surface motion for the filler metal deposition. The former is solved for the material representation of the y -component of the mesh velocity $\dot{\omega}_2$, while the latter is solved for the material representation of the transformed velocity component ψ_n . Neither system incorporates an artificial sink. Test functions are as before denoted by an overbar, and for reasons of brevity we have removed the subscripts on the nabla operator. For the same reason, we do not write out the Dirichlet boundary conditions on the fluid flow and mesh velocity, but they are more or less apparent from the context. The implementation of the surface divergence operator is somewhat intricate, and we are here content with the notation $\hat{\nabla}_S$. The computational domain is a rectangle aligned with the coordinate axes which extends h_0 meters in the y -direction and 0.025 meters in the x -direction.

$$0 = \tag{23}$$

$$- \int_{\Omega_0} \left[\nabla \begin{bmatrix} 0 \\ \hat{\omega}_2 \end{bmatrix} \mathcal{J}_\omega^{-1} \right] : \left[\nabla \begin{bmatrix} 0 \\ \hat{\omega}_2 \end{bmatrix} \mathcal{J}_\omega^{-1} \right] |_{\mathcal{J}_\omega}$$

(Laplace equation for the flow of the pseudo-fluid)

$$- \int_{\partial\Omega_0} \hat{\lambda} \begin{bmatrix} 0 \\ \hat{\omega}_2 \end{bmatrix} \cdot \hat{\mathbf{n}}$$

(Constraining force on pseudo-fluid surface)

$$0 =$$

$$\int_{\partial\Omega_0} \left(\begin{bmatrix} \hat{u} \\ \hat{v} \end{bmatrix} - \begin{bmatrix} 0 \\ \hat{\omega}_2 \end{bmatrix} \right) \cdot \hat{\mathbf{n}} \hat{\lambda}$$

(Constraint equation for multiplier)

$$\int_{\Omega_0} \frac{\partial}{\partial t} \begin{bmatrix} 0 \\ \omega_2 \end{bmatrix} \cdot \begin{bmatrix} 0 \\ \bar{\omega}_2 \end{bmatrix} =$$

$$\int_{\Omega_0} \begin{bmatrix} 0 \\ \hat{\omega}_2 \end{bmatrix} \cdot \begin{bmatrix} 0 \\ \bar{\omega}_2 \end{bmatrix}$$

(ODE in time for mesh motion)

$$\rho_{ref} \int_{\Omega_0} \left[\frac{\partial}{\partial t} \begin{bmatrix} \hat{u} \\ \hat{v} \end{bmatrix} + \nabla \begin{bmatrix} \hat{u} \\ \hat{v} \end{bmatrix} \mathcal{J}_\omega^{-1} \left(\begin{bmatrix} \hat{u} \\ \hat{v} \end{bmatrix} - \begin{bmatrix} 0 \\ \hat{\omega}_2 \end{bmatrix} \right) \right] \cdot \begin{bmatrix} \hat{u} \\ \hat{v} \end{bmatrix} |_{\mathcal{J}_\omega} =$$

(Inertia and convection of linear momentum)

$$- \int_{\Omega_0} 10^5 \left[\frac{\mu_m}{10^5} \right]^{f \circ \hat{T}} \left[\nabla \begin{bmatrix} \hat{u} \\ \hat{v} \end{bmatrix} \mathcal{J}_\omega^{-1} + \mathcal{J}_\omega^{-T} (\nabla \begin{bmatrix} \hat{u} \\ \hat{v} \end{bmatrix})^T \right] : \left[\nabla \begin{bmatrix} \hat{u} \\ \hat{v} \end{bmatrix} \mathcal{J}_\omega^{-1} \right] |_{\mathcal{J}_\omega}$$

(Internal force in fluid)

$$+ \int_{\Omega_0} \mathbf{I} \hat{p} : \left[\nabla \begin{bmatrix} \hat{u} \\ \hat{v} \end{bmatrix} \mathcal{J}_\omega^{-1} \right] |_{\mathcal{J}_\omega}$$

(Constraining force for incompressibility condition)

$$+ \rho_{ref} \int_{\Omega_0} \left[1 - f \circ \hat{T} \beta (\hat{T} - T_{sm}) \right] \begin{bmatrix} g_1 \\ g_2 \end{bmatrix} \cdot \begin{bmatrix} \hat{u} \\ \hat{v} \end{bmatrix} |_{\mathcal{J}_\omega}$$

(Gravitational force and buoyancy)

(23) cont'd.

$$-\int_{\Omega_0} \frac{\mu_B I}{2\pi r^2} \left(1 - \exp\left(-\frac{r^2}{\sigma^2}\right)\right) \left(1 + \frac{Y}{h_0}\right) \left[\frac{I}{\pi\sigma^2} \exp\left(-\frac{r^2}{\sigma(t)^2}\right) \left(1 + \frac{Y}{h_0}\right) X \right] \cdot \begin{bmatrix} \hat{u} \\ \hat{v} \end{bmatrix} \Big|_{\mathcal{J}_\omega} \\ \text{(Lorentz force)}$$

$$-\int_{\partial\Omega_0} \left(\gamma_m - A(\hat{T} - T_m)\right) \hat{\nabla}_S \cdot \begin{bmatrix} \hat{u} \\ \hat{v} \end{bmatrix} \\ \text{(Surface tension force)}$$

$$+\int_{\partial\Omega_0} \hat{\nabla}_S \left(\gamma_m - A(\hat{T} - T_m)\right) \cdot \begin{bmatrix} \hat{u} \\ \hat{v} \end{bmatrix} \\ \text{(Marangoni force)}$$

$$-\frac{P_{arc}}{\pi p_{arc}^2} \int_{\Gamma_0^w} f \circ \hat{T} \exp\left(\frac{-\|X, P_3(t)\|^2}{p_{arc}^2}\right) \hat{\mathbf{n}} \cdot \begin{bmatrix} \hat{u} \\ \hat{v} \end{bmatrix} \\ \text{(Arc pressure force)}$$

0 =

$$-\rho_{ref} \int_{\Omega_0} \nabla \begin{bmatrix} \hat{u} \\ \hat{v} \end{bmatrix} : \mathcal{J}_\omega^{-T} \hat{p} \Big|_{\mathcal{J}_\omega} \\ \text{(Constraint equation for pressure)}$$

$$-\epsilon \int_{\Omega_0} \nabla \hat{p} \mathcal{J}_\omega^{-1} \mathcal{J}_\omega^{-T} \nabla^T \hat{p} \Big|_{\mathcal{J}_\omega} - \epsilon^2 \int_{\Omega_0} \hat{p} \hat{p} \Big|_{\mathcal{J}_\omega} \\ \text{(Relaxation of incompressibility constraint)}$$

$$+\frac{M}{\pi b^2} \int_{\Gamma_0^w} f \circ \hat{T} \exp\left(\frac{-\|X, P_3(t)\|^2}{b^2}\right) \hat{p} \\ \text{(Mass deposition as a boundary source for the density)}$$

$$\rho_{ref} \int_{\Omega_0} \left(c \circ \hat{T} + L \frac{\partial f}{\partial \hat{T}} \circ \hat{T}\right) \left[\frac{\partial \hat{T}}{\partial t} + \nabla \hat{T} \mathcal{J}_\omega^{-1} \left(\begin{bmatrix} \hat{u} \\ \hat{v} \end{bmatrix} - \begin{bmatrix} 0 \\ \hat{\omega}_2 \end{bmatrix} \right) \right] \hat{T} \Big|_{\mathcal{J}_\omega} = \\ \text{(Total derivative of energy density)}$$

$$-\int_{\Omega_0} k \circ \hat{T} \nabla \hat{T} \mathcal{J}_\omega^{-1} \mathcal{J}_\omega^{-T} \nabla^T \hat{T} \Big|_{\mathcal{J}_\omega} \\ \text{(Thermal diffusion)}$$

(23) cont'd.

$$- \int_{\partial\Omega_0} \hat{k}_\infty (\hat{T} - \hat{T}_\infty) \|\mathcal{J}_\omega \hat{\mathbf{t}}\| \hat{T}$$

(Convective heat transfer across workpiece surfaces)

$$- \int_{\partial\Omega_0} \sigma \hat{\epsilon} (\hat{T}^4 - \hat{T}_\infty^4) \|\mathcal{J}_\omega \hat{\mathbf{t}}\| \hat{T}$$

(Radiative heat transfer across workpiece surfaces)

$$\frac{\eta_v 2\mathcal{W}}{\pi^{3/2} db^2} \int_{\Gamma_0^w} \exp\left(-\left\|\left(\frac{X}{b}, \frac{\omega_2}{d}, \frac{P_3(t)}{b}\right)\right\|^2\right) \hat{T}$$

(Applied volumetric heat source)

$$\frac{\eta_s \mathcal{W}}{\pi a^2} \int_{\Gamma_0^w} \exp\left(\frac{-\|(X, P_3(t))\|^2}{a^2}\right) \hat{T}$$

(Applied surface heat source)

 $\omega(X, Y; \mathbf{0}) =$

$$\left[X, Y + X + \frac{h_0 + Y}{h_0} h_\epsilon (\exp(-X/h_\epsilon) - 1)\right]^T$$

(Initial configuration)

$$\begin{bmatrix} 0 \\ \hat{\omega}_2 \end{bmatrix} = \begin{bmatrix} 0 \\ 0 \end{bmatrix}$$

(Initial mesh velocity)

$$\begin{bmatrix} \hat{u} \\ \hat{v} \end{bmatrix} = \begin{bmatrix} 0 \\ 0 \end{bmatrix}$$

(Initial flow velocity)

$$\hat{p} = 0$$

(Initial pressure)

$$\hat{T} = 298$$

(Initial temperature)

$$\hat{\lambda} = 0$$

(Initial multiplier)

$$0 = \tag{24}$$

$$\int_{\Omega_0} \nabla \begin{bmatrix} 0 \\ \hat{\omega}_2 \end{bmatrix} : \nabla \begin{bmatrix} 0 \\ \hat{\psi}_n \end{bmatrix}$$

(Laplace equation for the flow of the pseudo-fluid)

$$\int_{\partial\Omega_0} 10^5 \left(\begin{bmatrix} -\frac{\partial\omega_2}{X} \\ \frac{\partial\omega_1}{X} \end{bmatrix} \cdot \begin{bmatrix} \hat{u} \\ \hat{v} \end{bmatrix} + \frac{f\circ\hat{T}M}{\rho\pi b^2} \exp\left(\frac{-\|X, P_3(t)\|^2}{b^2}\right) - \hat{\psi}_n \right)$$

(Penalization term on pseudo-fluid surface)

$$\int_{\Omega_0} \frac{\partial}{\partial t} \begin{bmatrix} \omega_1 \\ \omega_2 \end{bmatrix} \cdot \begin{bmatrix} \bar{\omega}_1 \\ \bar{\omega}_2 \end{bmatrix} =$$

$$\int_{\Omega_0} \begin{bmatrix} \hat{\omega}_1 \\ \hat{\omega}_2 \end{bmatrix} \cdot \begin{bmatrix} \bar{\omega}_1 \\ \bar{\omega}_2 \end{bmatrix}$$

(ODE in time for mesh motion)

$$\rho_{ref} \int_{\Omega_0} \left[\frac{\partial}{\partial t} \begin{bmatrix} \hat{u} \\ \hat{v} \end{bmatrix} + \nabla \begin{bmatrix} \hat{u} \\ \hat{v} \end{bmatrix} \mathcal{J}_\omega^{-1} \left(\begin{bmatrix} \hat{u} \\ \hat{v} \end{bmatrix} - \begin{bmatrix} \hat{\omega}_1 \\ \hat{\omega}_2 \end{bmatrix} \right) \right] \cdot \begin{bmatrix} \hat{u} \\ \hat{v} \end{bmatrix} |_{\mathcal{J}_\omega} =$$

(Inertia and convection of linear momentum)

$$- \int_{\Omega_0} 10^5 \left[\frac{\mu_m}{10^5} \right]^{f\circ\hat{T}} \left[\nabla \begin{bmatrix} \hat{u} \\ \hat{v} \end{bmatrix} \mathcal{J}_\omega^{-1} + \mathcal{J}_\omega^{-T} (\nabla \begin{bmatrix} \hat{u} \\ \hat{v} \end{bmatrix})^T \right] : \left[\nabla \begin{bmatrix} \hat{u} \\ \hat{v} \end{bmatrix} \mathcal{J}_\omega^{-1} \right] |_{\mathcal{J}_\omega}$$

(Internal force in fluid)

$$+ \int_{\Omega_0} \mathbf{I}\hat{p} : \left[\nabla \begin{bmatrix} \hat{u} \\ \hat{v} \end{bmatrix} \mathcal{J}_\omega^{-1} \right] |_{\mathcal{J}_\omega}$$

(Constraining force for incompressibility condition)

$$+ \rho_{ref} \int_{\Omega_0} \left[1 - f\circ\hat{T}\beta(\hat{T} - T_{sm}) \right] \begin{bmatrix} g_1 \\ g_2 \end{bmatrix} \cdot \begin{bmatrix} \hat{u} \\ \hat{v} \end{bmatrix} |_{\mathcal{J}_\omega}$$

(Gravitational force and buoyancy)

$$- \int_{\Omega_0} \frac{\mu_B I}{2\pi r^2} \left(1 - \exp\left(-\frac{r^2}{\sigma^2}\right) \right) \left(1 + \frac{Y}{h_0} \right) \begin{bmatrix} \frac{I}{\pi\sigma^2} \exp\left(-\frac{r^2}{\sigma(t)^2}\right) \left(1 + \frac{Y}{h_0} \right) X \\ \frac{I}{2\pi h_0} \left(1 - \exp\left(-\frac{r^2}{\sigma(t)^2}\right) \right) \end{bmatrix} \cdot \begin{bmatrix} \hat{u} \\ \hat{v} \end{bmatrix} |_{\mathcal{J}_\omega}$$

(Lorentz force)

(24) cont'd.

$$- \int_{\partial\Omega_0} \left(\gamma_m - A(\hat{T} - T_m) \right) \hat{\nabla}_S \cdot \begin{bmatrix} \hat{u} \\ \hat{v} \end{bmatrix}$$

(Surface tension force)

$$+ \int_{\partial\Omega_0} \hat{\nabla}_S \left(\gamma_m - A(\hat{T} - T_m) \right) \cdot \begin{bmatrix} \hat{u} \\ \hat{v} \end{bmatrix}$$

(Marangoni force)

$$- \frac{P_{arc}}{\pi p_{arc}^2} \int_{\Gamma_0^w} f \circ \hat{T} \exp \left(\frac{-\|(X, P_3(t))\|^2}{p_{arc}^2} \right) \hat{\mathbf{n}} \cdot \begin{bmatrix} \hat{u} \\ \hat{v} \end{bmatrix}$$

(Arc pressure force)

0 =

$$- \rho_{ref} \int_{\Omega_0} \nabla \begin{bmatrix} \hat{u} \\ \hat{v} \end{bmatrix} : \mathcal{J}_\omega^{-T} \hat{p} | \mathcal{J}_\omega |$$

(Constraint equation for pressure)

$$- \epsilon \int_{\Omega_0} \nabla \hat{p} \mathcal{J}_\omega^{-1} \mathcal{J}_\omega^{-T} \nabla^T \hat{p} | \mathcal{J}_\omega | - \epsilon^2 \int_{\Omega_0} \hat{p} \hat{p} | \mathcal{J}_\omega |$$

(Relaxation of incompressibility constraint)

$$\rho_{ref} \int_{\Omega_0} \left(c \circ \hat{T} + L \frac{\partial f}{\partial \hat{T}} \circ \hat{T} \right) \left[\frac{\partial \hat{T}}{\partial t} + \nabla \hat{T} \mathcal{J}_\omega^{-1} \left(\begin{bmatrix} \hat{u} \\ \hat{v} \end{bmatrix} - \begin{bmatrix} \hat{\omega}_1 \\ \hat{\omega}_2 \end{bmatrix} \right) \right] \hat{T} | \mathcal{J}_\omega | =$$

(Total derivative of energy density)

$$- \int_{\Omega_0} k \circ \hat{T} \nabla \hat{T} \mathcal{J}_\omega^{-1} \mathcal{J}_\omega^{-T} \nabla^T \hat{T} | \mathcal{J}_\omega |$$

(Thermal diffusion)

$$- \int_{\partial\Omega_0} \hat{k}_\infty (\hat{T} - \hat{T}_\infty) | \mathcal{J}_\omega \hat{\mathbf{t}} | \hat{T}$$

(Convective heat transfer across workpiece surfaces)

(24) cont'd.

$$- \int_{\partial\Omega_0} \sigma \hat{\epsilon}(\hat{T}^4 - \hat{T}_\infty^4) \|\mathcal{J}_\omega \hat{\mathbf{t}}\| \hat{T}$$

(Radiative heat transfer across workpiece surfaces)

$$\frac{\eta_v 2\mathcal{W}}{\pi^{3/2} db^2} \int_{\Gamma_0^w} \exp\left(-\left\|\left(\frac{X}{b}, \frac{\omega_2}{d}, \frac{P_3(t)}{b}\right)\right\|^2\right) \hat{T}$$

(Applied volumetric heat source)

$$\frac{\eta_s \mathcal{W}}{\pi a^2} \int_{\Gamma_0^w} \exp\left(-\frac{\|(X, P_3(t))\|^2}{a^2}\right) \hat{T}$$

(Applied surface heat source)

$$\begin{bmatrix} \hat{\omega}_1 \\ \hat{\omega}_2 \end{bmatrix} = \left(\left(\frac{\partial\omega_1}{X}\right)^2 + \left(\frac{\partial\omega_2}{X}\right)^2 \right)^{-1} \begin{bmatrix} -\frac{\partial\omega_2}{X} \\ \frac{\partial\omega_1}{X} \end{bmatrix} \hat{\psi}_n$$

(Constitutive equation for the mesh velocity)

$$\omega(X, Y; 0) =$$

$$[X, Y + X + h_\epsilon(\exp(-X/h_\epsilon) - 1)]^T$$

(Initial configuration)

$$\hat{\psi}_n = 0$$

(Initial mesh velocity)

$$\begin{bmatrix} \hat{u} \\ \hat{v} \end{bmatrix} = \begin{bmatrix} 0 \\ 0 \end{bmatrix}$$

(Initial flow velocity)

$$\hat{p} = 0$$

(Initial pressure)

$$\hat{T} = 298$$

(Initial temperature)

6.8 Something on continuum surface formulations and level set methods

When employing the hitherto analyzed method which is based upon a time-dependent mapping of the computational domain, sometimes referred to as an *interface tracking method*, it is difficult to treat topology changes such the ones occurring during non-autogeneous fusion welding as a filler metal droplet merges the pool, or during overflow. By incorporating into the model a medium on the other side of the boundary, one can avoid the need for (but not the possibility of) mapping the referential domain onto the spatial domain, and one may also treat topology changes without requiring special means. The *level set method* accomplish this. Another approach is to employ the *volume of fluid method*, in which the interface is treated as a connected volume. Since the thickness of the actual surface is below the continuum mechanical scale, the approach of yet treating it as a volume has rendered the volume of fluid method being sometimes known as a *diffuse interface method*. In [77], a diffuse interface method coupled with an energy method was successfully applied to three-phase systems. Therefore, we investigate further the possibilities of applying the akin level set method. When doing so, the medium outside the weld pool may be 'void', but may also be used in order to model the physical behaviour of the continuum neighbouring the weld pool, in our case the arc. Since we are interested in studying overflowing weld pools and spatters merging with the base plate, we will now attempt to adopt the level set method to the computational modelling of pool and arc fluid flow and heat transfer phenomena. This investigation has not been the major focus of our work, but since we have discovered some inherent difficulties, and also various possibilities, of employing an *interface capturing method* such as the level set method, we present these results in order to prepare ground for future studies.

For every t , we let $\Omega(t)$ be equal to the fixed box Ω_0 which is the union of two disjoint, not necessarily connected, subsets $\Omega_l(t)$ and $\Omega_g(t)$ where the subscripts indicate whether the subset represents the liquid or gaseous (arc) part of the computational domain. We arbitrarily include the smooth interface $\Gamma_{lg}(t) = \partial\Omega_l(t) \cap \partial\Omega_g(t)$ into $\Omega_l(t)$; This implies that when the subscript g appears on a function evaluated at the interface, its value should be interpreted in a limiting sense. In our simulations we have also mushy and solid domains, but since these are modelled as liquids of varying viscosity, the current notation suffices. Having fixed the spatial domain, there is no longer a need for mapping, and we may take $\omega(\mathbf{x}, t) \equiv \mathbf{x}$. However, the computational domain now contains the surfaces $\Gamma_{lg}(t)$ across which we cannot assume the continuity of neither the material properties nor the quantity \mathcal{X}^t nor its flux \mathbf{q}_{tot}^t . Since we wish to avoid tracking the moving boundaries, we realize that we must smooth the material properties in order for the finite element method to work well on an equation posed on Ω_0 . What more is, it is necessary to employ a *continuum surface formulation* (CSF) which is explained below.

Since equation (2) is still valid a.e. in the spatial domain, the derivation of equation (6) is also valid, except that the application of the Greens formula

leading to the boundary integral must be performed on Ω_l and Ω_g separately, since the flux field is continuous only when restricted to either of these sets. A generic semi-weak equation on the fixed domain containing a discontinuity surface thus reads;

$$\begin{aligned} & \frac{d}{dt} \int_{\Omega_0} \mathcal{X}^t \phi + \int_{\Omega_0} \mathbf{u}^t \cdot \nabla \mathcal{X}^t \phi = \\ & - \int_{\Omega_0} \mathcal{X}^t \nabla \cdot \mathbf{u}^t + \int_{\Omega_0} \mathbf{q}^t \cdot \nabla \phi - \int_{\partial \Omega_0} \mathbf{q}^t \cdot \mathbf{n}^t \phi - \int_{\Gamma_{l_g}^t(t)} [\mathbf{q}_l^t - \mathbf{q}_g^t] \cdot \mathbf{n}_l^t \phi + \int_{\Omega_0} F^t \phi, \end{aligned} \quad (25)$$

where \mathbf{n}_l^t is the normal to $\Gamma_{l_g}^t(t)$ pointing away from the liquid domain. Natural boundary conditions are incorporated in the weighted surface integral $\Gamma^t[\phi] := - \int_{\Gamma_{l_g}^t(t)} [\mathbf{q}_l^t - \mathbf{q}_g^t] \cdot \mathbf{n}_l^t \phi$. Assuming that the integrands and weighting space possess the appropriate characteristics, Γ^t is a generalized function. What more is, the characteristics of this generalized function allows us to approximate it arbitrarily well by a smooth function. It follows that the support of a such function approximates the interface. Although this approximation procedure is a simple application of a basic mathematical method, the use of volume integrals instead of surface integrals have in certain applications been distinguished as a special formulation commonly known as the CSF, or the *continuum surface force formulation*. This is because it has mainly been applied to the surface forces appearing in the momentum equation.

The assumption of incompressibility requires a few remarks, or rather the continuity equation does, since it is not an equation that we solve on the above form. In the case of continuous velocity and mass density fields, the incompressibility constraint is a condition such that, if satisfied at every point, we would find, using the transport theorem, that the size of every volume advected with the flow remains constant. We may still not extract any information about the mass density field, unless we assume that also the mass of every such control volume remains constant. In this case it follows again from the transport theorem that the following equation must hold for ρ

$$\frac{D\rho}{Dt} = 0,$$

i.e. we have implicitly assumed the absence of mass density sources and that the mass density flux is purely advective. If ρ is initialized to be constant, the above continuity equation is satisfied by taking the mass density equal to the same constant at every point in space and time, and so we do not need to solve an equation for the density, but only make sure that the incompressibility constraint is satisfied. In the case when the control volume contains a surface across which the velocity is discontinuous, it is not obvious how to interpret the transport theorem. The interpretation that every control volume $W(t)$ advected with the flow is, at every time, identified with the same set of fluid particles, implies some constraints on the velocity field further than being solenoidal. One may refer to [71] for an illustration of the fact that the continuity of the flow velocity normal to the interface between the liquid and gaseous fluids is a

consequence of the mass conservation assumption. The location of the liquid-gaseous interface can thus implicitly be defined using the normal velocities of the fluid particles at the interface⁴, which by virtue are well-defined. We note that this is what makes $\Gamma_{lg}^t(t)$ 'impermeable', that is, no fluid flows through the discontinuity surface. The condition of continuous normal velocity, which we refer to as the 'kinematic condition', is automatically satisfied by the finite element approximation using a continuous finite element space for the velocity, so its enforcement need not be addressed any further. The kinematic condition being satisfied at the interface, and the incompressibility condition $0 = -\nabla \cdot \mathbf{u}^t$ being satisfied almost everywhere in Ω_0 , we find from the Leibniz rule employed in [71], that we solve the same equation for the mass density as we did in the absence of a discontinuity surface. However, in this case we would like to solve the convection equation using discontinuous initial data, which will not work well. As mentioned before, this is the reason we smooth the material properties, and in doing so we introduce the *level set function*.

The level set function Φ is such that

$$\Phi(\mathbf{x}, t) = \begin{cases} > 0, & \mathbf{x} \in \Omega_l(t) \setminus \Gamma_{lg}(t) \\ = 0, & \mathbf{x} \in \Gamma_{lg}(t) \\ < 0, & \mathbf{x} \in \Omega_g(t) \end{cases}$$

The initial condition for the continuity equation can now be written as

$$\rho(\mathbf{x}, 0) = \rho_0(\mathbf{x}) = \begin{cases} = \rho_l, & \Phi(\mathbf{x}, 0) \geq 0 \\ = \rho_g, & \Phi(\mathbf{x}, 0) < 0 \end{cases},$$

However in computations we would like to employ a smoothed version of ρ_0 . In order to smooth ρ_0 such that the transition between the liquid and gaseous values of ρ occurs in a set the points of which are close to the interface, the standard level set method requires Φ to be a smooth function giving the signed distance to interface, and then sets

$$\rho_0(\mathbf{x}) = \rho_\epsilon(\mathbf{x}) := \rho_g + (\rho_l - \rho_g)H_\epsilon \circ \Phi(\mathbf{x}, 0),$$

where H_ϵ is a smoothed Heaviside function such that

$$H_\epsilon(x) = \begin{cases} = 0, & x < -\epsilon \\ = 1, & x > \epsilon \end{cases},$$

It follows that if the level set function is such that

$$\frac{D\Phi}{Dt} = 0, \tag{26}$$

⁴In treatise, we do not further investigate the question why the motion of a surface is well-defined by its normal velocity alone, or in other words, why the same interface is obtained when tracking the fluid particles at the interface using either \mathbf{u}_l^t or \mathbf{u}_g^t .

then $\rho(\mathbf{x}, t) := \rho_g + (\rho_l - \rho_g)H_\epsilon \circ \Phi(\mathbf{x}, t)$ satisfies the continuity equation (26) and the initial condition $\rho(\mathbf{x}, 0) = \rho_\epsilon(\mathbf{x})$. The beauty of the level set method is that by evolving the level set function in time using the continuity equation, we find that $\Gamma_{lg}(t) = \{\mathbf{x} \in \Omega_0 \mid \Phi(\mathbf{x}, t) = 0\}$, and that the sign of Φ changes neither in $\Omega_l(t)$ nor in $\Omega_g(t)$. What more is, the vector field $\Omega_0 \ni \mathbf{x} \rightarrow \mathbf{n}^t(\mathbf{x}) = -\frac{\nabla\Phi}{|\nabla\Phi|} \in \mathfrak{R}^3$ agrees, at the interface, with the normal to $\Gamma_{lg}(t)$ pointing away from the liquid domain. Hence, equation (26) can be equivalently expressed as

$$\frac{\partial\Phi}{\partial t} + V|\nabla\Phi| = 0,$$

where $V = -\mathbf{u}^t \cdot \mathbf{n}^t$, and the discontinuity of the tangential component of the convective field present in the continuity equation can thus be ignored without further ado. Note however, that approximations of the fluid flow field are usually continuous so one might as well use equation (26), and as a matter of fact this is often a better choice.

However practical and often assumed in the standard level set method, it is not necessary that Φ is a distance function. It is merely required that the level set function is zero on the interface and that the transition zone, i.e. the zone in which the Heaviside function varies, extends only over a few elements, so that when assigning properties to the fluid in the transition zone by weighting the properties of the adjacent fluids in the same manner as for the denisty, the solution tends towards the corresponding solution obtained when the CSF formulation is not utilized, as the mesh size tends to zero. The complication of the standard level set method is that even if we initialize Φ to be a signed distance function, it does not necessarily keep its nice features when evolving it according to the continuity equation only. This is why the level set function of the standard level set method has to be reinitialized every now and then. Since reinitialization has a positive effect on the shape and size of the phase transition zone, one cannot completely avoid all kinds of reinitialization. However, an alternative level set formulation, together with a reinitialization technique, was proposed in [64]. It was noticed that the thickness of the transition zone is often smeared out, and that this behaviour can be suppressed by employing a reinitialization technique that utilizes a flux for Φ in the direction pointing towards the interface. This direction can, as we have seen, be expressed using the level set function itself. The flux has the effect of pushing the isolevels of the level set function (i.e. the level sets) towards the interface, thus limiting the thickness of the zone. Also, a diffusion term was added in order to avoid discontinuities at the interface. Based on this approach, COMSOL has developed a level set method in which the compressive flux is added to equation (26), and no separate reinitialization step is required. The amount of compressive flux and diffusion in the level set equation ofcourse has to be traded against mass conservation. We have adopted this modelling strategy for an axi-symmetric test case involving a droplet falling into a liquid pool under the influence of gravity only. In this test case we have not considered the solid phase but instead applied no slip conditions on the walls of the cylindrical pool. In other respects, the settings are chosen as in the fillet case study. The results is shown in figure 14.

If we wish to model also the solid phase we must consider a three-phase modelling strategy. The naive approach is to simply apply the equations we have developed for the interface tracking problem, which effectively includes a volume of fluid method for the solid-liquid interface. We immediately run into problems since the properties of the fluid we have considered so far are dependent only upon the value of the temperature at a certain point. The property is now also dependent upon the value of the level set function at that point. If we are to continue in a straightforward manner, we must first figure out how to define the liquid fraction in the gaseous phase as a function of temperature only. For example, if we use the same expression as before for the effective viscosity, but now also weigh it using the level set function, we obtain

$$\mu = \mu_g + \left(10^5 \left[\frac{\mu_m}{10^5} \right]^{f\sigma T} - \mu_g \right) H_\epsilon \circ \Phi.$$

If we use the same expression for f as before, and the temperature of the gas is lower than the melting point of the base material, we find that

$$\mu = \mu_g + \left(10^5 \left[\frac{\mu_m}{10^5} \right]^{0.5} - \mu_g \right) 0.5 \approx 10^{2.5} \mu_m^{0.5},$$

i.e. a liquid droplet is surrounded by very viscous shell. This phenomena can be seen to appear no matter how the viscosity is taken to vary with T between the liquid and solid phases. The best one can hope for is that the gas is hotter than the liquid, in which case we instead find that the viscosity in the transition zone between the solid and gaseous domains depend on the viscosity of the liquid, but not even this is entirely to our satisfaction.

We see two ways of getting around the problem. One of them is well-known, and it involves solving an equation for f which evolves the location of the liquid domain in a manner similar to the one for Φ . The other way is to couple the interface tracking method for the weld pool and workpiece to a level set method for the arc region, using domain decomposition. The deposition of filler metal droplets into the weld pool can then, as before, be modelled as a mass density source or by a mesh velocity source which is dependent upon the velocity and mass density in the arc region. We note also that if we are to simulate the arc and pool during an autogeneous process, the previous developed model using interface tracking works well if domain decomposition is applied, and no three phase modelling is required.

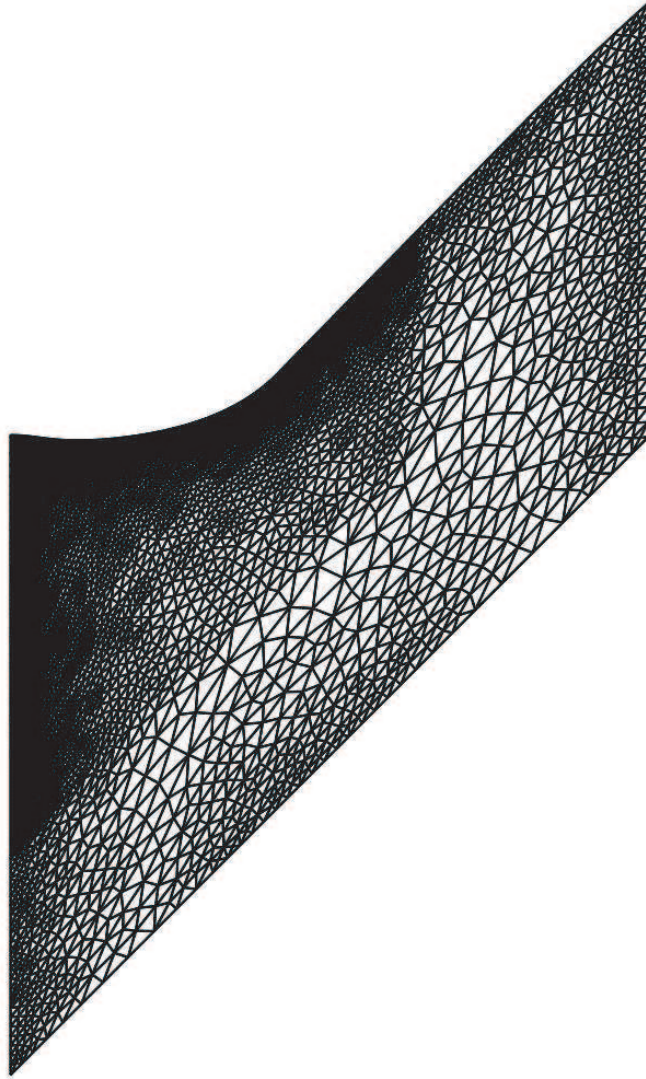


Figure 12: An approximation of the spatial configuration of the mesh as the weld has solidified. In this picture the spatial locations of the element nodes are according to the solution, however they are connected by straight lines instead of the quadratic curves which define the locations of the edges.

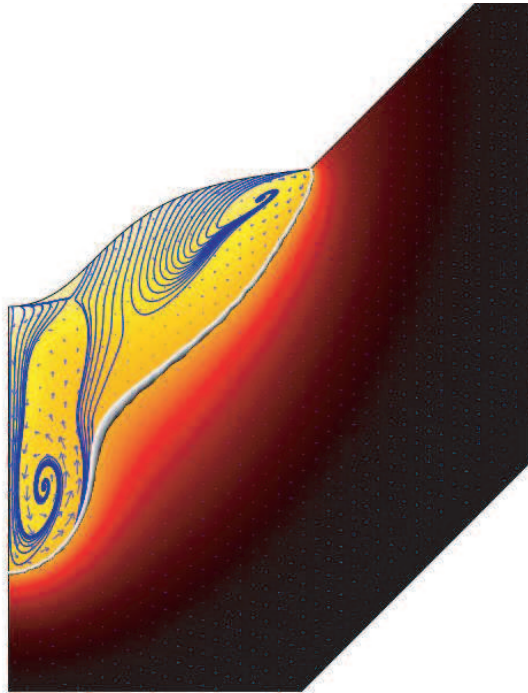


Figure 13: Flow field at a distance of 1.5mm behind the arc.

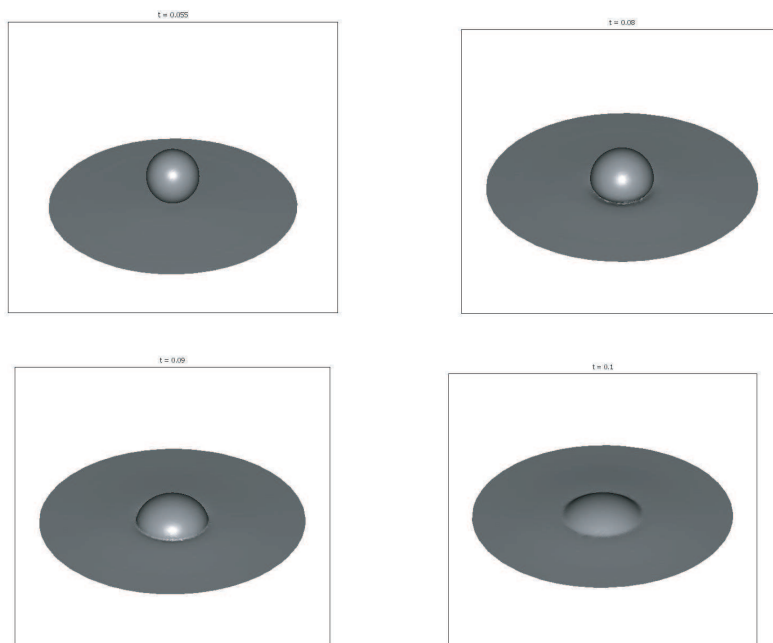


Figure 14: A droplet dropped into a liquid pool.

7 Calibration and Verification

In this section we present the results of a calibration of the relaxation parameter for the fillet case study. However, since the non-autogeneous model has proven somewhat difficult to work with, we restrict our attention to an autogeneous GTA butt weld when verifying the computational results against fusion zone shape for a weld case that requires only a calibration of the temperature coefficient of surface tension. Preferably, we would like to calibrate the pool shape against measurements, however no such data has been obtained within our project.

It should be pointed out that it is not practical to simultaneously optimize the model with respect to all input parameters in a calibration procedure (virtually all data in our model can be subject to calibration). Therefore, the parameter set should be reduced for the specific process that is considered. The calibration then outputs effective values for the unknown parameters, for which the model can be assumed to output reliable predictions for similar cases. In the verification of the GTA fusion zone shape prediction, we have access to data from a related study, and we may calibrate with respect to the effective value of A only.

7.1 Incompressibility relaxation

The value $C_\epsilon = 10^{-5}$ that was used in the fillet case study, conserved the mass by 99.98%. The reason for introducing the relaxation in the first place, was to decrease the computational time, so calibrating the C_ϵ is a matter of deciding how much mass loss/increase one is prepared to accept. In order to find an optimal value of the relaxation coefficient, we therefore run the test case for a range of values for C_ϵ , namely $10^{-3}, 10^{-4}, 10^{-5}, 10^{-6}, 10^{-7}, 10^{-8}$. For the value $C_\epsilon = 10^{-3}$, the computations did not converge. In figure 15, the mass conservation ratio (the added mass in the computational model to the added mass in the purely incompressible mathematical model) is plotted against the negative 10-logarithm of C_ϵ . As we see, perfectly acceptable mass conservation is obtained for $C_\epsilon = 10^{-5}$, and there is no need to decrease it further. Lets look at the simulation times for the same runs (figure 16); Except for the first run in the test series, for which mass conservation was not entirely good, we see that simulation times increase slightly with decreasing values of the relaxation parameter. The conclusion is that the value $C_\epsilon = 10^{-5}$ is a good starting guess when applying the developed model.

7.2 Calibration of the temperature coefficient of surface tension and verification of fusion zone shape for a linear autogeneous GTA bead-on-plate weld

In [69] the arc efficiency and spot radius for the heat source was calibrated for a linear autogeneous GTA bead-on-plate welding process, using the weld surface temperature as measured by an IR-camera, see figure 17. At first attempt at

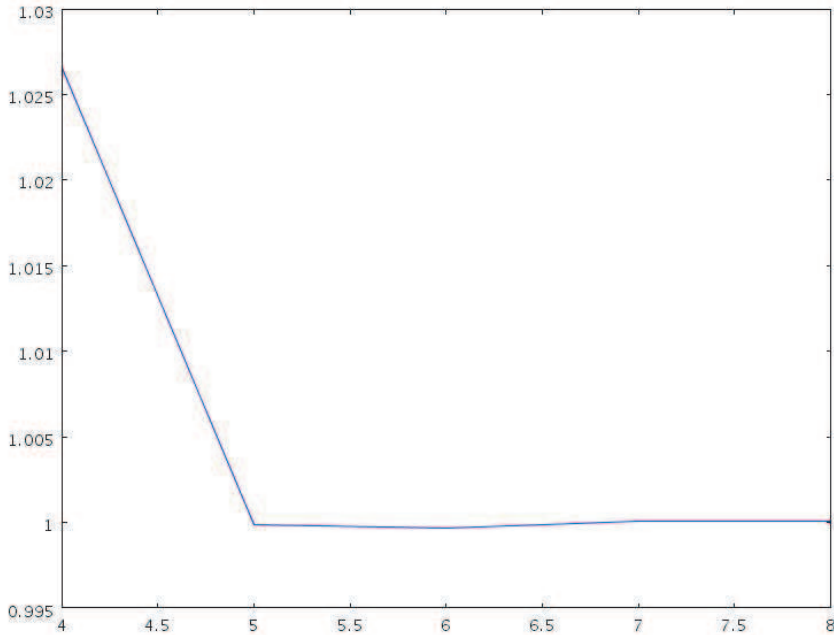


Figure 15: Mass conservation ratio plotted against the negative 10-logarithm of C_ϵ .

recreating the fusion zones of the welds in this set of experiments, we ignore arc pressure, set the incident current radius equal to half of the heat source spot radius, and approximate many of the material properties from the data given in [61] for the base material, which is steel 316. However, the value of the magnetic permeability, which can be assumed to have an impact on the fusion zone shape, is not known. We employ the value used in [91] for another type of steel. We reduce the set of uncertain input parameters further by incorporating the values of the heat transfer coefficients along the different workpiece surfaces, which are used in [40] and [91]. Since no mass is added, the incompressibility condition is not relaxed. A difficulty is that, according to the relations recommended in [61], the value of the surface tension and its temperature coefficient is strongly dependent upon the sulphur content of the base material, the precise value of which in our case is unknown. The value of A even switches sign within reasonable limits for the sulphur content. We therefore employ the value for γ_m also used in [91], and perform a calibration of A . Considering what we learned from the fillet case study, we may suspect that the fusion zone shape is determined by the relative influence of the circulating motions induced by the electromagnetic force and the Marangoni force.

Having run a number of simulations we find that the size of the pool is

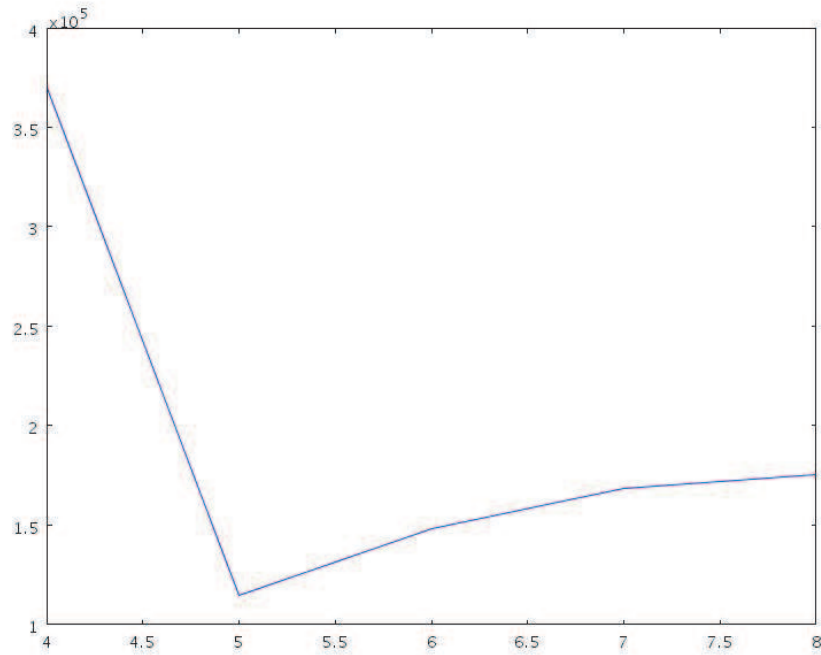


Figure 16: Simulation times plotted against the negative 10-logarithm of C_e .



Figure 17: Experimental setup for measuring the surface temperature during a GTA welding process.

repeatedly overestimated when using the value $\mu_s = 0.8962$ that was calibrated in [69]. We set instead the arc efficiency of the surface source to 0.7. It is plausible that the reduction of the size of the pool that this setting causes could be obtained by instead calibrating the heat transfer coefficients as well as the

spot radius, or by employing an effective value for the heat capacity which is allowed to vary with temperature in the pool. What more is, the value 0.7 was found by trial and error, so in a sense the arc efficiency has also been calibrated, however not in formal fashion but rather by *hand-weaving*.

We have hitherto extracted the fusion zone shape from the result of a simulation by manually searching through the isocontours of the temperature at different times. In order to avoid this cumbersome procedure, we now add an equation for an independent field variable f_{sol} , the value of which at a certain spatial point approximates the solidification time, i.e. the time that spatial point spent in the mushy zone during solidification. This way we may visualize the FZ shape by plotting the isocontour $f_{sol} = \epsilon_{FZ}$, where ϵ_{FZ} is a small positive number, however not zero since f_{sol} has no zero isocontour. What more is, the solidification time can be input to metallurgical simulations of the weld, c.f. section 8.2. The equation we employ is the following;

$$\int_{\Omega_0} \left[\frac{\partial \hat{f}_{sol}}{\partial t} - \nabla_{(X,Y)} \hat{f}_{sol} \mathcal{J}_\omega^{-1} \frac{\partial \omega}{\partial t} \right] |_{\mathcal{J}_\omega} \hat{f}_{sol} = \int_{\Omega_0} \left(\frac{\partial \hat{T}}{\partial t} < 0 \right) (\hat{T} < T_m) (\hat{T} > T_s) |_{\mathcal{J}_\omega} \hat{f}_{sol} \quad (27)$$

where $(\frac{\partial \hat{T}}{\partial t} < 0)(\hat{T} < T_m)(\hat{T} > T_s)$ is a function which is one whenever and wherever the parenthesized expressions are all true, and zero otherwise. It turns out that we usually need to set ϵ_{FZ} to a value between 0.01 and 0.1 depending on the mesh size, in order to compensate for the inaccuracy in the solution of equation (27). The error is likely due to numerical diffusion, caused by the discontinuity of the coefficient in the right hand side of equation (27). The value of ϵ_{FZ} is found by matching the f_{sol} isocontour to the $T = T_s$ isotherm curve at the weld and root surfaces, at the times when the pool widths at the respective surfaces were at their widest.

The simulations were run for $A = 10^{-6}[1, 2, 3, 4, 5, 6, 7, 8, 9, 10]$, and with the same value of the weld parameters (travel speed, voltage and current) as were used in the experiment that produced the weld with the cross section shown on the left side in figure 19. Due to the limited deformation of the pool surfaces, we employ the model which allows the mesh to move in the y -direction only, and applies a penalizations method for the y -direction mesh velocity at the weld and root surfaces. This approach has proven to be very useful so far, but for the first four simulation runs in the series, a disturbing phenomena occurs, which comprises that wiggles in the mesh appear on the root side as melt-through is initiated, see figure 18. An investigation of the difference between the fluid velocity and the mesh velocity discloses that the kinematic boundary constraint was violated. We recall from the fillet weld case study, that A seems to have a smoothing effect on the mesh, which may explain why the calculation manage to converge without wiggles for the value $A = 5 \times 10^{-6}$. However, for the fillet case, the main problem with the kinks were solved by applying the penalization technique instead of the multiplier technique, and that seemingly does not do the trick in this situation. The simulations thus did not provide any useful information about the value of A however it did hint that the values of the

arc efficiency and the incident current radius should be modified, and that the simulation results are quite sensitive to the value of A . For the next series of simulations, we therefore instead set $\eta_s = 0.725$ and $\sigma = 0.3a$, and run the simulations for $A = 10^{-6}[1, 2, 3, 4, 5]$. Also, a coarser mesh was used. In this test series, no wiggles appear at the root side. We have no intention to further investigate the wiggling phenomena in this treatise, but are content that it has vanished for now.

A reasonable agreement between the measured and simulated FZ shapes were obtained for $A = 10^{-6}$. A comparison between the real and simulated fusion zones for the melt-through weld against which A was calibrated, is shown in figure 19. The widths at the weld surface and root surface agree reasonably well. There is some ambiguity in the location of the fusion zone line, both when considering the real weld and when considering the simulated weld. The ambiguity is possibly due to inaccuracy in the measurements, the possibility of oxides on the surface, numerical errors, and modelling errors (from not taking into account the solid state transformations the results of which are visible in the photographs taken of the weld transversal cuts). As can be seen, the root side shape of the weld surface is not accurately rendered. This is may very well be due to the fact that we have ignored the arc pressure in this calibration, since the arc pressure pushes the pool towards the root side.

We now verify the simulation against one other run in the same test series, using the same value for A but other values for the voltage and current. A comparison between the real and simulated fusion zones is shown in figure 20. As can be seen, the weld surface is convex. The weld was performed autogenously, so the volume of mass required to establish this reinforcement is most likely due to transversal shrinking or thermal expansion, neither of which we consider in the simulations. Although fusion zone is not entirely erroneous, we conclude that more than one parameter should be calibrated simultaneously in order to obtain better predictions of the fusion zone shapes. What more is, even if the FZ shape is correct, we cannot be certain that the pool shape is accurately predicted. This is a reason for investigating the effect of the arc pressure, and such a study is presented in section 8.4.

We conclude the present study of the linear autogeneous GTA bead-on-plate weld by speculating about the sensitive of the FZ shape to the value of A . We have run several simulations more than have been presented so far, particularly for finding an appropriate value for the arc efficiency. These were isolated runs and not part of any parameter study or (formal) calibration procedure, which is why we cannot draw any definite conclusions from them. However, we have found that when the value of A is high, the pool widening effect of the Marangoni induced circulating motion dominates. No melt-through of the plate then occurs, and we obtained a completely erroneous shape of the FZ, since melt-through did occur during the real welding process. A slight decrease in A allows for the digging effect induced by the Lorentz force to increase its influence on the pool shape. When A is decreased further, melt-through occurs, and Marangoni forces now act on the root side pool surface. The root side Marangoni force and the Lorentz force now both act to strengthen the circulat-

7.2 Calibration of the temperature coefficient of surface tension and verification of fusion zone shape for a linear ar

ing flow pattern which tends to widen the width of the pool on the root side.
This seems to be the reason why the FZ shape is sensitive to the value of A .

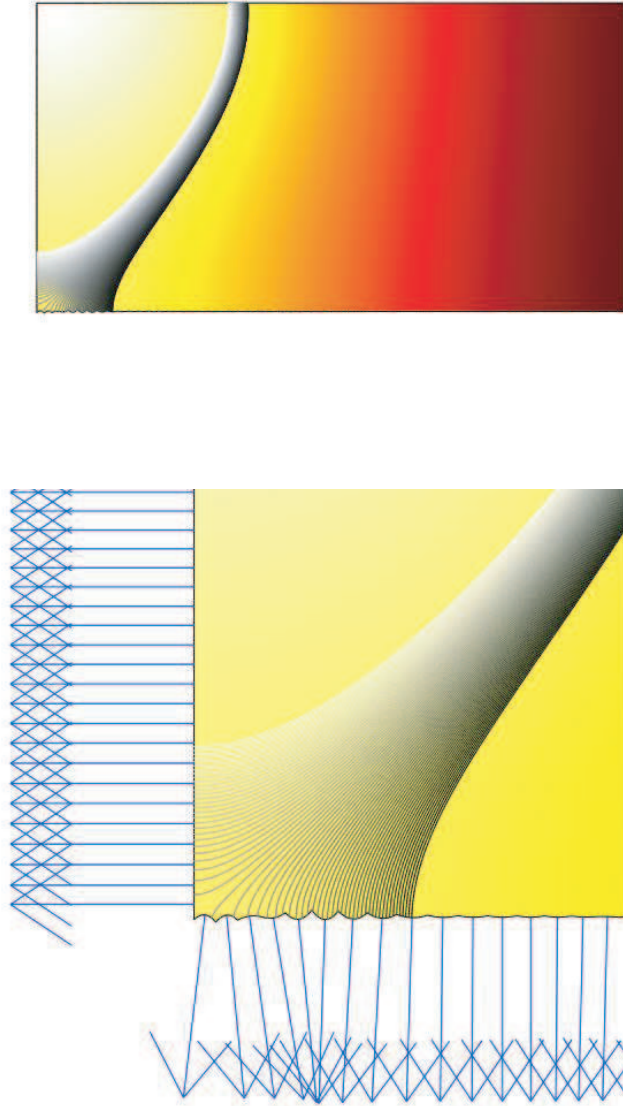


Figure 18: Wiggles in the mesh appear as melt-through is initiated. In the close-up picture, surface normals are shown. The left boundary is the symmetry line, which is not deformed.

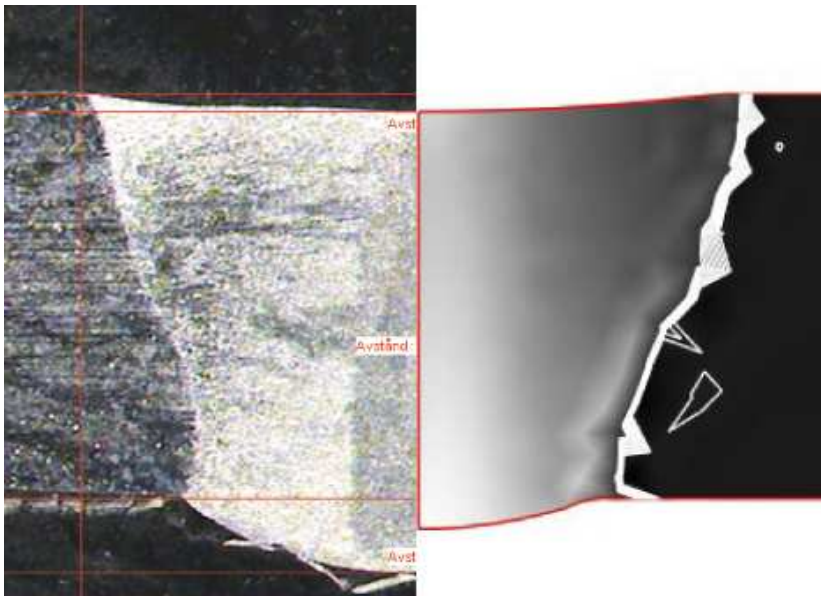


Figure 19: On the left; A cross-section of the weld against the dimensions of which the surface tension coefficient was calibrated. On the right; Simulated fusion zone shape. The surface is color mapped to the value of f_{sol} . The white region which marks the location of the fusion zone line is the set of isocontours of f_{sol} corresponding to the values $f_{sol} = 10^{-2}[1, 2, \dots, 10]$.

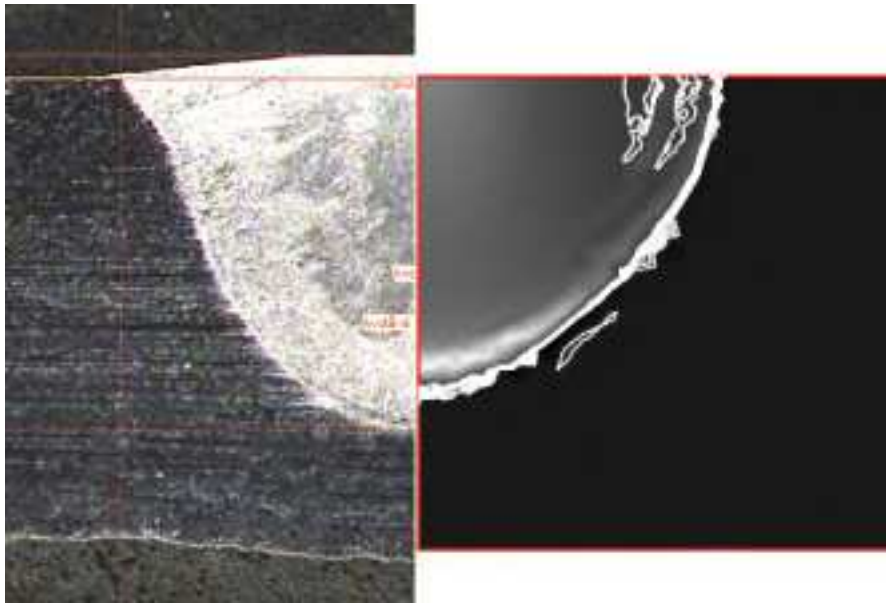


Figure 20: A comparison between measured and simulated fusion zone shapes..

8 Applications and Conclusions

8.1 Welding out-of-position

If the settings used in the fillet case study are applied to a welding process which is performed upside down, the calculations fail to converge when the arc has passed the computational slice by 0.15mm. The configuration is then as in figure 21. By this time, the Jacobian determinant of the configuration had

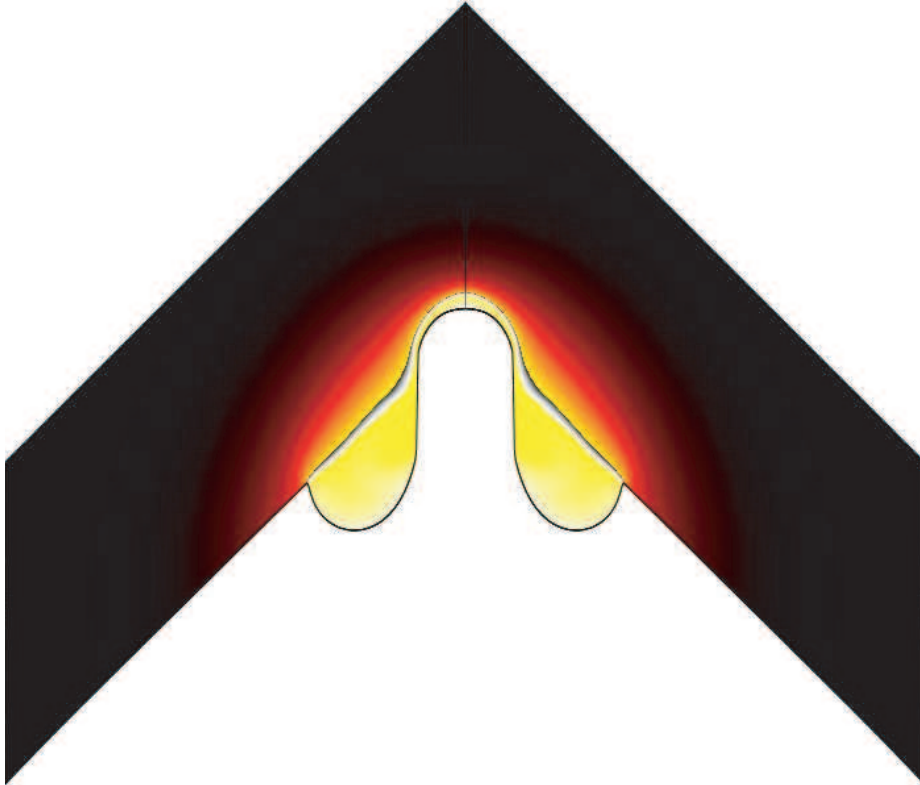


Figure 21: Configuration at 0.15mm behind the arc when welding at 362A. The problem we solve is symmetric, but for the sake of visual appearance we have in this picture reflected the workpiece slice in the symmetry plane and superimposed it onto the original one.

already switched sign at the triple point, so the result is not valid according to our theory. This could perhaps be avoided by employing the formulation in which the mesh is allowed to move in any direction, however it turns out that we cannot define an efficient method that penalizes two variables for violating the same scalar constraint. As we have seen, neither does the multiplier technique work very well when encountering this type of configuration.

It is interesting, and computationally challenging, to investigate whether the

pool can be kept in place during welding in PD position, and adequate penetration achieved, by increasing the source ampereage and thus also modifying the arc pressure according to the expression employed in [90] (similar expressions are also used in [55] for studying different welding positions). It is a fact that GMA welding in this position is performed, so this is rather an investigation made in order to find out if our simulation tool can handle this situation. We run simulations for a set of values for the current which are percentages of the current used in PA position, the highest of which is $1.5 \times 362I$. The simulations do not show that the melt can be kept in place by modifying the current only. As the current is increased from its original value, the pressure also increases, however so does the effective heat input to the workpiece, which makes the melt larger and more difficult to keep in place c.f. figure 22. The simulations all fail to converge at approximately the same arc positions.

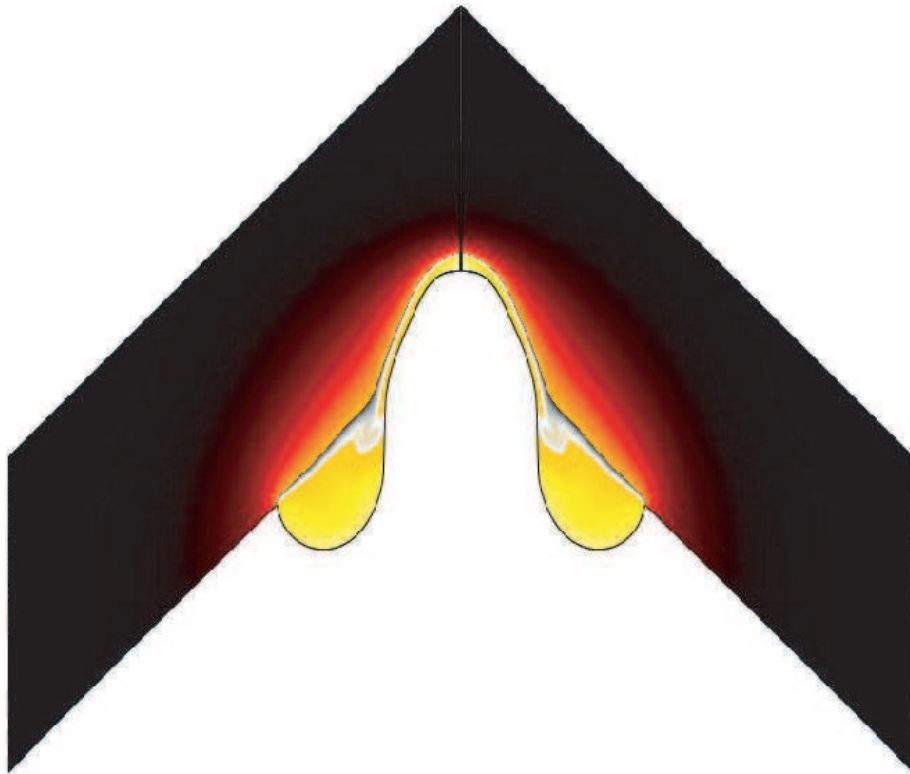


Figure 22: Configuration at 0.3mm in front of the arc when welding at 543A. As can be seen, the penetration of the workpiece has increased, but not in a very useful manner.

8.2 Metal deposition and metallurgical simulations

Metal deposition is process during which metal is melted and deposited onto a workpiece to which it fuses. The purpose is to repair or create from scratch a component with certain characteristics such as a predefined shape and durability. The process can be performed using non-autogenous fusion welding equipment, and several passes of the source are required in order to establish the geometry. At each pass, the previously deposited metal layer (bead) is partially remelted, however only as much as is required for the fusion with the subsequently deposited layer. The heat distribution and the shape of the solidified bead can be studied using the simulations tool developed in this treatise, as was done in [22]. The output of such simulations, i.e. the reinforcement geometry and temperature distribution within the bead, can be input to a simulation calculating for example the dendrite arm spacing and grain growth directions in the layers of the wall, which impact on the performance of the component.

8.3 Laser welding

Simulations of conduction mde laser weld pools were performed within the INN-Side project. As is evident from equation (9), it is largely so that it is the ratio between the welding direction flux and the welding speed determines whether our model, without modification, successfully can be applied to a specific welding process. The welding speed during laser welding is high in comparison to electric arc welding methods. However, the energy density of a laser welding process is also comparatively high, and so it can be expected that the welding direction flux is too. We have attempted to recreate a number of those laser welding fusion zones described in [67], but have not managed to obtain accurate penetration. This verifies that the welding direction expansion of a laser weld pool is foremost due to conduction through the workpiece of the heat absorbed in the key-hole or cavity. Even though the welding speed is high, the concentrated heat source gives rise to large temperature gradients near the pool. We have therefore attempted two modifications to the two-dimensional model; First we consider a longitudinal workpiece slice instead of a transversal one. This will account for heat flow in the welding direction. Secondly, we have managed to take into the possibility of substantial evaporation of the base metal, a phenomena that should not be ignored when simulating high density energy pools. When doing so we have utilized the different models for mass deposition that we have developed. When adding material to a weld pool, we have seen that the energy it carries cannot be controlled without specifying the temperature at the locations where the mass is added. However, by applying the mass deposition model in reverse, we can implement a simple evaporation model which removes exactly the material the temperature of which exceeds the evaporation point of the base material. Preliminary results show that the simulated penetration depth increases significantly when considering evaporation in this fashion, in comparison to not taking into account at all.

In parallell, we have begun working on a three-dimensional time-dependent

model. So far we have made only simulations of the heat flow and mass deposition, an example of which can be found on the cover of this thesis.

8.4 The influence of arc forces on the probability of overlap

As we approach the end of our work, it is good to remind ourselves why we started it. Hence we study in this section the probability of overflow as a function of the arc pressure, overflow being one of the reasons for the appearance of cold laps at the weld toe. This we do for the linear autogeneous GTA bead-on-plate weld which served as a verification case in section 7.2. This study is mainly of theoretical interest, since cold laps are usually not a such a big problem as in consumable arc welding processes, such as GMA welding of fillet joints. However, the GTA simulation was calibrated, so can allow ourselves to put a relatively large amount of trust in its output.

When adding the arc pressure to the simulation, we at first employ the [90] expression for the arc pressure and impingement radius as functions of the source amperage. However, all other parameters remain the same throughout the study, including the applied current. The pressure parameters must thus be modified according to an artificial amperage, used only as a tool for modifying the pressure in a physical manner. This approach does not reveal much useful information concerning the probability of overflow, possibly because the arc pressure impingement radius increases as the total pressure increases while the pool width does not. This implies that the magnitude of the gradient of the applied force along the surface does not increase a lot as the artificial amperage increases. However, we do find that penetration is increased by the application of an arc pressure. It seems that the calibration of the model should have included the arc pressure to begin with, c.f. figure 23.

We now instead run a series of simulations in which the arc pressure radius remains equal to the heat source radius, and increase the total pressure according to $P_{arc} = 10^{-4}[10, 15, 16, 17, 18, 19, 20, 21, 22, 23, 24, 25, 30]$. Even better agreement with the verification case was achieved at $P_{arc} = 17 \times 10^{-4}$, se figure 24. As a measure of the probability of overlap we choose the maximum d_{max} of the distance in the arc axis direction between the highest elevated and deepest cavitated points on the pool surface, during the simulation. For $P_{arc} = 24 \times 10^{-4}$, $P_{arc} = 25 \times 10^{-4}$ and $P_{arc} = 30 \times 10^{-4}$ failed to converge as the source passed the computational slice, c.f. figure 25. This failure to converge is due to a severe deformation of the domain in the cavity. This would not necessarily be a problem in a real weld, on the contrary the cavitation helps to provoke penetration and is filled as the pool advances. There is no obvious reason why the possibility of overflow should be higher in this situation, but one should rather worry about the entrapment of gas bubbles in the pool which do not exit the pool before solidification and thus causes porosity. Yet we include these simulations, as they are part of a pattern. For the other runs, d_{max} is plotted against P_{arc} in figure 26 Except for the outlier, there is a clear cut trend in the simulation results. We do not dare to draw any conclusion about the reason for cold laps

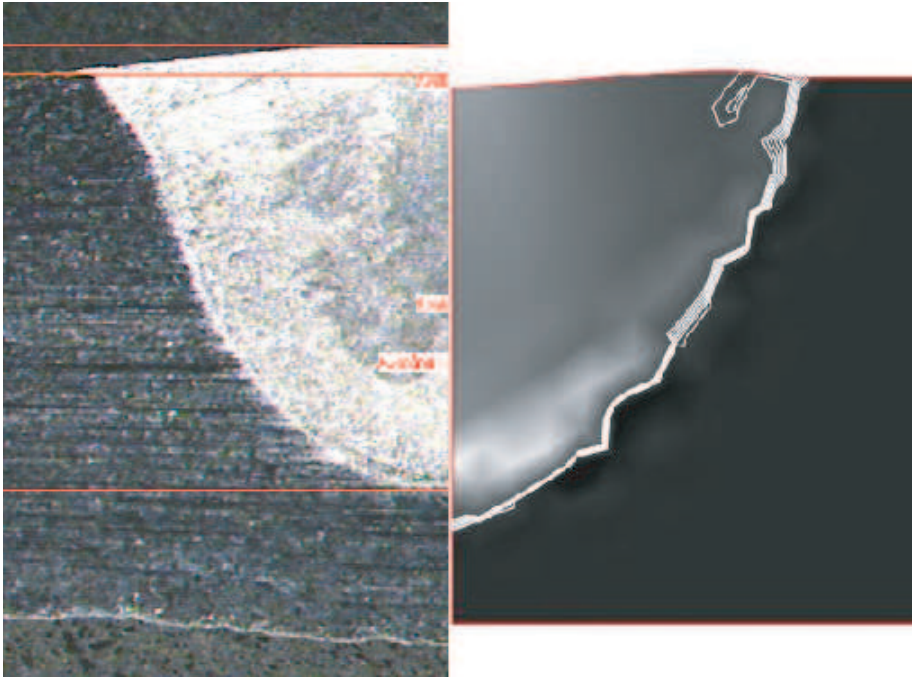


Figure 23: Better agreement with respect to penetration can be achieved if the arc pressure is considered.

from this study, however it shows that the fluid mechanical influence that the arc exercises on the pool plays an important role.

8.5 Summary, conclusions and future work

The work commenced with a literature study, but we did not find that previous research had attempted a fluid and thermo dynamical model for studying the kind of phenomena (overflow, spatter) that we supposed exercised a major effect on the appearance of defects related to solidification and cooling. A computational tool that simulates arc fusion weld pools with respect to fluid flow, temperature and pool deformation, and which is based upon a finite element model for the governing continuum mechanical equations, was developed and employed in a series of articles.

It was discovered that modelling the pool separately from the arc has some inherent drawbacks when considering non-autogeneous processes. Specifically, it is difficult to a priori define the amount and distribution of the energy transferred by the filler metal droplets. Therefore, a minor investigation into the possibilities of exploiting a three-phase modelling strategy which incorporates temperature, was undertaken. Some suggestions for pool-arc modelling strategies were presented.

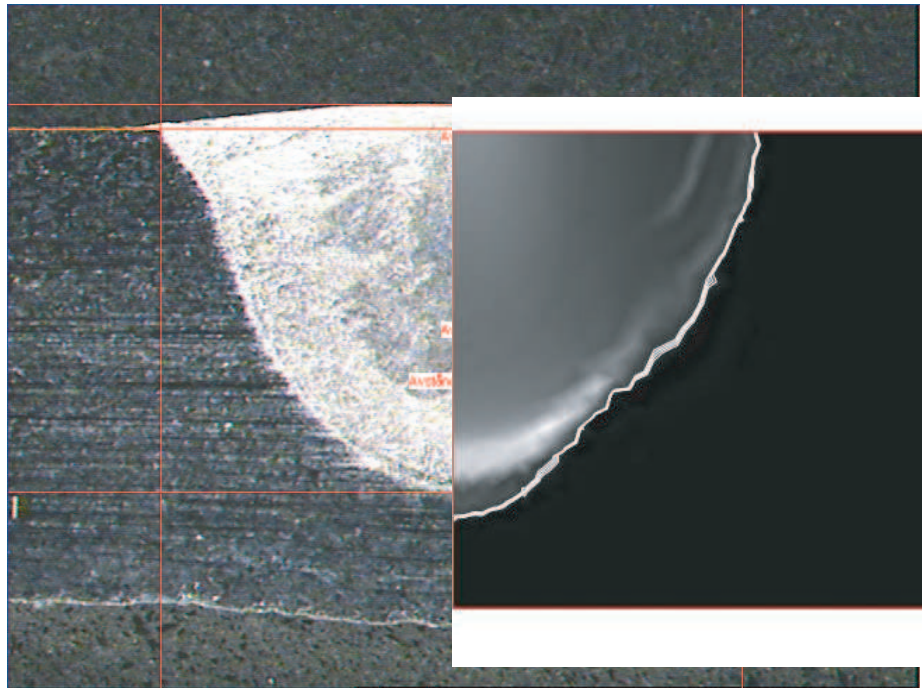


Figure 24: Even better agreement can be achieved if the total arc pressure and the arc pressure radius are entirely decoupled.

The effects of arc pressure on the probability of overlap was studied. It was concluded that it is important to accurately model (or measure) the arc pressure on the pool surface in order to predict the behaviour of the pool flow. We learned also from studying a GMA fillet weld that since mass cannot escape in the welding direction, the build up of material is greater in the two dimensional case. When studying the motion of the pool surface it might therefore be worthwhile to consider a three dimensional model, which preferably also takes into account transients in order to incorporate the effects of disturbances in the arc (such as voltage drops or arc wandering) or workpiece (such as irregularities in the weld surface).

In order to accurately predict weld shape and temperature distribution during non-autogenous welding, and also to predict weld defects related to the motion of the pool surface, it is recommended that the pool model is coupled to an arc model. Until then the tool should be used mainly for autogeneous weld pool simulations and for predicting the temperature history in the bead deposited during metal deposition, but only after having undertaken a model calibration which simultaneously optimizes the values of several parameters for the specific process.

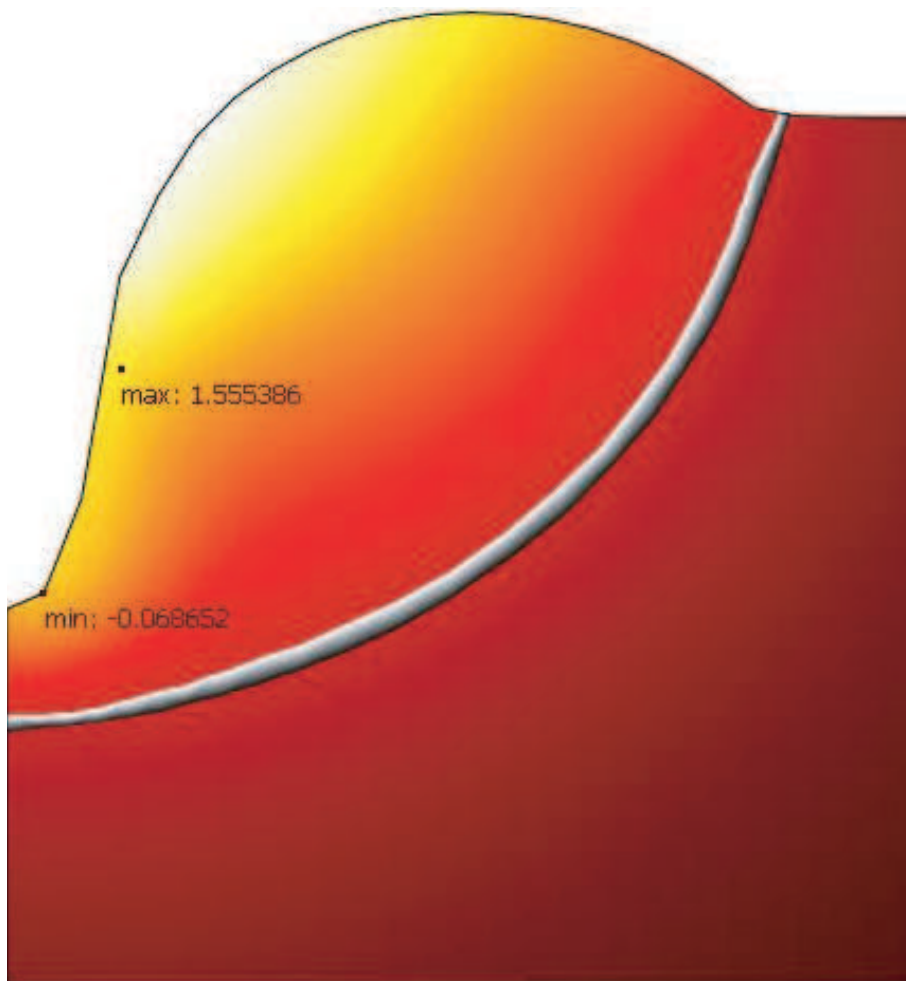


Figure 25: For $P_{arc} = 0.0025$, the mesh Jacobian turns negative in the cavity.

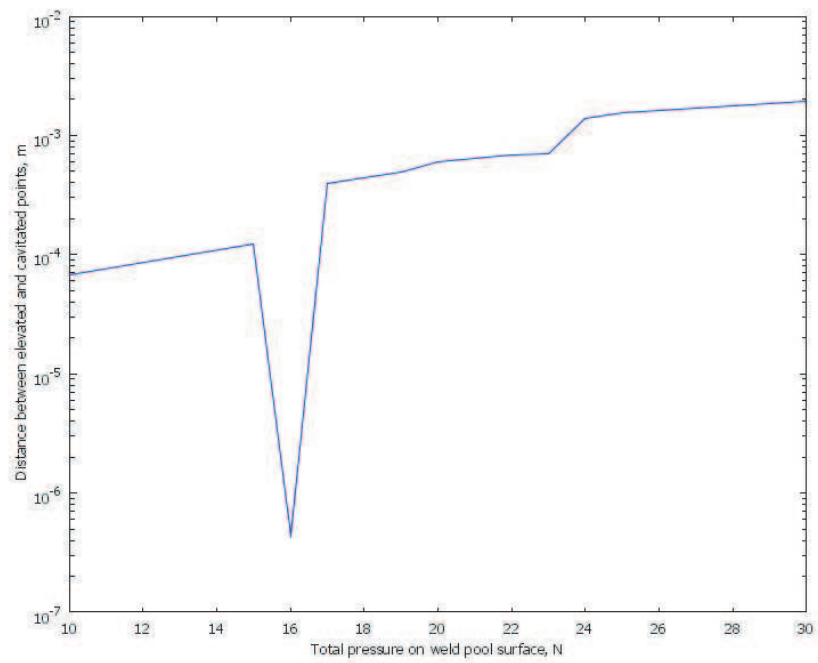


Figure 26: d_{max} against P_{arc} . The scale of the vertical axis is logarithmic.

References

- [1] M. Arenas, V.L. Acoff, and N. El-Kaddah, *Measurement and prediction of gta weld penetration in gamma titanium aluminide*, Mathematical Modelling of Weld Phenomena 5, IOM Communications Ltd, 2001, pp. 39–53.
- [2] Z. Barsoum, *Fatigue and quality analysis of cruciform joints welded with different methods*, Tech. report, International Institute of Welding, doc. XIII-2136-06.
- [3] K.B. Bisen, M. Arenas, N. El-Kaddah, and V.L. Acoff, *Computation and validation of weld pool dimensions and temperature profiles for gamma tial*, Metallurgical and Materials Transactions **34A** (2003), no. 10, 2273–2279.
- [4] K.E. Brenan, S.L. Campbell, and L.R. Petzold, *Numerical solution of initial-value problems in differential-algebraic equations*, Elsevier Science Publishing, 1989.
- [5] P.N. Brown, A.C. Hindmarsh, and L.R. Petzold, *Using krylov methods in the solution of large-scale differential-algebraic systems*, Journal of Scientific Computing **15** (1994), no. 6, 1467–1488.
- [6] W. Cao, W. Huang, and R.D. Russel, *A moving mesh method based on the geometric conservation law*, Journal on Scientific Computing **24** (2002), no. 1, 118–142.
- [7] Z.N. Cao and P. Dong, *Modeling of gma weld pools with consideration of droplet impact*, Journal of Engineering Materials and Technology **120** (1998), 313–320.
- [8] N. Chakraborty, S. Chakraborty, and P. Dutta, *Modelling of turbulent transport in arc welding pools*, International Journal of Numerical Methods for Heat and Fluid Flow **13** (2003), no. 1, 7–30.
- [9] ———, *Three-dimensional modeling of turbulent weld pool convection in gtaw processes*, Numerical Heat Transfer **Part A** (2004), no. 45, 391–413.
- [10] K. Chattopadhyay, G. Phanikumar, and P. Dutta, *Modelling of transport phenomena in laser welding of dissimilar metals*, International Journal of Numerical Methods for Heat and Fluid Flow **11** (2001), no. 2, 156–171.
- [11] F.K. Chung and P.S. Wei, *Mass, momentum, and energy transport in a molten pool when welding dissimilar metals*, Journal of Heat Transfer **121** (1999), 451–461.
- [12] S.A. David and J.M. Vitek, *Analysis of weld metal solidification and microstructures*, Mathematical Modelling of Weld Phenomena (H. Cerjak and K.E. Easterling, eds.), The Institute of Materials, 1993, pp. 41–59.
- [13] P.A. Davidson, *An introduction to magnetohydrodynamics*, Cambridge University Press, 2001.

- [14] M.H. Davies, M. Wahab, and M.J. Painter, *An investigation of the interaction of a molten droplet with a liquid weld pool surface: a computational and experimental approach*, *Welding Journal* **79** (2000), no. 1, 18–23.
- [15] T. DebRoy, *Weld pool surface phenomena - a perspective*, *Mathematical Modelling of Weld Phenomena* (H. Cerjak and K.E. Easterling, eds.), The Institute of Materials, 1993, pp. 24–38.
- [16] T. Debroy, *Role of interfacial phenomena in numerical analysis of weldability*, *Mathematical Modelling of Weld Phenomena 2* (H. Cerjak, ed.), The Institute of Materials, 1995, pp. 4–21.
- [17] T. DebRoy, *Mathematical modelling of fluid flow and heat transfer in fusion welding*, *Mathematical Modelling of Weld Phenomena 5*, IOM Communications Ltd, 2001, pp. 1–20.
- [18] M Do-Quang and G. Amberg, *Modelling of time-dependent 3d weld pool flow*, *Mathematical Modelling of Weld Phenomena 7* (H. Cerjak, H.K.D.H. Bhadeshia, and E. Kozeschnik, eds.), Verlag der Technischen Universität Graz, 2005, pp. 91–112.
- [19] M. Do-Quang and G. Amberg, *Modelling of time-dependent 3d weld pool due to a moving arc*, *Proceedings of High Performance Scientific Computing*, Hanoi, March 2003.
- [20] J.N. DuPont and A.R. Marder, *Thermal efficiency of arc welding processes*, *Welding Journal* **74** (1995), no. 12, 406–416.
- [21] M. Edstorp, *A dislocation based technique for the simulation of the fatigue growth of initiated microcracks*, Master’s thesis, University of Gothenburg/Chalmers University of Technology, Department of Mathematics, 2003.
- [22] ———, *A comparison between moving mesh implementations for metal deposition simulations*, *Proceedings of the Nordic Comsol Conference* (Lynby, Copenhagen, Denmark), November 2006, pp. 107–110.
- [23] ———, *A simplified finite element formulation for spray transfer gma weld pools*, *Progress in Industrial Mathematics at ECMI 2006* (L.L. Bonilla, M. Moscoso, G. Platero, and J.M. Vega, eds.), *Mathematics in Industry*, vol. 12, The European Consortium for Mathematics in Industry, Springer, 2007, pp. 822–826.
- [24] M. Edstorp and K. Eriksson, *Modelling and simulation of moving boundaries and convective heat transfer in non-autogenous fusion weld pools using femlab 3.1*, *Proceedings of the FEMLAB CONFERENCE 2005* (J Yström, ed.), October 2005, pp. 85–90.
- [25] A. Ern and J.-L. Guermond, *Theory and practice of finite elements*, *Applied Mathematical Sciences*, vol. 159, Springer, 2003.

- [26] H.G. Fan and R. Kovacevic, *Droplet formation, detachment, and impingement on the molten pool in gas metal arc welding*, Metallurgical and Materials Transactions **30B** (1999), 791–801.
- [27] ———, *A unified model of transport phenomena in gas metal arc welding including, electrode, arc plasma and molten pool*, Journal of Physics D: Applied Physics **37** (2004).
- [28] M. Farajian-Sohi and N. Järsvstråt, *Formation and detection of imperfections in tandem gas-shielded metal arc welding*, unpublished.
- [29] ———, *Formation and detection of weld toe imperfections in tandem gas metal arc welding*, Tech. report, International Institute of Welding, 2005, Doc.212-1074-05.
- [30] ———, *A fractographical investigation of weld toe imperfections in tandem gas metal arc welding*, Steel Research International **77** (2006), no. 12, pp 889–895.
- [31] M. Farajian-Sohi, N. Järsvstråt, and B. Jonsson, *Surface geometry measurements and the experimental and numerical investigation of stress concentration in fillet welds*, 59th Annual Assembly and the International Conference of the International Institute of Welding, Quebec, 2006.
- [32] M. Farajian-Sohi, N. Järsvstråt, and M. Thuvander, *Effect of welding parameters on formation of toe imperfections in tandem gas metal arc welding*, ASM 7th International Conference on Trends in Welding Research, Pine Mountain, Georgia, USA, May 16-20 2005.
- [33] C.V. Goncalves, L.O. Vilarinho, A. Scotti, and G. Guimaraes, *Estimation of heat source and thermal efficiency in gtaw process by using inverse techniques*, Journal of Materials Processing Technology (2006), no. 172, 42–51.
- [34] M. Goodarzi, R. Choo, T. Takasu, and J.M. Toguri, *The effect of the cathode tip angle on the gas tungsten arc welding arc and weld pool ii. the mathematical model for the weld pool*, Journal of Physics D: Applied Physics (1998), 569–583.
- [35] J. Haidar, *A theoretical model for gas metal arc welding and gas tungsten arc welding. i*, Journal of Applied Physics **84** (1998), no. 7, 3518–3529.
- [36] C.R. Heiple and J.R. Roper, *Effect of selenium on gtaw fusion zone geometry*, Welding Journal **60** (1981), no. 8, 143–145.
- [37] ———, *Mechanism for minor element effect on gta fusion zone geometry*, Welding Journal **61** (1982), no. 4, 97–102.
- [38] C.R. Heiple, J.R. Roper, R.T. Stagner, and R.J. Aden, *Surface active element effects on the shape of gta, laser, and electron beam welds*, Welding Journal **62** (1983), no. 3, 72–77.

- [39] K. Hong, D.C. Weckman, and A.B. Strong, *The influence of thermo-fluids phenomena in gas tungsten arc welds in high and low thermal conductivity metals*, Canadian Metallurgical Quarterly **37** (1998), no. 3-4, 293–303.
- [40] K. Hong, D.C. Weckman, A.B. Strong, and W. Zheng, *Modelling turbulent thermo-fluid flow in stationary gas tungsten arc weld pools*, Science and Technology of Welding and Joining **7** (2002), no. 3, 125–136.
- [41] D. Honggang, G. Hongming, and W. Lin, *Heat transfer and fluid flow in fusion type pa-gta double-sided welding*, MODELLING AND SIMULATION IN MATERIALS SCIENCE AND ENGINEERING (2005), no. 13, 1205–1215.
- [42] J. Hu and H.L. Tsai, *Heat and mass transfer in gas metal arc welding, part i, the arc*, International Journal of Heat and Mass Transfer **50** (2007), 833–846.
- [43] M. Hughes, K. Pericleous, and N. Strusevich, *Modelling the fluid dynamics and coupled phenomena in arc weld pools*, Mathematical Modelling of Weld Phenomena 6 (H. Cerjak, ed.), Maney Publishing, 2002, pp. 63–81.
- [44] P.G. Jönsson, J. Szekely, R.T.C. Choo, and T.P. Quinn, *Mathematical models of transport phenomena associated with arc-welding processes, a survey*, Modelling Simul. Mater. Sci. Eng. (1994), no. 2, 995–1016.
- [45] M. Kanouff and R. Greif, *The unsteady development of a gta weld pool*, International Journal of Heat and Mass Transfer **35** (1992), no. 4, 967–979.
- [46] V.A. Karkhin, H.J. Pesch, A.S. Ilin, A.A. Prikhodovsky, V.V. Plochikhine, M.V. Makhutin, and H.-W. Zoch, *Effects of latent heat of fusion on thermal process during welding*, Mathematical Modelling of Weld Phenomena 7 (H. Cerjak, H.K.D.H. Bhadeshia, and E. Kozeschnik, eds.), Verlag der Technischen Universität Graz, 2005, pp. 3–37.
- [47] C.-H. Kim, W. Zhang, and T. DebRoy, *Modeling of temperature field and solidified surface profile during gas-metal arc fillet welding*, Journal of Applied Physics **94** (2003), no. 4, 2667–2679.
- [48] W.-H. Kim and S.-J. Na, *Heat and fluid flow in pulsed current gta weld pool*, International Journal of Heat and Mass Transfer **41** (1998), 3213–3227.
- [49] S.H. Ko, D.F. Farson, S.K. Choi, and C.D. Yoo, *Mathematical modeling of the dynamic behavior of gas tungsten arc weld pools*, Metallurgical and Materials Transactions B **31B** (2000), 1465–1473.
- [50] S. Kou, *Welding metallurgy, second edition*, Wiley-Interscience, 2003.
- [51] S. Kou and D.K. Sun, *Fluid flow and weld penetration in stationary arc welds*, Metallurgical Transactions **16A** (1985), no. 2, 203–213.

- [52] S. Kou and Y.H. Wang, *Computer simulation of convection in moving arc weld pools*, Metallurgical Transactions **17A** (1986), 2271–2277.
- [53] A. Kumar and T. DebRoy, *Calculation of three-dimensional electromagnetic force field during arc welding*, Journal of Applied Physics **94** (2003), no. 2.
- [54] ———, *Guaranteed fillet weld geometry from heat transfer model and multivariable optimization*, International Journal of Heat and Mass Transfer **47** (2004), 5793–5806.
- [55] A. Kumar and T. DebRoy, *Heat transfer and fluid flow during gas-metal-arc fillet welding for various joint configurations and welding positions*, Metallurgical and Materials Transactions **38A** (2007), no. 3, 506–519.
- [56] A. Kumar, W. Zhang, and T. DebRoy, *Improving reliability of modelling heat and fluid flow in complex gas metal arc fillet welds - part i: an engineering physics model*, Journal of Physics D: Applied Physics **38** (2005), 119–126.
- [57] A. Kumar, W. Zhang, C.H Kim, and T. DebRoy, *A smart bi-directional model of heat transfer and free surface flow in gas metal arc fillet welding for practicing engineers*, Mathematical Modelling of Weld Phenomena 7 (H. Cerjak, H.K.D.H. Bhadeshia, and E. Kozeschnik, eds.), Verlag der Technischen Universität Graz, 2005, pp. 3–37.
- [58] S. Kumar and S.C. Bhaduri, *Three-dimensional finite element modeling of gas metal-arc welding*, Metallurgical and Materials Transactions (1994), 435–441.
- [59] Y.P. Lei, Y.W. Shi, H. Murakawa, and Y. Ueda, *Numerical analysis on the effect of sulphur content on weld pool geometry and free surface phenomena for type 304 stainless steel*, Mathematical Modelling of Weld Phenomena 4, IOM Communications Ltd, 1998, pp. 104–122.
- [60] R.W. Jr. Messler, *Principles of welding; processes, physics, chemistry and metallurgy*, Wiley-Interscience, 1999.
- [61] K.C. Mills, *Recommended values of thermophysical properties for selected commercial alloys*, Woodhead Publishing Limited, 2002.
- [62] S. Mishra, S. Chakraborty, and T. DebRoy, *Probing liquation cracking and solidification through modeling of momentum, heat, and solute transport during welding of aluminum alloys*, Journal of Applied Physics **97** (2005).
- [63] S. Mishra and T. DebRoy, *A heat-transfer and fluid-flow-based model to obtain a specific weld geometry using various combinations of welding variables*, Journal of Applied Physics (2005).
- [64] E. Olsson and G. Kreiss, *A conservative level set method for two phase flow*, Journal of Computational Physics **210** (2005), 225–246.

- [65] W. Pitscheneder, R. Ebner, T. Hong, T. Debroy, K. Mundra, and R. Benes, *Experimental and numerical investigation of transport phenomena in conduction mode weld pools*, Mathematical Modelling of Weld Phenomena 4, IOM Communications Ltd, 1998, pp. 3–25.
- [66] I.K. Pokhodnya, O.M. Portnov, and V.I. Shvachko, *Computer modelling of gas partition between the weld metal and its plasma environment*, Mathematical Modelling of Weld Phenomena 5, IOM Communications Ltd, 2001, pp. 55–65.
- [67] R. Rai, S.M Kelly, R.P. Martukanitz, and T. Debroy, *A convective heat-transfer model for partial and full penetration keyhole mode laser welding of a structural steel*, Metallurgical and Materials Transactions **39A** (2008), 98–112.
- [68] P. Sahoo, T. Debroy, and M.J. McNallan, *Surface tension of binary metal - surface active solute systems under conditions relevant to welding metallurgy*, Metallurgical Transactions **19B** (1988), 483–491.
- [69] F. Sikström, A.-K. Christiansson, and B. Lennartson, *Simulation for design of automated welding*, Proceedings of the International Conference on Computer as a tool, Warsaw, Poland, September 2007.
- [70] R. Sizaire, *Numerical study of free surface newtonian and viscoelastic flows*, Ph.D. thesis, Université catholique de Louvain, 1998.
- [71] A. Smolianski, *Numerical modeling of two-fluid interfacial flows*, Ph.D. thesis, University of Jyväskylä, 2001.
- [72] V. Sudnik, *Modelling of the mag process for pre-welding planning*, Mathematical Modelling of Weld Phenomena 3, The Institute of Materials, 1997, pp. 791–816.
- [73] G.A. Taylor, M. Hughes, and K. Pericleous, *The application of three dimensional finite volume methods to the modelling of welding phenomena*, Modeling of Casting, Welding and Advanced Solidification Processes IX (P.R. Sahn, P.N. Hansen, and J.G. Conley, eds.).
- [74] G.A. Taylor, M. Hughes, N. Strusevich, and K. Pericleous, *Second international conference on cfd in the minerals and process industries, csiro, melbourne, australia*, December 1999.
- [75] M.E. Thompson and J. Szekely, *The transient behavior of weldpools with a deformed free surface*, International Journal of Heat and Mass Transfer **32** (1989), no. 6, 1007–1019.
- [76] K.C. Tsao and C.S. Wu, *Fluid flow and heat transfer in gma weld pools*, Welding Journal **67** (1988), no. 3, 70–75.

- [77] W. Villanueva, *Diffuse-interface simulations of capillary phenomena*, Ph.D. thesis, Royal Institute of Technology, Department of Mechanics, 2007.
- [78] M.A. Walkley, P.H. Gaskell, P.K. Jimack, M.A. Kelmanson, and J.L. Summers, *Finite element simulation of three-dimensional free-surface flow problems*, February 2004.
- [79] Y. Wang and H.L. Tsai, *Impingement of filler droplets and weld pool dynamics during gas metal arc welding process*, International Journal of Heat and Mass Transfer **44** (2001).
- [80] D. Weiss, J. Schmidt, and U. Franz, *A model of temperature distribution and weld pool deformation during arc welding*, Mathematical Modelling of Weld Phenomena 2 (H. Cerjak, ed.), The Institute of Materials, 1995, pp. 22–39.
- [81] J. Wendelstorf, I. Decker, H. Wohlfahrt, and G. Simon, *Tig and plasma arc modelling; a survey*, Mathematical Modelling of Weld Phenomena 3, The Institute of Materials, 1997, pp. 848–897.
- [82] C. Winkler, G. Amberg, H. Inoue, and T. Koseki, *A numerical and experimental investigation of qualitatively different weld pool shapes*, Mathematical Modelling of Weld Phenomena 4, IOM Communications Ltd, 1998, pp. 37–69.
- [83] C.S. Wu and L. Dorn, *Computer simulation of fluid dynamics and heat transfer in full-penetrated tig weld pools with surface depression*, Computational Materials Science **2** (1994), 341–349.
- [84] ———, *Numerical simulation of three-dimensional heat and momentum transfer in gma welding*, Mathematical Modelling of Weld Phenomena 3, The Institute of Materials, 1997, pp. 898–916.
- [85] Z. Yang and T. DebRoy, *Modeling macro-and microstructures of gas-metal-arc welded hsla-100 steel*, Metallurgical and Materials Transactions **30B** (1999), 483–493.
- [86] T. Zacharia and S.A. David, *Heat and fluid flow in welding*, Mathematical Modelling of Weld Phenomena (H. Cerjak and K.E. Easterling, eds.), The Institute of Materials, 1993, pp. 3–23.
- [87] T. Zacharia, S.A. David, J.M. Vitek, and T. DebRoy, *Weld pool development during gta and laser-beam welding of type 304 stainless steel, part 1 - theoretical analysis*, Welding Journal **68** (1989), no. 12, 499–519.
- [88] T. Zacharia, A.H. Eraslan, and D.K. Aidun, *Modeling of non-autogenous welding*, Welding Journal **67** (1988), no. 1, 18–27.
- [89] T. Zacharia, J.M. Vitek, J.A. Goldak, T.A. DebRoy, M. Rappaz, and H.K.D.H. Bhadeshia, *Modeling of fundamental phenomena in welds*, Modelling Simul. Mater. Sci. Eng. (1995), no. 3, 265–288.

- [90] W. Zhang, C.-H. Kim, and T. DebRoy, *Heat and fluid flow in complex joints during gas metal arc welding - part i: Numerical model of fillet welding*, Journal of Applied Physics **95** (2004), no. 9, 5210–5219.
- [91] ———, *Heat and fluid flow in complex joints during gas metal arc welding - part ii: Application to fillet welding of mild steel*, Journal of Applied Physics **95** (2004), no. 9, 5220–5229.
- [92] Y. Zhao, H. Zhou, and Y. Shi, *The study of surface active element on weld pool development in a-tig welding*, Modelling Simul. Mater. Sci. Eng. (2006).
- [93] W. Zheng, *Numerical simulation for transient behaviour of fluid flow and heat transfer in stationary pulsed current tig weld pool*, Mathematical Modelling of Weld Phenomena 3, The Institute of Materials, 1997, pp. 817–834.